Robust Displacement Estimation for Ultrasound Elastography and Thermal Imaging

by

Ioana N. Fleming

A dissertation submitted to The Johns Hopkins University in conformity with the requirements for the degree of Doctor of Philosophy.

Baltimore, Maryland

July, 2014

Abstract

Ultrasound imaging is becoming the modality of choice for many diagnostic and surgical procedures. Besides being inexpensive and safe, ultrasonography is emerging as a quantitative tool able to image tissue properties. In this dissertation we focus on elastography and thermal imaging, which both rely on the measurement of real or apparent motion in ultrasound image sequences.

In ultrasound elastography, signal decorrelation is widely viewed as the major limiting factor for adoption of into clinical practice. In this dissertation we focus on improving the robustness of a displacement estimation method based on dynamic programming, addressing multiple weak points. We propose a set of tools which can improve its ability to overcome displacement discontinuities and regions of poorly correlated RF data. The method is further extended to three dimensional data. Phantom, animal and human studies are presented for experimental validation. The addition of robust tools results in an improved ability to achieve repeatable, artifact-

free strain maps, without compromising computational speed.

In thermal imaging, we focus on the estimation of real and apparent motion while the tissue temperature is increased in an ablation procedure. Estimating heat-induced echo shifts is a very difficult problem because of their very small amplitude, on the order of tens of microns. They can easily be masked by other sources of deformation/movement from the environment such as patient motion or hand tremor. In this dissertation, we build upon the robust displacement estimation method for elastography, with the additional deployment of an iterative motion compensation algorithm. The validation experiments are performed on laboratory induced ablation lesions, where the ultrasound probe is either held by the operator's hand or supported by a robotic arm. We demonstrate the ability to detect and remove non-heat induced tissue motion at every step of the ablation procedure. Our results exceed the state of the art in both the accuracy of temperature estimation as well as the length of time over which temperature estimation can be performed. Previous research in the area of motion compensation resulted in good results for experiments lasting less than 10 seconds. Our experiments lasted close to 20 minutes.

Primary Advisor: Dr. Gregory Hager (Johns Hopkins University)

Co-advisor: Dr. Emad Boctor (Johns Hopkins Medical Institutions)

Reader: Dr. Russ Taylor (Johns Hopkins University)

ABSTRACT

Acknowledgments

There are many people without whom this thesis would not have come to be. Most importantly, I cannot thank enough my husband, Brian, with whom I share this accomplishment. He has supported me in ways that I cannot even number. He gave me the confidence to venture on the paths of my dreams, and then he opened new ones for me to explore. His love, patience, and encouragement have carried me throughout the last 12 years, and I am the luckiest person in the world to have had him alongside me for this journey. Brian, you and the kids continue to give me the inspiration which uplifts and helps carry me through each new endeavor I undertake, whether it is teaching, research or a new piece of woodwork.

To my son Martin, to my daughter Penelope and to soon-to-come in this world little one. I am proud to tell the world that you are my three other PhD contributions. Although it has not been easy to continually shift focus in the last 5 years between you and my work, it was thinking of you that made me continue to push forward

every day until this dissertation was finally complete.

To my mom and dad, the first engineers and researchers in my life. Desi m-ati indreptat spre medicina, undeva la un moment dat, materialul genetic si-a spus cuvantul si am ajuns pe calea care eu cred mi se potriveste cel mai bine. Nu pot exprima in cuvinte cat de mult ii datoram, si eu si Brian, mamei mele Ilinca, care nu numai ca a crezut in noi si ne-a incurajat neconditionat pe tot parcursul doctoratului, dar in plus s-a sacrificat de nenumarate ori venind in ajutorul nostru cu cresterea copiilor, pentru ca eu si Brian sa putem continue cercetarea. Fara mama, cu siguranta as fi fost nevoita sa intrerup sau sa renunt la doctorat.

To my in-laws, John and Nancy, whose love and support have surrounded me from the first time I set foot in their home. A special mention to the motorhome which saw the first draft of my dissertation. Thank you very much for everything.

To my colleague and friend Hassan Rivaz, who instigated my first interest in elastography, who mentored me when I was just beginning and with whom I also had the pleasure to co-develop and teach my first class. Thank you for your friendship and your continued support.

I have been fortunate to be surrounded by amazing friends, colleagues, staff and faculty from CIRL, MUSIIC, LCSR, ERC. Thank you all for fun lunches and coffee breaks, for brainstorming research ideas in the lab or at retreats and simply

for providing such a great environment for growing as a researcher and as a person throughout my time at Johns Hopkins.

To Dr. Russ Taylor, with whom I took my first steps into research during the early days of the Eye Project. During those brainstorming sessions, as my first research mentor, you gave me the confidence to step into research and express my ideas. I am very thankful for your continued support, for many insightful discussions, and for your fish stories.

To my co-advisor Dr. Emad Boctor, to whom I owe almost everything I know about ultrasound. From the first day I expressed interest in ultrasound research, you encouraged me, supported me and have been a great motivator for my research. You believed in me and pushed me in new directions while allowing me to come up with my own ideas and solutions. I have been fortunate to have you as a friend who listens not just to my rants about research but also about kids.

Finally, to my advisor, Dr Greg Hager, who taught me when I needed to be taught and let me go when I needed to figure it out on my own. You taught me how to look at the big picture, how to ask the right questions and how to doubt my own results. You believed in me and kept supporting me as I tried to be both a mom and a researcher and I cannot thank you enough for this. I must have tested your patience many times but I hope I came thorough in the end.

ACKNOWLEDGMENTS

Dedication

Pentru mama si tata, pe urmele carora am pornit in inginerie si cercetare.

To Brian and my three other PhD contributions: thank you for your unconditional love and support.

Contents

List of Tables

List of Figures

Chapter 1

Introduction

1.1 Motivation

The field of medical imaging is advancing at a rapid pace. Medical imaging modalities like x-ray radiography, computed tomography (CT), nuclear imaging and magnetic resonance imaging (MRI), are being used in laboratories and hospitals today not only to visualize anatomical structures, but also to detect diseases and plan surgical interventions. Ultrasound imaging stands out as the cheapest and safest imaging modality. It does not require special imaging rooms or expensive additional hardware which has made ultrasound available all over the world.

Fueled by other technological advances and also by growing computational power, basic ultrasound research has experienced a renaissance in the past decade, leading to several innovations in flow mapping [31], measurement of optical properties [67], beamforming [116, 68] and image enhancement [109, 73, 87]. Research developments have also transformed ultrasonography from a qualitative tool for imaging soft tissue into a quantitative tool for measuring tissue properties. In particular, two cases have seen increased interest in recent years: 1) measurement of tissue stiffness (known as strain imaging or elasticity imaging), and 2) measurement of change in tissue temperature (known as thermal imaging). Both elastography and thermal imaging rely fundamentally on the measurement of real or apparent motion in ultrasound image sequences.

In quasi-static elastography, ultrasound images are compared pre- and post-compression to estimate a motion/displacement map. The strain map is generated by differentiating the displacement in the axial direction. When the ultrasound probe is held by a human operator, the elastography is often referred to as "freehand elastography". The basis of elastography have been established by Ophir in 1991 [83] and many possible clinical applications have since emerged. Elastography has been assessed as a tool for detection of tumors, most notably in breast ([40, 45, 49]) and prostate cancer ([21, 114, 98]). Other potential clinical areas include monitoring tumor ablation ([91, 126, 94]) and assessing the extent of plaque in deep vein thrombosis

([26, 29]).

Despite many advances, ultrasound elastography is still not routinely used in clinical practice. The main limitations of current strain imaging systems are:

1. The inability to achieve repeatable, user independent strain images,
2. The need for elastograms with higher strain signal-to-noise-ratio (SNR),
3. The inability to compute strain images/volumes fast enough to be displayed in real-time.

The displacement/motion estimation step is arguably the most important part in overcoming elastography's challenges. In order to achieve repeatable results, the algorithm has to deal with varying degrees of compression from different operators. In addition, the operator needs to apply careful, optimal compression in order to minimize the potential for global and local decorrelation between pre- and post-compression ultrasound signals which usually affects the signal-to-noise-ratio (SNR). In *in vivo* data, other sources of decorrelation could also affect the computation of strain images, such as incoherent fluid (blood) motion, out-of-plane motion of structures within one image due to transducer or respiratory motion, and sub-sample speckle motion. There are several techniques to recover the displacement between pre- and post- compression ultrasound data, including normalized cross-correlation [83],

phase zero estimation [86], and dynamic programming [93, 92]. Decorrelation affects negatively correlation-based methods which use window/block matching, as it introduces significant noise into the displacement map. Large tissue deformations which would be desirable for high SNR [91,123,43] are also not well tolerated by correlation-based methods. Using small segments/blocks for signal matching can lead to errors in finding the right time shift between pre- and post-compression signals, while the use of larger blocks would introduce noise and lower the SNR.

In this thesis we focus on improving on the robustness and accuracy of a displacement estimation method based on dynamic programming [92]. We propose a set of tools which can improve its ability to overcome displacement discontinuities and regions of poorly correlated RF data. We then extend the method to three dimensional data. In order to minimize decorrelation, we first employ the method of Foroughi et al for frame selection [37], followed by the robust displacement estimation on each frame pair. Combining the strengths of both techniques allows for fast displacement estimation. We limit the use of the dynamic programming to one RF line pair per frame, while all the other steps of the algorithm are highly parallelizable, thus greatly decreasing the computational time.

For thermal imaging, monitoring the ablation of tumors in hepatocellular carcinoma has been one of the recent areas of research. The challenge in thermal imaging is estimating the real and apparent tissue motion between two ultrasound data frames

acquired during the ablation procedure. The shifts in the RF echo signals are caused primarily by variations in the speed of sound in tissue with temperature. A secondary cause for changes in the echo signals is the thermal expansion of tissue with heating [65]. The motion produced by the changes in the speed of sound is apparent or virtual, while thermal expansion of the tissue introduces an actual physical shift in the scatterer positions.

As thermal imaging attempts to estimate very small tissue motion (on the order of tens of microns), it can be negatively influenced by signal decorrelation. Patient's breathing and cardiac cycle generate shifts in the RF signal patterns. Other sources of movement could be found outside the patients body, like transducer slippage or small vibrations due to environment factors like electronic noise. Researchers observed that these signal shifts can easily mask the very small temperature-induced tissue displacement. Solutions have been proposed for detecting and compensating for this non-heat induced tissue motion, with most approaches involving the use of signal filtering or smoothing [106, 7, 28].

In this thesis we develop a robust method for heat-induced strain mapping. Initial displacement is estimated using the dynamic programming method [93, 92] with the additional tools developed for ultrasound elastography. The method is then enhanced through an iterative motion compensation algorithm which can detect and remove non-heat induced tissue motion at every step of the ablation procedure.

1.2 Thesis Statement

Robust methods for motion estimation in ultrasound images help overcome displacement discontinuities and regions of poorly correlated RF data. This results in an improved ability to achieve repeatable, artifact-free strain maps, without compromising computational speed. In thermal imaging, estimation of heat-induced echo strain can be further improved by detecting and removing unwanted motion from the environment which would otherwise mask the very small heat-induced tissue displacements.

1.3 Contributions

This thesis addresses limitations of current displacement estimation techniques in ultrasound imaging. We briefly summarize the major contributions of this dissertation as follows:

1. We present a robust algorithm which improves on the dynamic programming displacement estimation method [92], in its ability to overcome displacement discontinuities and poorly correlated regions. Signal decorrelation is widely viewed as the major limiting factor for adoption of ultrasound elastography

into clinical practice. Our contribution is important as it improves the ability to obtain real-time, repeatable, user independent elastograms. The robust implementation addresses multiple weak points in the Rivaz method [92]:

- By addressing the selection of the seed RF line, our method insures a robust, stable starting point for the algorithm.
- By controlling the displacement propagation step, we provide true displacement in regions which would otherwise be negatively affected by decorrelation artifacts.

We evaluate the method on tissue mimicking phantoms and we explore applications to detection of cancerous nodules in the prostate gland during radical prostatectomy.

2. We extend the robust displacement estimation method to three dimensions by pairing it with the frame selection algorithm of Foroughi et al [37]. Combining the strengths of both techniques minimizes the effects of signal decorrelation. We validated the 3D method on human *in vivo* data from hepatocellular carcinoma ablation.

3. We develop additional tools for heat-induced echo strain estimation in thermal imaging. After the initial robust displacement estimation, an iterative motion compensation algorithm is deployed which can detect and filter displacement of tissue due to other sources of deformation/movement. Estimating heat-induced

Table 1.1: Thesis chapters and the corresponding thesis contributions.

Chapter number	Title	Contributions
2	Background and Significance	-
3	Ultrasound Elastography as an Imaging Tool During Prostatectomy: Initial Experience	-
4	Robust Displacement Estimation for Ultrasound Elastography	1,2
5	Ultrasound Elastography Mosaicking	4
6	Thermal imaging	3
7	Conclusions and Future Work	-

echo shifts is a very difficult problem because of their very small amplitude, on the order of tens of microns. We show that removing extraneous motion helps unmask the effects of heating. The method is evaluated on ablated lesions in *ex vivo* tissue.

4. We develop an algorithm for generating reliable multi-image ultrasound elastography mosaics, robust to poorly correlated regions. For proof-of-concept, the method is evaluated in a controlled laboratory setup on 2D and 3D data from tissue-mimicking phantoms.

The correspondence between the thesis contributions and each chapter is presented in Table 4.1.

1.4 Outline

We begin **Chapter 2** by first providing the reader with the necessary background concepts in ultrasound imaging and elastography. We explore various methods for motion estimation which are used in elastography, but also for thermal imaging. The medical impact is underlined by presenting two potentially clinically significant applications: prostate cancer and hepatocellular carcinoma.

In **Chapter 3** we introduce to the reader the regularized dynamic programming displacement estimation technique by Rivaz [92], followed by results of a study evaluating the efficacy of ultrasound elastography as a tumor detection tool in prostate cancer.

Chapter 4 focuses on the robust displacement estimation method for ultrasound elastography. We first analyze the drawbacks of the Rivaz technique with respect to the *in vivo* prostate investigation from Chapter 3. Tools are then introduced for robust seed RF line selection and for correlation-guided displacement propagation. The effects of signal decorrelation are then presented in a tissue mimicking phantom data set. A 3D extension of the robust method is introduced, followed by experimental results from 2D phantoms, 2D *ex vivo* prostate data, 3D phantoms and 3D *in vivo* porcine hepatic tissue following thermal ablation.

In **Chapter 5** we propose an algorithm for ultrasound elastography mosaicking. Methods and experimental results are presented for 2D pair-wise, 2D multi-image and 3D multi-volume mosaicking. Tissue mimicking phantoms are used in an experimental evaluation, under a controlled laboratory setup.

Displacement estimation methods for thermal imaging are presented in **Chapter 6**. Using an iterative motion compensation approach, we attempt to detect and remove extraneous, non heat-induced tissue motion. The efficacy of the method is evaluated on ablated lesions using *ex vivo* chicken breast tissue.

Chapter 7 summarizes the conclusions of our research work and future directions.

Chapter 2

Background and Significance

2.1 Ultrasound Imaging

Sound waves are the organized vibrations of atoms or molecules in a medium. Ultrasound represents sound waves generally above 20 kHz, with medical ultrasound usually in the 1 to 10 MHz range. The basic principle of ultrasound imaging can be described as follows [20]:

An ultrasound pulse is transmitted into tissue where it encounters interfaces and scatters that produce echoes (reflections) as the pulse penetrates tissue. The echoes are recorded and their magnitude and timing are used to form an image.

The component that generates the pulses and measures the echoes is a piezoelectric crystal. Piezoelectric crystals, often referred to as transducers, can be used for ultrasound transmission and reception. They are the interface between the electronic circuits of an ultrasound machine and the physical world.

In ultrasound **A-mode** imaging, a transducer with a single piezoelectric element is excited with a voltage spike to transmit a pulse. As the pulse travels into the tissue, it generates echos from the reflections at tissue boundaries. The intensity of the returning echos is converted into voltage signals, which are commonly referred to as the radio-frequency (RF) signal. The voltage signals can be recorded, digitized and processed in order to be displayed on a computer monitor as an image. The total time between the initial pulse and the echo is proportional to the depth of the boundary, while the amplitude of the echo is proportional to the difference in acoustic impedances at the tissue boundaries. These two pieces of information, coupled with a known or approximate value for the speed of sound in the imaged tissue, allow a one-dimensional mapping of the tissue boundaries along the line of propagation of the pulse. The pulse-echo technique of A-mode imaging produces 1D signals (Figure 2.1), where the amplitude of the echoes are displayed to the user as a function of depth.

B-mode imaging is the natural extension of A-mode imaging into 2D. A modern ultrasound hand-held probe contains a line of piezoelectric elements. Instead

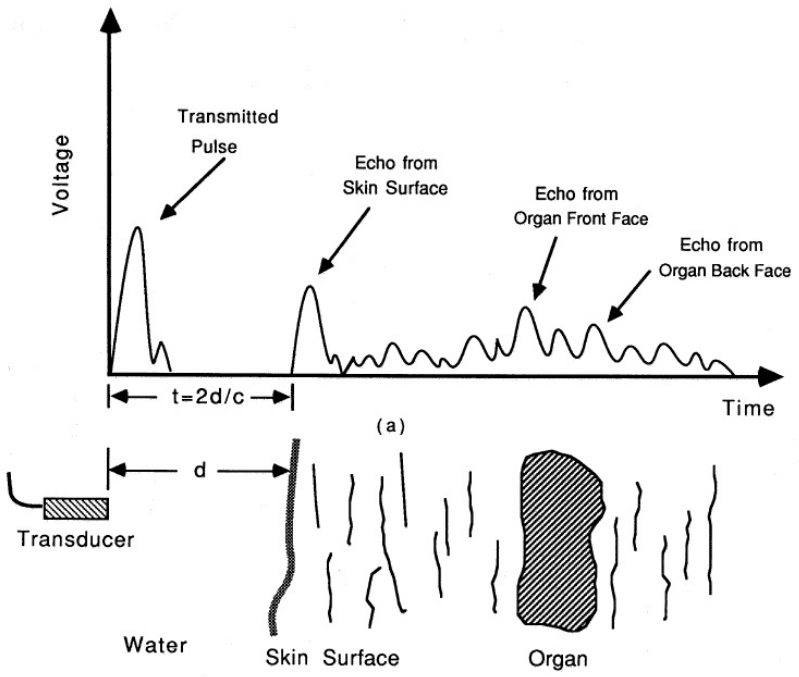

Figure 2.1: Illustration of A-mode ultrasound imaging and the pulse-echo technique (J. L. Prince and J. Links, *Medical Imaging Signals and Systems*. Prentice Hall, 2005)

of displaying the amplitude versus distance, here brightness is used, hence the B in B-mode. The RF signals are combined in columns and the resulting 2D image contains pixels of brightness, calculated as the logarithmically scaled envelope of the RF signal at each depth/location.

2.2 Motion Estimation in Ultrasound Images

In this dissertation, we focus on estimating the motion between two ultrasound images acquired at two different times. We expand below on two ultrasound technologies which could benefit from robust, accurate motion estimation: ultrasound elastography and thermal imaging.

2.2.1 Ultrasound Elastography

Physicians have used palpation for thousands of years and for some diseases it is still the primary diagnostic tool. Examples include breast self-examination for early detection of breast lumps and digital rectal examination for prostate cancer nodules. Palpation is so effective as a medical tool because many diseases cause changes in the mechanical properties of tissues. Various inflammatory and neoplastic processes result in an increase in stiffness or elastic modulus of the tissue. It is also worth noting that surgeons routinely use manual palpation intra-operatively in open procedures, to asses the degree of stiffness in tissues undetected pre-operatively by CT, MRI, or conventional B-mode ultrasound.

Several years ago, Ophir et al [83] introduced a new method termed *elastography* for direct ultrasound imaging of the stiffness of tissues. Emulating manual palpation, the tissue was compressed and apparent motion of regions of the image were compared. From this information, measurements related to tissue stiffness were computed.

The main components of elasticity imaging are:

1. Data capturing during externally or internally applied tissue motion or deformation,
2. Evaluation of tissue response, and,
3. Reconstruction of the elastic modulus or other physical properties based on the theory of elasticity, which usually results in a map/image of the tissue.

Static elasticity methods involve applying compression directly to the tissue [83,80,81], while dynamic ones induce motion by applying a low-frequency vibration to the tissue [55,58,57,129,1]. Many literature reviews describe various dynamic and static elasticity imaging techniques [39, 82, 43, 44, 84]. In Acoustic Radiation Force Impulse (ARFI) Imaging the excitation is applied internally. In addition to the conventional ultrasound beams for imaging (called tracking beams), ARFI uses the ultrasound beams to to also push the target tissue (called pushing beams) [78].

In all three methods, RF signals are acquired before and after tissue excitation and are then used to estimate tissue motion. Vibro-elastography is an extension of static elastography where the tissue is externally vibrated over a range of frequencies simultaneously and the resulting displacement is recorded at multiple locations and time instants with a sequence of ultrasound images [118]. For some elasticity methods the final resulting image maps physical parameters, like Young's modulus and Poissons ratio, while others provide a more qualitative image of stiffness distribution in tissue. Vibro-elastography methods have been used to estimate visco-elastic properties of tissue like viscosity and density [118, 30]. The literature refers to measurements acquired under static and dynamic excitation collectively as *elasticity imaging*.

Among the techniques used for tissue displacement estimation in quasi-static elastography, two have been studied in depth: correlation based approaches and phase-based methods. The method as first proposed by Ophir et al [83] used correlation maximization between windows/segments of RF signal from the pre and post-deformation A-line pairs. It still remains the most widely used method today. The reference window is translated in small overlapping steps along the RF line and a time shift $t_{1..n}$ is estimated for each n segment pairs. Time shifts are indicative of tissue response, where stiffer tissues move less under compression, while soft tissues would exhibit a larger motion. The strain image is produced by displaying a unified map of spatial derivatives from the estimated motion field on each A-line [83]:

$$s_i = \frac{t_{i+1} - t_i}{2 * dz/c}; i = 1..n \tag{2.1}$$

where s_i represents the strain estimate for segment pair i, dz is the amount of applied compression in the axial direction and c is the speed of sound through the respective tissue.

The second dominant approach for tissue displacement estimation was pioneered by ODonnell et. al. [80, 81], who showed that there is a direct relationship between the relative displacement between two windows and the phase of the complex correlation between baseband signal windows. At time t, the baseband representation of two signals $x_1(t)$ and $x_2(t)$ are [80, 81]:

$$\tilde{x}_1(t) = A(t - \tau_1)e^{-i\omega_0\tau_1}, \tag{2.2}$$

$$\tilde{x}_2(t) = A(t - \tau_2)e^{-i\omega_0\tau_2}, \tag{2.3}$$

where A is the real envelope of the transceived pulse, ω_0 is the angular frequency of the ultrasound carrier, and τ is the round-trip propagation time from the transducer to the point scatterer. The complex correlation function between the two signals can be evaluated as:

$$\tilde{C}(t) = \frac{1}{T}\int_0^T \tilde{x}_1\tilde{x}_2^*(t+\tau)d\tau = A(t-\tau_1)A(t-\tau_2)e^{-i\omega_0(\tau_2-\tau_1)}, \tag{2.4}$$

The time delay between $x_1(t)$ and $x_2(t)$ can be estimated from the zero phase of $\tilde{C}$, while a non-zero phase can be used to estimate the location of the peak without further search [81]:

$$\Delta\phi(0) = tan^{-1}\left[\frac{Im(\tilde{x}(0))}{Re(\tilde{x}(0))}\right] \tag{2.5}$$

$$\Delta x = \frac{c * \Delta\phi}{2\omega_0}, \tag{2.6}$$

where c is the speed of sound.

Despite ongoing progress, ultrasound elastography needs to overcome some challenges before a successful adoption into clinical use. The displacement estimation step plays a very important role as it has arguably the biggest impact on the speed and accuracy of elasticity algorithms. Every method of displacement estimation can be negatively impacted however, by signal decorrelation. Many enhancements to the displacement estimation step have been proposed to reduce signal decorrelation effects, most notably signal companding (compression and expanding) [15, 123, 18]. Axial stretching can only compensate for decorrelation due to scatterer motion in the axial direction; decorrelation due to lateral and elevational motion or other sources do not benefit from these methods. In addition, there has been active research in improving the quality of strain estimation. Tracking approaches have focused on

the way the displacement map is accumulated. Assuming displacement continuity, Pesavento et al.[86] and Zhu et al. [131] were the first to propose elastography algorithms where each point's displacement is initialized to the previously calculated displacement value of it's neighbor. Other row-to-row tracking algorithms have been proposed [63] and similar techniques have been developed for column [50, 51], diagonal [130] or other [63, 117] directions of propagation. Chen et al. [19] rejected the displacement continuity assumption and implemented an algorithm governed by the presence of high-quality data areas, where displacement is propagated around these regions first and poorly correlated data segments are estimated last (or not at all), in order to limit their overall influence.

In general, these post-processing steps improve signal quality, but they also introduce significant computation demands, making it challenging to display elastograms in real-time. The ability to display the strain map in real-time to the user is very valuable in the medical community, where such capability greatly increases the potential elastography might become the tool of choice for image guided surgical interventions. The speed of the displacement estimation becomes even more important in three-dimensional elasticity imaging, where the volume of the data increases computational demands. Jiang el al [51] and Rivaz et al. [93] were the first to frame the displacement estimation as an optimization problem solved by dynamic programming. Rivaz et al [92] greatly improved the speed of the displacement estimation

without sacrificing accuracy. The 2D Analytic Minimization (AM) method uses dynamic programming to estimate 2D sub-pixel displacement values on one seed axial RF line, which are later propagated line-by-line throughout the entire image.

2.2.1.1 Three Dimensional Ultrasound Elastography

The first 3D ultrasound imaging systems used conventional arrays which were mechanically translated in the elevational direction [32]. Similarly, 3D strain imaging was first attempted by comparing pairs of images acquired at each position in the elevational direction. Keeping the applied compression between adjacent frame pairs constant or within very little variation becomes very important [100, 62]. A second technique for 3D strain imaging is to acquire the pre- and post-compression volumes sequentially. A small pressure is applied to the tissue between volume acquisitions using a mechanical or simulated fixture [56,64,4,27,34,35], or by freehand compression [117]. Both methods are slow and cumbersome in the data acquisition phase, requiring great care to avoid signal decorrelation between the pre- and post-compression frames.

Two hybrid approaches in 3D elastography stand out recently. Houdsen et al. [46] applied freehand compression at each step of the sweep and selected several frames, before the stepper motor was advanced to the next location in the elevational direction. This method has ease of acquisition as it bypasses the practical difficulty

of performing careful and optimal compression between pre- and post-compression frames. It still suffers however from the point of view of data acquisition, which can be quite slow for large volumes. Tracking the 2D wobbler transducer using a position sensor allows Foroughi et al. to select aligned pairs of RF frames with minimal out-of-plane motion, ensuring high quality strain [38, 37]. The acquisition is fast as RF data is continuously collected while the operator performs freehand compression and relies on the tracking algorithm to select suitable pairs. The downside of the method is that it requires additional tracking hardware.

2.2.2 Thermal Imaging

Thermal ablation therapies, using energy sources like RF, laser, microwave, or focused ultrasound, aim to destroy malignant tumors without damaging the surrounding tissue. But despite promising results, current systems remain highly dependent on operator skill, and there is little control of the size and shape of the ablated area. Monitoring the spatial distribution of heating is necessary to control the degree of tissue damage produced. Conventional B-mode ultrasound has been used historically for guiding the ablative tools. But the ablation lesion and surrounding tissue have similar back-scatter characteristics, making conventional B-mode ultrasound images alone unable to clearly distinguish the boundaries between the two areas. Many have

observed an increased echogenicity at the site of the ablation and shadowing below the thermal lesion (cavitation effects) [125, 74]. These effects are easily observed late in the ablation process, once the ablated area has reached a larger size, on the order of centimeters. It is still difficult to accurately ascertain the size and position of the thermal lesion on B-mode images alone and, furthermore, it is nearly impossible to delineate the treated tissue margins.

Although conventional B-mode ultrasound does not provide a clear delineation of the ablated region, algorithms have been proposed which use the raw RF signals and are very similar to strain estimation. Several techniques for heat-induced echo strain are based on estimating the echo shifts using speckle tracking [65, 66, 104, 106, 115], and differentiating the time-shift estimates along the axial direction to obtain a temperature map. Temperature estimates are obtained using a cross-correlation algorithm applied to raw ultrasound RF data acquired at discrete intervals during heating [125]. Measurements have been validated experimentally in tissue and tissue-mimicking samples [74, 85, 110, 2].

Just as motion tracking in strain estimation methods can be affected by signal decorrelation, thermal ablation procedures can be plagued by non-heat induced motion as well. Solutions for the compensation of cyclic respiratory and cardiac motion in ultrasound thermal strain images have been attempted recently by several groups [106, 7, 28]. It is worth noting that these efforts only monitored the effects of

motion compensation on heat-induced echo strain imaging for a very brief period of time, at most 4-5 seconds [7].

2.2.3 Ultrasound Elastography Mosaicking

Compared to other imaging modalities like CT and MR, ultrasound suffers from a limited field of view (FOV). Monitoring a structure can be particularly challenging when it is too large to be visualized in a single image or 3D sweep. Size and distance measurements are unreliable in large organs. With the ability to obtain a 3D ultrasound volume, the next evolutionary step in 3D ultrasound is to create an extended field of view by stitching several volumes together. Ultrasound mosaics (also referred to as stitching or panorama) are emerging as a prevalent technique in clinical practice with a high clinical value. They aim to achieve several advantages which come along with extended FOV: 1) improving the understanding of spatial relationships among structures when the size of a single image/volume is not large enough to cover the entire region of interest, 2) visualizing structures that are too large for a single volume and 3) allowing for measurements of size and distance in large organs and lesions, and 4) compounded volumes of higher quality will offer the ability to visualize the anatomical structures from a variety of angles.

In the literature of ultrasound mosaicking, registering the underlying displace-

ment field for elastography has not yet been addressed. The clinical advantages of ultrasound mosaics can be improved with the additional corresponding strain information. In particular, strain information can help in multi-modal registration and fusion with pre-operative data for guidance in minimally-invasive interventions.

2.3 Clinical Significance

In this thesis we consider two clinical applications : prostate and hepatic cancer. In the remainder of the chapter we will briefly explain (for each application) the diseases/conditions involved, treatment options and the imaging techniques currently used for monitoring and intervention, as well as how a more robust and accurate strain algorithm can aid and improve these clinical applications.

2.3.1 Prostate Cancer and Laparoscopic Prostatectomy

Prostate cancer develops in the prostate, a gland in the male reproductive system. It is the second leading cause of cancer death and the most common cancer detected in men in the United States. An estimated 238,590 new cases of prostate

cancer were diagnosed in the United States, and approximately 29,720 men died of prostate cancer during 2013 [105]. The severity of the disease dictates the management strategy. Treatment of aggressive centralized prostate cancer may involve Radical Prostatectomy (RP) which aims for complete cancer resection and has been shown to improve cancer survival [9]. The surgical procedure was historically an open intervention but more recently laparoscopic alternatives have emerged. Robotic-assisted laparoscopic prostatectomy (RALP) relies on the daVinci Surgical System (Intuitive Surgical, Sunnyvale, CA) which provides 3-D visualization, higher magnification, hand tremor elimination and refined dexterity by incorporating wristed instrumentation. Since the year 2000, when the Food and Drug Administration (FDA) approved the daVinci robotic surgical system for conducting abdominal and pelvic surgeries, its use has skyrocketed. The daVinci Surgical System is now used to perform as many as 4 out of 5 radical prostatectomies in the United States [76]. From 250 robotic cases in the beginning (2001), the number has reached 73,000 by 2009, as 86 % of the 85,000 American men who had prostate cancer surgery opted for the robotic approach) [13, 89] .

Initial experiences with the daVinci Surgical System have been positive: short learning curve, limited blood loss, less post-operative pain, fewer perioperative complications, and short hospital stay [13, 89, 77, 3, 24, 5, 33, 8]. But what concerns the doctors and patients more is whether the robotic approach reduces the chances for

cancer recurrence and improves the quality-of-life after the procedure. In the hands of a trained surgeon, does the robot offer better chances for complete cancer excision and sparing of the fragile cavernous nerves (Figure 2.2 [14])? One recent study found patients were three times more likely to require salvage therapy [48], while another study focused on Medicare-age patients concluded that for this age group the risks of problems with continence and sexual function are equally high after both open and robotic procedures [6].

One theoretical disadvantage with regards to robotic surgery is the lack of tactile feedback. In open RPs, the surgeon uses his or her fingers to feel the periphery of the prostate gland [128]. Without tactile feedback, a robotic surgeon is unable to appreciate differences in tissue texture or firmness and therefore may not be able to tailor precisely the extent of tissue excision around the prostate gland in efforts to eradicate all cancerous tissue. Inadvertently leaving residual cancer cells behind, called a positive surgical margin (PSM), is highly associated with cancer recurrence. PSM rates were initially higher in RALP than in the open procedure, but they have been shown to decrease with surgeon's experience and improved technique [33, 48].

As manual palpation helps guide the surgeon in the open procedure, an equivalent real-time guiding tool is needed for laparoscopic prostatectomy. Imaging modalities like MRI or CT are not feasible intra-operatively, nor do they possess the sensitivity or specificity for accurate detection and localization of prostate cancer. Transrectal

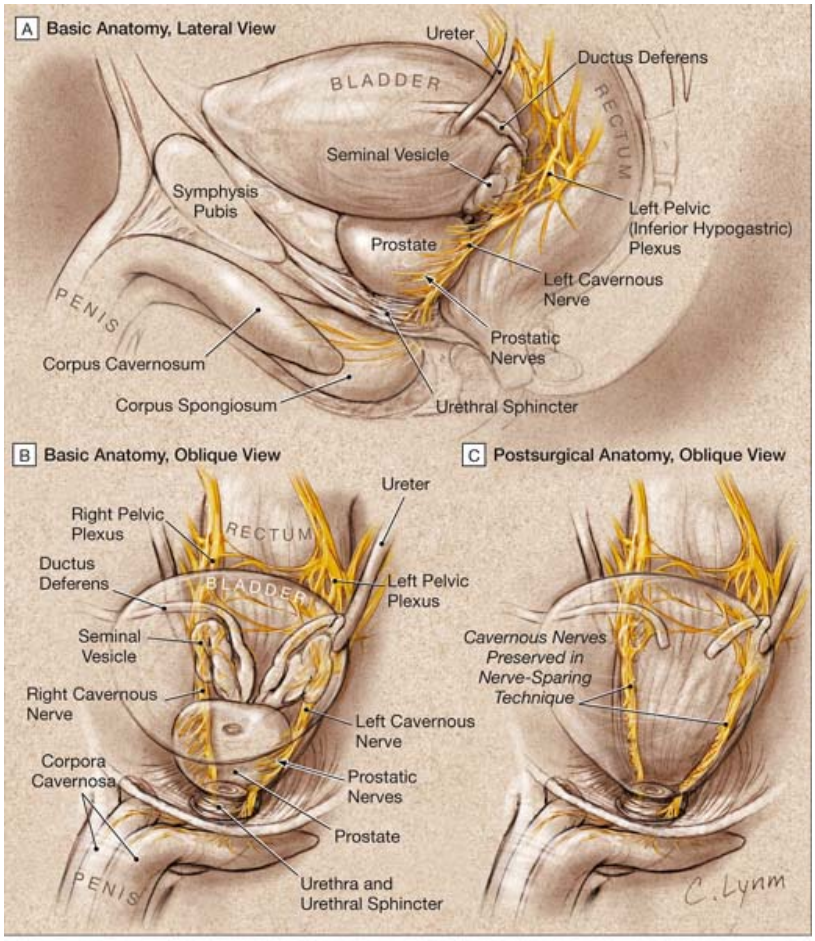

Figure 2.2: Anatomical illustration of the nerve-sparing prostatectomy technique. Courtesy of Dr. Arthur L. Burnett

ultrasound (TRUS) is routinely used in diagnosis, in conjunction with digital rectal examination (DRE) and biopsies [98]. One center used TRUS for real-time monitoring and guidance during Laparoscopic RP and reported technical feasibility and enhanced precision by decreased PSM rates [120, 121]. TRUS was capable of imaging a substantial percent of non-palpable prostate cancers. The authors recognized however, the limitations of TRUS guidance; it requires considerable prior expertise and tends to identify primarily hypoechoic lesions, which were just 47% of the cancer nodules studied [121]. Today's prostate cancer patients are more likely to present with echogenic or isoechoic lesions because aggressive screening techniques lead to a shift toward smaller, early-stage cancers [23,25] ; classic B-mode gray-scale ultrasound alone cannot identify these lesions.

Ultrasound (US) Elastography (USE) is emerging as a valuable tool in the field of imaging. Cancers tend to present as hard lesions due to increased cellularity, which makes them suitable for elastography where harder, stiffer tissue will have smaller strain than softer, more compliant tissue [82]. Echogenicity and stiffness of tissue are generally uncorrelated; USE can identify hypoechoic lesions, but also echogenic or isoechoic cancers that classic gray-scale ultrasonography cannot. Elastography through the transrectal approach has already been been used successfully in guiding biopsies of the prostate [21,54,114,59]. Integrating USE technology with a laparoscopic ultrasound probe will give robotic and laparoscopic surgeons an important

intra-operative image-guidance tool, which until this point does not exist [102,101,10].

Ultrasound raw data used in the elastography algorithms suffers however from all of the challenges described in section 2.2. Improving on the robustness and accuracy of the displacement estimation step can impact the use of elastography as an interventional tool. A laparoscopic ultrasound probe with integrated elastography algorithm and strain visualization could help the surgeon at the crucial time of prostate excision. For radical prostatectomy, this could mean lower PSM rates, reduces chances of recurrence and maybe an improved sparing of the fragile cavernous nerves. The probe could also be used to investigate the adjacent seminal vesicles and the pelvic lymph nodes to asses the spread of cancer in more advanced patients.

2.3.2 Hepatocellular Carcinoma and Tumor Ablation

Hepatic cancers are malignant tumors that grow on the surface or inside the liver. Liver cancer is the fifth most frequently diagnosed cancer globally and the second leading cause of cancer death. In 2013 in the United States, hepatic cancer saw 30,640 new cases and was responsible for 21,670 deaths [105]. 75% of liver cancer is formed by liver cells (hepatocytes) which become malignant and it is known as

Hepatocellular Carcinoma. Surgical resection is often the treatment of choice but less than half the patients are eligible for removal and transplant as the cancer is usually detected in late stages. Percutaneous ablation offers an alternative cure for this group. Radio frequency ablation (RFA), microwave ablation, laser ablation, and high-intensity focused ultrasound (HIFU) employ heat to destroy the cancerous cells.

In RFA, an electrode is placed inside the tumor under ultrasound guidance (Figure 2.3). High frequency alternating current in the range of $350 - 500$ kHz flows from the probe into the tissue leading to thermal coagulation. At temperatures above 45° C the cell proteins denature and the cell membrane begins to lose its integrity which eventually leads to irreversible necrosis [71]. The goal of the ablation is to destroy all the malignant cells, plus an additional 0.5 to 1.0 cm tumor-free margin to reduce the chances for cancer recurrence [97]. The size of the ablated region has been shown to depend on the electrode gage, the temperature of the probe and the duration of the treatment [71, 96]. But local hepatic factors can also influence the size of the necrosis. Nearby blood vessels can act as a heat sink, where a strong local blood flow has been reported to be a predictor of small size in the necrotic lesion [71].

Real time monitoring of the expansion of the ablated region, its shape, size and location would insure the success of the procedure and lower the risk for cancer recurrence. Currently, imaging assessments are done post-operatively and without much success, which represents the biggest drawback to RFA therapy. CT and MRI

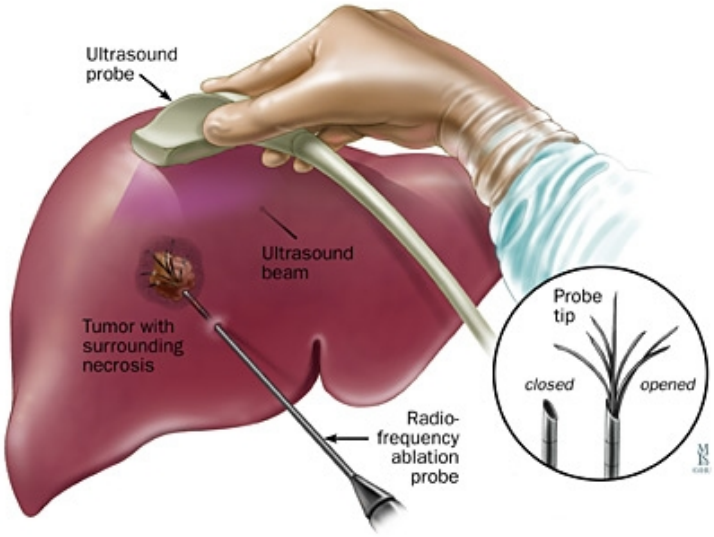

Figure 2.3: Radiofrequency ablation (RFA) in liver cancer (hepatocellular carcinoma)

have been shown to be able to predict the necrotic area to within 2-3 mm but these imaging modalities are rarely available intra-operatively for real time monitoring and are usually performed within 1 week following the RF ablation session, when results are compared with baseline examinations to differentiate between ablated regions and residual tumor requiring additional therapy [42]. Conventional B-mode ultrasound recognizes the ablated area where the acoustical properties of tissue have changed, but cannot clearly distinguish the necrosis zone [16, 61]. Gas bubbles formed in the ablated region during RFA treatment define a hyper-echoic region on conventional ultrasonography [42, 109]. Gas bubbles may however occlude the visualization of the RFA probe and of the ablated region but they resolve within 1 hour after treatment [124]. Contrast enhanced ultrasound (CEUS) looks at microbubble contrast agents through the liver and aims to assess the degree of vascularity in the ablated

region. A promising technique, CEUS is ideally performed 5-10 minutes after each ablation, while the patient is still under general anesthesia. When used for monitoring purposes, treatment is continued until complete avascularity is demonstrated with CEUS, making it practically unfeasible during a busy multi-site ablation intervention [109].

As the temperature of tissue increases cell proteins start degrading and losing water, which corresponds with an increase in tissue stiffness [53]. This makes ultrasound elastography an ideal imaging modality for monitoring the RFA procedure both intra-operatively and at later follow-ups. Elastography has recently been investigated for this purpose in ex-vivo tissue [126, 12, 11, 122]. A robust 3-D elastogram would improve the accuracy of monitoring the ablative lesion.

Cellular protein denaturation starts at 45° C and the rate of necrosis increases exponentially with the rise in temperature. At 45° C, necrosis occurs within 20 to 30 minutes, at 50 to 55° C, necrosis occurs within 5 minutes, and at temperatures between 60 to 100° C, necrosis occurs immediately [71, 47, 108, 79]. If heat-induced motion can be correctly estimated, temperature imaging methods can prove very valuable in addition to elastography. Monitoring the temperature around the RFA probe and the spatial distribution of heating would insure control over the degree of tissue necrosis produced and could prevent unnecessary damage to healthy tissue.

Chapter 3

Ultrasound Elastography as an Imaging Tool During Prostatectomy: Initial Experience

3.1 Introduction

Prostate cancer is the most diagnosed form of cancer in men in the United States [105]. For patients with a localized form of the disease, complete removal of the prostate gland is often recommended. Open radical prostatectomy was developed

in the 1940s and then refined in the 1980s by Dr. Patrick Walsh (Johns Hopkins Urological Institute, Baltimore, MD) who pursued an anatomical approach, aiming for complete cancer removal. The nerve-sparing approach is one of several technical advances pioneered by Dr. Walsh [128], where efforts are made to preserve the fragile cavernous nerves which are responsible for sexual function and urine continence. Alternatives to open surgery have recently emerged. In laparoscopic radical prostatectomy, the surgeon operates through several small abdominal incisions with the help of small, stick-like instruments. The DaVinci Surgical System (Intuitive Surgical, Sunnyvale, CA) refined the laparoscopic technique: the laparoscopic tools have small, precise, wristed instruments which are maneuvered by a surgeon, but operated in cooperation with a robot. Other improvements include 3-D visualization, FOV magnification and hand tremor elimination. The new robot-assisted laparoscopic radical prostatectomy has gained a lot of support in the last decade, with an estimated 80% of procedures today being robot-assisted [76].

Several studies have investigated the success of the robotic-assisted procedure versus the traditional open approach. Initial experiences showed many positives: short learning curve, limited blood loss, less post-operative pain, fewer peri-operative complications, and short hospital stay [13,89,77,3,24,5,33,8]. What concerns surgeons is the lack of tactile feedback. Unlike the open prostatectomy surgeon, the robot-assisted surgeon cannot palpate the prostate gland, running the risk of leaving behind

cancerous tissue. Laparoscopic and robot-assisted prostatectomies can benefit from an intra-operative imaging tool which can give them the feedback equivalent to manual palpation. Ultrasound elastography (USE) appears to be the natural candidate and the technology can be incorporated in a laparoscopic tool. The remainder of this chapter continues as follows. Section 2 summarizes an elastography algorithm based on the dynamic programming (DP) technique for tissue displacement estimation [93]. We then present the methodology, results and conclusion of a pilot study where human *ex vivo* prostatectomy specimens where used to assess the accuracy of USE in the identification and characterization of hard cancerous nodules. We compared the elastogram results with histopathology maps (the gold standard) and also to pre- and post-operative MR scans of the prostate gland in order to assess and co-localize anatomically USE with the reference histopathology and MR scans.

3.2 Ultrasound Elastography: Prior Work

3.2.1 2D Dynamic Programming Displacement Estimation

Quasistatic elasticity imaging usually involves two steps: 1) the pre- and post-compression ultrasound raw RF data is compared to estimate a displacement map, and then 2) a strain image is obtained by axial differentiation of the displacement data. Jiang el al [51] and Rivaz et al. [93] were the first to frame the displacement estimation as an optimization problem solved by dynamic programming (DP). Rivaz et al [92] refined the algorithm by improving the speed of the displacement estimation without sacrificing accuracy. The 2D Analytic Minimization (AM) method uses dynamic programming to estimate 2D sub-pixel displacement values on one seed axial RF line, which are later propagated laterally throughout the entire image.

Consider two ultrasound RF frames I_1 and I_2 acquired before and after tissue compression. Let n be the number of RF lines, with each signal sampled at $i = 1,\ 2 \cdots m$. Rivaz estimates the integer axial a_i and lateral l_i displacements of each RF line pair using DP [93]. The cost function is generated by combining the prior of displacement continuity (smoothness term) and an amplitude similarity term. The

smoothness term takes into account displacement continuity in both axial and lateral direction:

$$R_j(a_i, l_i, a_{i-1}, l_{i-1}) = \alpha_a(a_i - a_{i-1})^2 + \alpha_l(l_i - l_{i-1})^2 \tag{3.1}$$

where α_a and α_l are axial and lateral regularization weights respectively.

The distance between pre- and post-compression signals for line pair j can be written as:

$$\Delta(i, j, a_i, l_i) = [I_1(i, j) - I_2(i + a_i, j + l_i)]^2 \tag{3.2}$$

The cost function at the ith sample of the jth A-line becomes:

$$C_j(a_i, l_i, i) = \min_{d_a, d_l} \left\{ \frac{C_j(d_a, d_l, i-1) + C_{j-1}(d_a, d_l, i)}{2} + w\Delta(i, j, a_i, l_i) \right\} \tag{3.3}$$

where w is a regularization weight for smoothness; d_a and d_l are temporary axial and lateral displacements which are varied in order to minimize eqn.(3.3). The integer displacement estimates are then refined to subpixel displacement estimation, by comparing the original pre-compression signal I_1 (not downsampled) with the post-compression signal I_2 upsampled by a factor of γ using parabolic interpolation [93]. Repeating the refinement procedure n times results in a refinement factor of $(\frac{1}{\gamma})^n$ [93]. The process is repeated for all n RF line pairs, which makes the entire displacement estimation algorithm very computationally expensive.

3.2.2 2D Analytic Minimization Displacement Estimation

Axial a_i and lateral l_i integer displacements are obtained here using DP on only one RF line pair, called the seed line. The subsample displacement estimation algorithm continues as follows:

1. a_i and l_i are first subsampled using linear interpolation. Then they become initial guesses for the 2D subsample displacement estimate for the seed line [92]. Let s be the seed RF line. The aim is to calculate Δa_i and Δl_i such that the pair $(a_i + \Delta a_i, l_i + \Delta l_i)$ gives the axial and lateral displacements at the sample i. The regularized cost function becomes [92]:

$$\begin{aligned} &C_s(\Delta a_1, ..., \Delta a_m, \Delta l_1, ..., \Delta l_m) = \\ &= \textstyle\sum_m^{i=1}\{[I_1(i,s) - I_2(i + a_i + \Delta a_i, s + l_i + \Delta l_i)]^2 + \\ &+\alpha\left(a_i + \Delta a_i - a_{i-1} - \Delta a_{i-1}\right)^2 + \beta_a\left(l_i + \Delta l_i - l_{i-1} - \Delta l_{i-1}\right)^2\} \end{aligned} \tag{3.4}$$

   where α and β_a are regularization terms which ensure continuity in displacements with respect to the top: α for axial and β_a for lateral.

2. Propagate the solution of the seed RF line from column to column to the left and right of the frame, using the displacement of the previous RF line as an initial estimate. The regularized cost function for the j^{th} RF line becomes [92]:

$$
\begin{aligned}
&C_j(\Delta a_1, ..., \Delta a_m, \Delta l_1, ..., \Delta l_m) = \\
&= \textstyle\sum_m^{i=1}\{[I_1(i,j) - I_2(i + a_i + \Delta a_i, j + l_i + \Delta l_i)]^2 + \\
&+\alpha\left(a_i + \Delta a_i - a_{i-1} - \Delta a_{i-1}\right)^2 + \beta_a\left(l_i + \Delta l_i - l_{i-1} - \Delta l_{i-1}\right)^2 + \\
&+\beta_l'\left(l_i + \Delta l_i - l_{i,j-1}\right)^2\}
\end{aligned}
\tag{3.5}
$$

where $l_{i,j-1}$ is the lateral displacement of the previous RF line. α, β_a and β_l' are regularization terms which ensure continuity in displacements with respect to the top (axial α), and the top and left/right (lateral β_a and β_l').

3.3 Materials and Methods

Prostate cancer patients, candidates for prostatectomy, were prospectively enrolled in our study, following an informed consent approved by the Institutional Review Board. The objective of the study was to evaluate the DP elastography method by Rivaz et al ([93]). We studied the efficacy of using DP elastography to identify and precisely localize hard nodules such as seen with prostate cancer just beneath the surface of the prostate gland in the peripheral zone. In this area, cancerous lesions are at most risk of invasion beyond the confines of the prostate gland and also more likely to be cut across by a well meaning surgeon. We recruited patients who underwent both open and assisted prostatectomies given that the process of removing the gland was not a focus of our study. Patients underwent multiple radiological procedures:

1. Pre-operative 3 Tesla MRI of the pelvis was performed right before the surgery procedure.

2. Post-operative ultra high-resolution MRI at 9.4 Tesla was performed on the excised prostate specimen to correlate the results to *in vivo* pre-operative imaging.

3. Ultrasound elastography was then performed on the prostate specimen by an experienced radiologist blinded to the surgeon's findings and to the pre-operative pathology report. The collected RF data was used offline to recreate classic B-mode grey-scale images, and also to compute elastograms showing the stiffness of the tissue scanned, using the Rivaz approach from section 3.2.2 [93, 92].

Pre-operative and post-operative MR scans were used for anatomical correlation with the computed elastograms. For ultrasound elastography, the prostate specimens were placed in prone position on a surgical table. USE scans were performed in a systematic sextant approach, similar to that used for image guided biopsies. RF data was acquired in axial planes (from gland's base, through mid gland, to apex), on the left and right side of the gland (Figure 3.1). The sextant approach was necessary to ensure that the scans were in the same plane with the histopathology diagrams (axial) which constituted the gold standard for comparison. USE coronal scans from the left to the right of the gland were also performed; these scans were in alignment with the MR coronal scans.

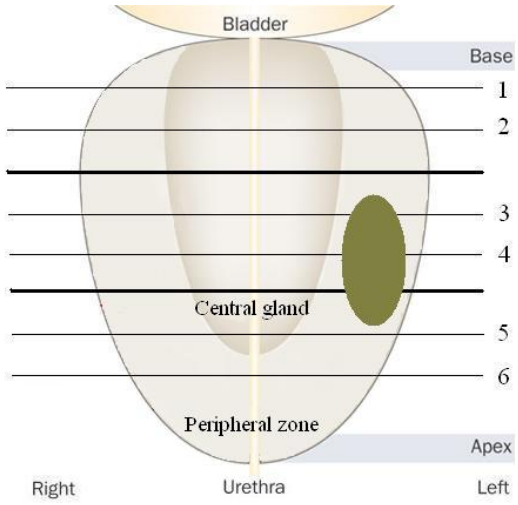

Figure 3.1: Ultrasound elastography data collection process using the sextant approach; RF data was acquired in axial planes (1 - 6) from the gland's base towards the apex. For illustration purposes, a lesion is outlined in the left mid section, peripheral zone of the specimen, similar with specimen #3 of our study

Hardware and Software Specification

USE acquisition was conducted using a Siemens Antares US scanner (Siemens Medical Solutions USA, Inc. Ultrasound Division, Issaquah, WA) with an ultrasound research interface to access raw RF data. Data was acquired by manual handling using a Siemens VF 10-5 linear array for prostate specimens. After RF data collection, elastograms were obtained using the DP elastography algorithm of Rivaz [93, 92].

Each prostate specimen underwent routine pathologic processing and analysis. Due to the high volume of prostatectomies performed at our institution, the routine pathological process does not result in a whole mount mapping. Instead, for histopathological evaluation the prostatectomy specimens were initially sliced at every 3-4 mm from apex to base, according to the Stanford protocol. Each slice (6 to

10 master slices) were then incorporated in a paraffin block and sliced at 5 μ meter thickness. The slices were stained with hematoxylin-eosin and were then analyzed under a microscope by a pathologist blinded to the surgeon's findings and also to the elastography results. The localization and size of each tumor focus were documented for all step master slices on axial diagrams, with Gleason score. Large macro photographs were reconstructed in several specimens (Figure 3.3(c)). All data collected were stored in a database.

N = 10 target areas were analyzed from N = 6 patients enrolled into the elastography analysis. Histological findings served as the *gold standard* in determining the presence, location and size of any prostatic nodules, malignant and benign. The objective of our study was then to compare axial elastograms findings with the histological findings recorded by the pathologist (mapping diagrams, measurements and nodule characteristics such as malignant vs. benign). Since histopathology diagrams often specified just the maximum diameter of a lesion, coronal elastograms were used to better establish the location and extent of the identified lesions. MRI images (both axial and coronal planes) were aligned to the elastograms and provided help with their anatomical co-registration using anatomical details such as urethra or boundaries of peripheral zone vs. central gland.

3.4 Results

DP elastography identified N=10 lesions, eight hard nodules in the peripheral zone, one hard and one soft nodule in the central gland (Table 3.1). Pathology reports showed the eight hard lesions in the periphery as malignant and the remaining two from the central gland as benign. Diameter measurements correlation proved difficult because of the inability to perfectly register the three investigative modalities. Size measurements and Gleason score are reported in Table 3.1. USE versus MRI measurements were within on average 2.05 mm vs. 2.25 mm of the diameters measured by pathology (standard deviation of 1.9 mm for USE and 2.9 mm for MRI).

Table 3.1: Prostate specimen data: A total of ten elastography lesions were identified in six human prostate specimens (eight malignant and two benign). PZ = peripheral zone, CG = central gland

#	Location	Gleason Score	Size (cm)		
			Elastography	Pathology	MRI
1.1	PZ base	3+5	1.4 x 0.8	1.3 x 0.8	1.3 x 1.1
1.2	CG base	N/A-Solid	0.7 x 1.1	1.0 x 1.0	1.0 x 1.1
1.3	CG base	N/A-Soft	1.1 x 0.8	1.0 x 1.0	1.0 x 0.9
2.1	PZ base	5+3	3.0 x 1.3	2.4 x 1.0	2.0 x 1.5
3.1	PZ mid	4+5	2.4 x 0.8	1.9 x 1.0	1.5 x 1.2
4.1	PZ mid	3+3	1.0 x 0.5	0.5 x 0.4	0.6 x 0.7
4.2	PZ mid	3+4	1.5 x 0.9	1.1 x 0.5	1.1 x 0.8
5.1	PZ apex	3+3	0.5 x 0.6	0.5 x 0.5	0.6 x 0.6
5.2	PZ apex	4+3	0.6 x 1.0	0.8 x 0.9	0.9 x 0.9
6.1	PZ base	3+3	0.7 x 1.2	0.7 x 1.8	0.7 x 0.7

Concerning the entire lesion area in cm^2, a paired t-test looking at the elastography and MRI estimates versus pathology measurements found very little differences between the groups (Table 3.2. Mean values indicate both elastography and MRI over-

Table 3.2: Lesion size (cm^2) as detected by elastography and MRI vs pathology: t-test results. Mean, standard deviation (StDev) and standard error of mean (SEM) are presented for each group.

Group	Elastography	Pathology		Group	MRI	Pathology
Mean	1.218	1.032		Mean	1.119	1.032
StDev	1.0494	0.6922		StDev	0.8	0.6922
SEM	0.3318	0.2189		SEM	0.253	0.2189
p-value = 0.3273				**p-value = 0.4769**		

estimated the size of the lesions, but the differences are not statistically significant ($p - value = 0.3273$ for elastography vs pathology and $p - value = 0.4769$ for MRI vs pathology)

Specimen #1 presented multiple hard and soft lesions, located in the central gland of the prostate (Figure 3.2). The *ex vivo* T2-weighted coronal image from specimen MRI obtained at 9.4 Tesla (Figure 3.2 (C) - here after counter clock wise rotation for better visualization of the correlation between USE and MRI of the specimen) shows detailed anatomy of the heterogeneous central gland with a solid benign prostatic hypertrophy nodule (BPH) confirmed by pathology. Elastography was able to detect this solid nodule despite the heterogeneity of the prostate (Figure 3.2 (B)) - solid arrow, whereas the lesion was not clearly identified by gray scale ultrasound. *Ex vivo* T2-weighted 9.4 Tesla coronal image from specimen MRI also shows an additional soft cystic BPH nodule (dashed arrow). Urethra is also visible on the elastogram , as well as MRI exam (labeled *urethra*).

Axial scans of the same specimens were compared with histopathology axial

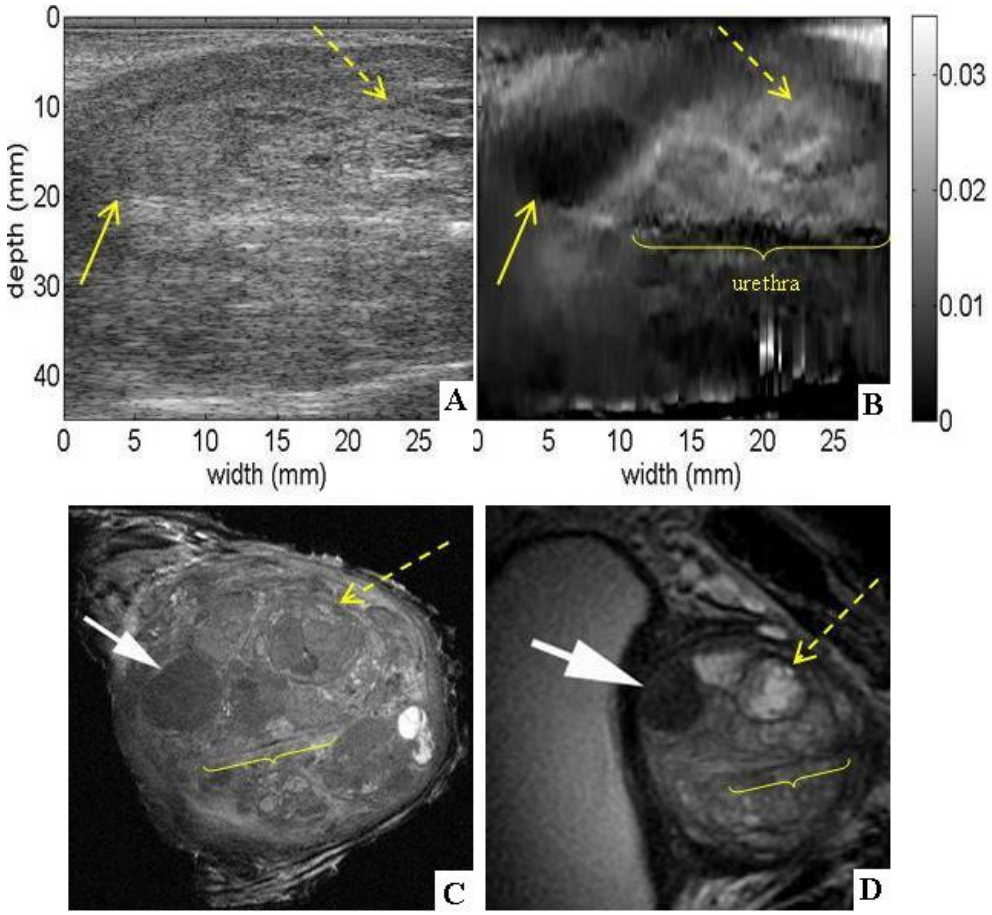

Figure 3.2: Coronal section of prostate specimen #1 at the level of the central gland. Classic ultrasound B-mode (A) and elastogram (B). 9.4 Tesla *ex vivo* (C) and 3 Tesla *in vivo* (D) MRI images are presented in coronal planes, after CCW (counter clock wise) rotation for better visualization of the correlation between USE and MRI of the specimen. Benign solid (arrow) and soft (dashed arrow) nodules and urethra are visible.

cross-sections. The prostate, submitted for histological processing in four quadrant sections per slice, was digitally realigned to reconstruct a full histological cross-section (Figure 3.3(c)). Specimen #1 was found with a tumor with Gleason score of 8 at the prostate base, left side (outlined). Figure 3.3(a) shows an ultrasound B-mode image and an elastogram obtained through an axial plane at the prostate's base on the left side. The same tumor was identified by elastography (Figure 3.3(b) - dashed contour) but is not visible on grey-scale ultrasound. For anatomical correlation, a soft - cystic nodule anterior to cancer can be seen on B-mode image and USE (Figure 3.3(a), 3.3(b) - arrows) and on histopathology (Figure 3.3(c) - arrows).

The remaining five prostate specimens presented with superficial lesions in the peripheral zone of the gland. USE identified multiple hard malignant lesions in various locations, from the base to the apex of the prostate gland. One can notice the clear delimitation of these lesions on USE (Figure 3.4) as well as the close estimations of size versus pathology and MRI.

3.5 Discussion

In surgical procedures where manual palpation would be helpful but not possible to perform, e. g. laparoscopic robotic surgery, USE can offer added value if proven

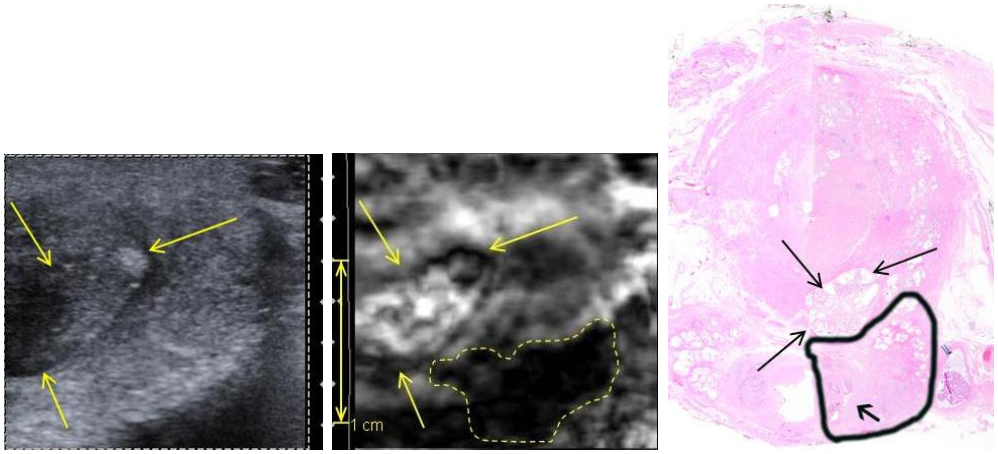

(a) (b) (c)

Figure 3.3: Axial section of prostate specimen #1 peripheral zone. Left lateral section of the prostate's base; classic ultrasound B-mode (a) and elastogram (b). Hard lesion is outlined, arrows point to adjacent nodule. (c) Hematoxylin & eosin stained histological section of prostate base. The tumor (Gleason score 3+5 = 8, outlined in black) extended beyond the prostatic capsule in this section and invaded the left seminal vesicle (arrow).

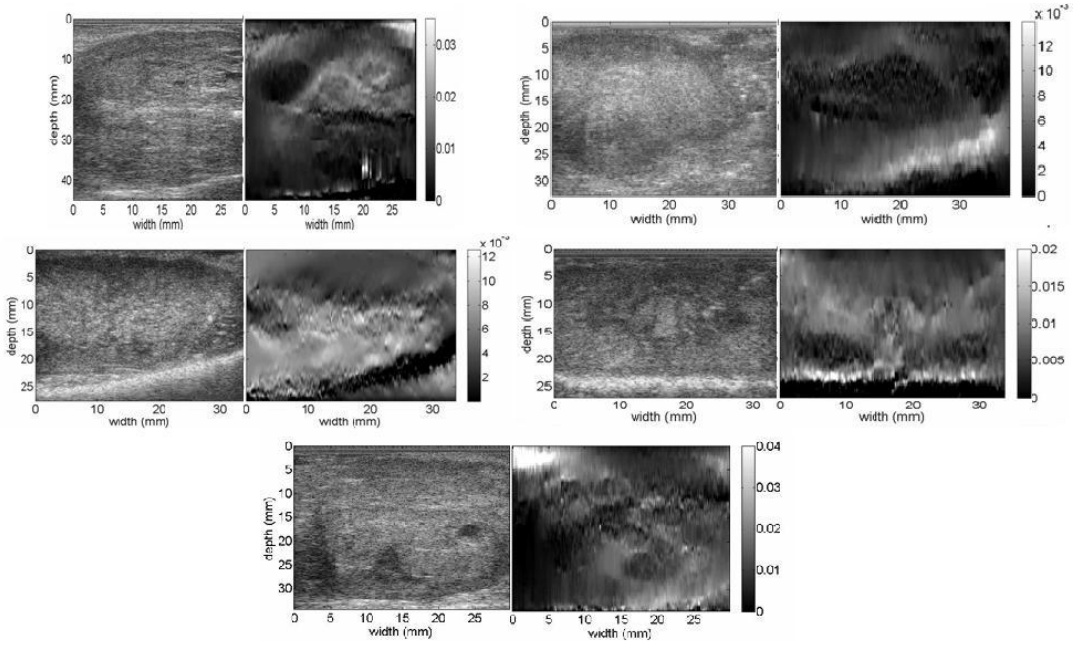

Figure 3.4: B-mode image (left) and elastogram (right) from specimens # 2-6. Dark regions at the very bottom of elastograms represent structures outside the prostate tissue (e.g. operating table). The border of the prostatic tissue can be easily noticed as a highly reflective band at the bottom of B-mode images.

to be accurate in detecting pathologic lesions. Our feasibility study showed that DP elastography with the method pioneered by Rivaz et al ([93]) was able to identify both hard and soft lesions in the *ex vivo* prostate specimens, located in the deep prostatic central gland and in the peripheral zone. Histopathologic findings validated USE, and results compared favorably with the *in vivo* pre-surgical and *ex vivo* post-surgical MRI scans. In the central gland of the prostate, elastography showed excellent detection of hard and soft areas, despite the complexity of this region. Elastography was able to identify both hard and soft BPH nodules and anatomical landmarks like the urethra (note excellent anatomical correlation to MR scan findings). In the peripheral

zone USE identified multiple hard malignant lesions, from the base to the apex of the prostate gland. These preliminary results demonstrate the ability of USE to detect hard nodules in the prostate and are encouraging in the pursuit of this technology as a palpation equivalent imaging tool for prostatectomy.

USE maps tissue elasticity which makes it an ideal imaging modality to serve as a surrogate and possible equivalence to manual palpation in identifying hard cancerous tissue in the prostate gland, especially in the peripheral zone but also in the central gland. Real-time intra-operative imaging guidance is needed for identifying the presence of cancer within the prostate, especially near the capsule where tumor can invade and spread outside of the gland, and also for studying surrounding structures. If diseased hard lymph nodes could be detected, then lymphadenectomy may provide a more accurate cancer staging, help tailor future therapy, and potentially prevent recurrence. A better delineation of the bladder neck and apex during dissection, especially when prostate cancer is located at the apex could perhaps improve patients' outcome. If deemed possible, imaging cavernous nerves (CNs) located along the immediate surface of the prostate gland may lead to their preservation, and thus improved preservation of potency and urinary continence [113]. Further more, the development of the elastography technology as an imaging guiding tool during prostatectomy could potentially be useful in the open procedures as well, where the manual palpation would not be enough to identify deeper lesions. It has been documented in

the literature that prostate carcinoma originates in the central gland and transitional zone in up to 30% of cases [72, 22].

3.6 Conclusions

Our initial experience showed USE was able to reliably identify hard nodules in the peripheral zone of the prostate that were prostate cancers. Additionally, USE showed its ability to define tissue hardness of BPH nodules despite the underlying tissue complexity in the central gland. Our comparative study demonstrated USE can approach the efficacy of manual palpation for superficial lesions and has the potential to surpass it for smaller, deeper lesions. Our initial experience with USE encourages us to pursue further the evaluation of this technique. The results obtained in this study using the DP elastography method by Rivaz et al ([93]) are considered our baseline results. The limitations of this method are discussed in the following chapter, where a more robust elastography method is also presented.

Chapter 4

Robust Displacement Estimation for Ultrasound Elastography

4.1 Introduction

In quasi-static elasticity imaging the tissue is compressed and ultrasound raw data is acquired before and after the deformation. The goal is to compare the two RF frames in order to estimate the displacement between them. Data acquisition however, is problematic and often results in poor elasticity image quality. Repeatable elastograms are often hard to generate as strain images are highly qualitative and

user-dependent. The best results are achieved when the operator compresses and decompresses the tissue uniformly, in the axial direction, and at an optimal speed [45]. Signal decorrelation affects negatively all the methods used today for displacement estimation. It can be a result of probe movement due to slippery or oblique surfaces, but also small lateral or out-of-plane motions [45,82,17]. Even with a skilled operator, other sources of decorrelation can also affect the displacement estimation, such as uncontrolled physiological motion (heartbeat, muscle contractions, respiration and blood flow) and movement of other structures due to breathing [17]. The widespread clinical use of elastography could benefit from the development of elastography algorithms less influenced by factors such as user expertise or signal decorrelation. The goal of achieving reliable, repeatable, user independent elastograms thus depends heavily on solving the decorrelation problem.

In the previous chapter we summarized Rivaz's elastography algorithm [93,92] and presented the results of a study using this algorithm with *ex vivo* prostate data. We encountered several examples of poorly correlated data regions in the prostate data set. In these cases, the resulting strain images can present structures with the wrong relative stiffness to one another (Figure 4.1(a)) or can simply be overwhelmed by artifacts which will obscure the real structures (Figure 4.1(b)).

The presence of decorrelation affects the Rivaz displacement estimation algorithm in two ways.

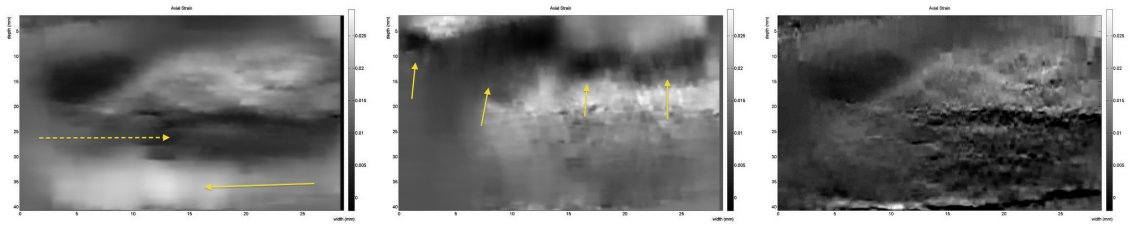

(a) (b) (c)

Figure 4.1: Prostate specimen #1: the final elastogram depends on the selection of the seed RF line. In (a), some structures are wrongly identified as soft (arrow) or hard (dashed arrow). In (b), multiple artifacts (arrows) obscure the real structures. Elastogram (c) agrees with the pathology report.

1. Choosing the seed RF line in a decorrelated region will result in a poor displacement estimate for that line, as well as allow incorrect estimates to propagate laterally throughout the strain map. Figure 4.2 shows an example of the effects of choosing a seed RF line from a poorly correlated data region. The incorrect initial estimate can create a small strain artifact (Figure 4.2 (b)) or it can propagate throughout the majority of the frame (Figure 4.2 (d)).

2. The choice of a robust seed RF line does not guarantee however, proper estimates for the entire frame. If the AM displacement propagation encounters a wide region of poorly correlated RF data, it is unlikely the estimates will maintain correct values as the region is traversed, potentially corrupting even the estimates in the highly correlated region beyond.

Methods are needed both for robust seed line selection and also for correlation-guided displacement propagation. The contribution of this chapter is the development

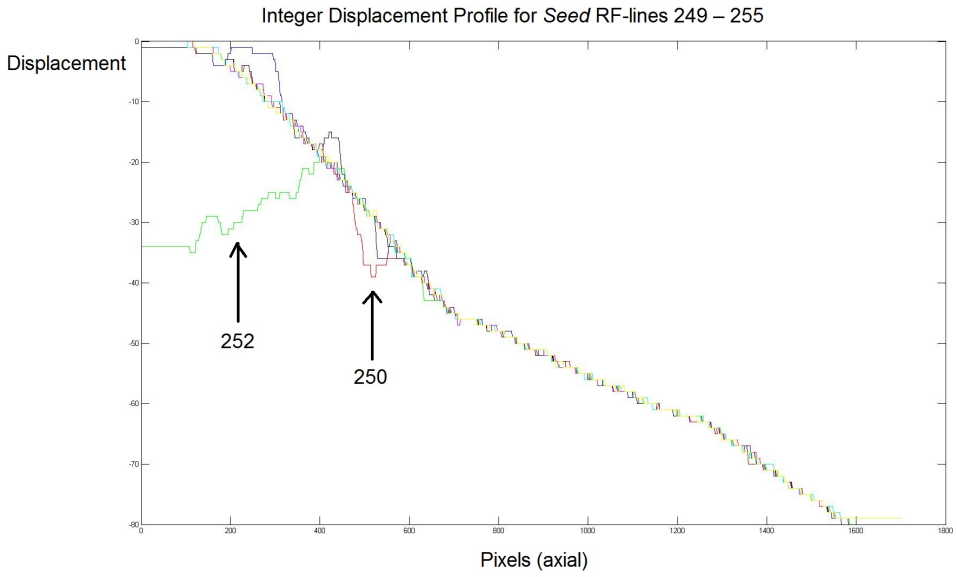

(a)

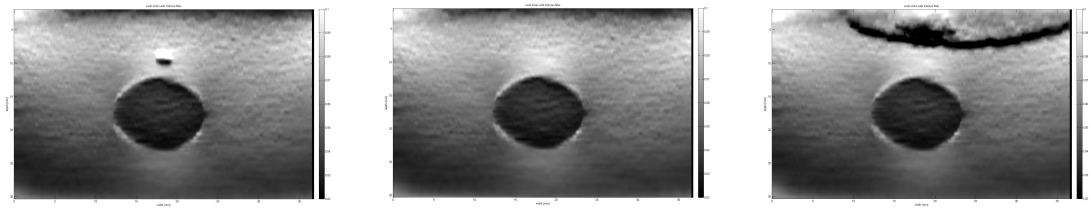

(b) Seed line 250 (c) Seed line 251 (d) Seed line 252

Figure 4.2: Integer DP displacement estimation in tissue-mimicking phantom for seed RF lines 249 - 255 (a). Note the areas (for lines 250 and 252 respectively) which exhibit a visible difference in displacement estimate. Strain images with corresponding artifacts for seed lines 250 (b) and 252 (d), and artifact-free for seed line 251 (c).

of robust methods and quality metrics which improve on the Rivaz technique [93, 92]. The algorithm addresses the choice of one or more robust starting seed RF lines, as well as the propagation of displacement values from column to column. Compared to the original algorithm, the current implementation is more robust to signal decorrelation and it can estimate tissue motion even in poorly correlated regions of the ultrasound images.

In a closely related work, Chen et al. [19] implemented an algorithm governed by the presence of high-quality data areas, where displacement is propagated around these regions first and poorly correlated data zones are estimated last (or not at all) to limit their overall influence. One stated advantage is that no preferential displacement propagation direction is needed. The limitation of their technique is that by rejecting the displacement continuity assumption, some imaged areas are not being displayed to the user, the authors choosing to leave gaps (blank areas) in the elastograms in regions deemed to be low quality. Our work relies on column-to-column displacement propagation but our results show this does not compromise the strain quality. We also address the continuity problem by using data quality metrics which can detect changes in the degree of correlation, allowing for reliable estimation of displacement even in poorly correlated regions.

The remainder of this chapter is summarized as follows. The robust methods for seed RF line selection and for correlation-guided displacement propagation are

discussed in Section 2, followed by a 3D extension of the algorithm in Section 3. Validation experiments using tissue-mimicking phantoms, *ex vivo* human prostate data and *in vivo* porcine liver data are presented in Section 4. Section 5 concludes the chapter and discusses future research directions.

4.2 Methods

We are proposing a set of methods to deal with the presence of signal decorrelation. The first subsection 4.2.1 presents two tools which will restrict the choice of seed line in an area unaffected by decorrelation to insure a robust starting point for the displacement estimation algorithm. The next subsection 4.2.2 introduces quality metrics to be used in displacement propagation, while subsection 4.2.3 makes the case for dividing the image frames into multiple sub-images, each with their own seed line, to allow parallelization and speed up of the overall run time without sacrificing accuracy. The last subsection details a 3D extension of the algorithm.

4.2.1 Seed RF line selection

The following methods address the selection of a robust seed RF line, unaffected by signal decorrelation.

- *Displacement Slope*

  In a continuous piece of tissue, the axial displacement profile resulting from a stress field induced by applied compression has a monotone ramp [69]. In the presence of decorrelation, the DP displacement estimation algorithm can sometimes fail to achieve an optimal solution along the entire axial line. Small segments of the RF data can be falsely aligned and result in displacement estimates which would not reflect the stress field.

  We hypothesized that for small deformations, these locally optimal solutions would correspond to perturbations in the monotone slope of their displacement profile, which in turn would result in artifacts in the final strain image (Fig. 4.2). In Algorithm 1 we compute ϵ_{max} as the number of consecutive data points which exhibit a change in the slope's direction along the axial displacement profile (a_i for $i = 1,\ 2 \cdots m$ are the integer axial displacement estimates after DP). In our phantom study, we found that a value of $\epsilon_{max} \geq 3$ indicates a region of poorly correlated, artifact-inducing data (Section 4.3). Note that the three data points don't need to be consecutive, as long as the ramp stays flat or continues to change direction (Figure 4.3), as computed in lines $7 - 12$ of Algorithm 1.

- *Displacement Stability*

  In the DP algorithm [93], w is a smoothness regularization parameter (eq. 3.3)

Algorithm 1 Calculate ϵ_{max}

```
1: ε ← 0;
2: ε_max ← 0
3: for i = 1 to m do
4:     if (a_i − a_{i−1}) ∗ (a_{i+1} − a_i) < 0 then
5:         ε ← ε + 1
6:         i ← i + 1
7:         while (a_i − a_{i−1}) ∗ (a_{i+1} − a_i) ≥ 0 do
8:             if (a_i − a_{i−1}) ∗ (a_{i+1} − a_i) > 0 then
9:                 ε ← ε + 1
10:            end if
11:            i ← i + 1
12:        end while
13:        if ε > ε_max then
14:            ε_max ← ε
15:        end if
16:        ε ← 0
17:    end if
18: end for
```

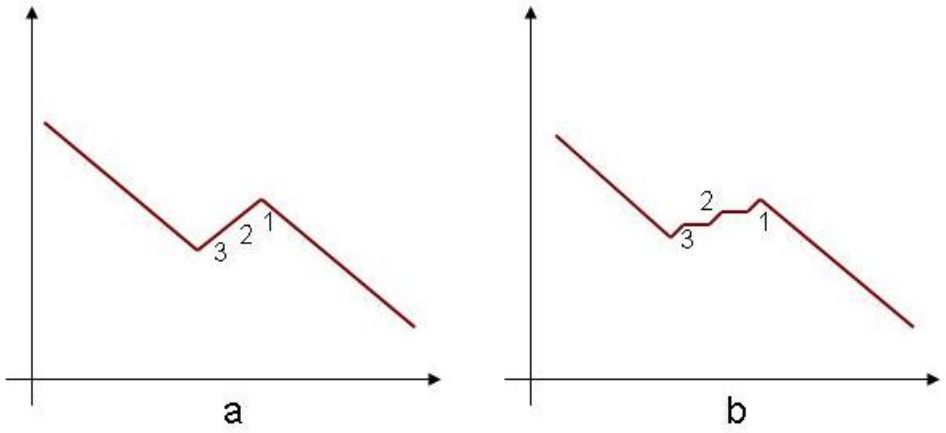

Figure 4.3: *Displacement slope.* The three data points where the change in slope is exhibited could be consecutive (a) or not (b)

meant to prevent regions with high local decorrelation from introducing errors in displacement estimation. If w is chosen too large it can result in an over-smoothing of the solution. We hypothesized highly correlated pairs of RF lines would give consistent displacement estimation results regardless of the chosen value for w (in a suitable range). Regions of poorly correlated RF data would give different displacement estimation results, given different values of w. We thus compute the metric As[1] for *instability* as:

$As =$ the percentage of data points along an RF line, which exhibit a discrepancy in the axial displacement estimate of at least δ units (pixels).

$$As = \Sigma_{i=1}^{m}(a_i^{w_1} - a_i^{w_2} \geq \delta)m \tag{4.1}$$

[1] As was chosen as the letter symbol for *instability* from the periodic table element Astatine. The name "astatine" comes from the Greek word ástatos, meaning "unstable", due to the element's propensity for radioactive decay (all isotopes of the element have been shown to be unstable)

where $a_i^{w_1}$ and $a_i^{w_2}$ are axial displacements estimated using w_1 and w_2 respectively, and m is the length of each RF line signal.

A high value of As suggests a poorly correlated RF signal pair. In our phantom study, we found that a value of $\delta \geq 3$ indicates the presence of region(s) of poorly correlated, artifact-inducing data (Section 4.3).

4.2.2 Robust displacement propagation

Consider two ultrasound RF frames I_1 and I_2 acquired before and after tissue compression. Let n be the number of RF lines, with each signal sampled at $i = 1,\ 2 \cdots m$. At the end of the displacement estimation process on the j^{th} pair of RF lines, $A_i = a_i + \Delta a_i, L_i = l_i + \Delta l_i$ are the axial and lateral displacements at each sample i (eq. 3.5). Using the estimated displacement values, and the raw RF signals pre- and post-compression, we calculate how well the estimates fit the data. A high-quality estimation would exhibit a high degree of correlation between the RF signals. We chose the magnitude of the normalized cross-correlation as an indicator for the degree of matching between the pre- and post-compression data.

For the j^{th} pair of RF lines, we compute:

$$C(I_1(j), I_2(j)) = \left| \frac{\sum_m^{i=1}(I_1(i,j)-\bar{I}_1)(I_2(i+A_i,j+L_i)-\bar{I}_2)}{\sqrt{\sum_m^{i=1}(I_1(i,j)-\bar{I}_1)^2 \sum_m^{i=1}(I_2(i+A_i,j+L_i)-\bar{I}_2)^2}} \right| \tag{4.2}$$

where $\bar{I}_1$ and $\bar{I}_2$ are the means of RF values along the j^{th} line of each frame.

$C(I_1(j), I_2(j))$ is a good indicator of the quality of the DP + AM displacement estimate for line j. As the array of A_is and L_is become the initial guesses for propagating forward to line $(j+1)^{th}$ (eq. 3.5), we can assess if the displacement propagation should continue or not. A poor initial guess would result in a potentially corrupted forward estimate. Even starting with a high-quality estimate could result in a corrupt forward estimate if the adjacent RF line pair $((j+1))$ exhibits a region of poorly correlated data. We can compute the same correlation metric for the RF line pair $(j+1)$ (eq. 4.2), plugging in the estimated displacements for line j:

$$C_{fwd}(I_1(j+1), I_2(j+1)) = \left| \frac{\sum_m^{i=1}(I_1(i,j+1)-\bar{I}_1)(I_2(i+A_i,(j+1)+L_i)-\bar{I}_2)}{\sqrt{\sum_m^{i=1}(I_1(i,j+1)-\bar{I}_1)^2 \sum_m^{i=1}(I_2(i+A_i,(j+1)+L_i)-\bar{I}_2)^2}} \right| \tag{4.3}$$

where A_i and L_i are the displacements for RF line j, and $\bar{I}_1$ and $\bar{I}_2$ are the means of RF values along the $(j+1)^{th}$ line.

As discussed in section 3.1, tracking algorithms which use the quality of data as an indicator of signal decorrelation fail to produce displacement estimates in the presence of high noise [19]. As suggested by [19], a quality metric enforcing continuity of displacement estimates would be desirable, to avoid differentiation across

displacement discontinuities which can generate artifacts. To ensure a continuity of high quality, highly correlated data, we compute the ratio ρ as follows:

$$\rho_{j+1} = \left| \frac{C_{fwd}(I_1(j+1), I_2(j+1)) - C(I_1(j), I_2(j))}{C(I_1(j), I_2(j))} \right| \tag{4.4}$$

4.2.3 Robust 2D elastography method with multiple seed lines

Given two ultrasound RF frames I_1 and I_2 exhibiting areas of poor correlation, we are proposing a displacement estimation method which relies on the selection of a robust starting seed RF line, followed by displacement propagation guided by each adjacent line's underlying degree of similarity.

We consider the question of selecting a **single** starting location, or **multiple** seed lines. As displacement is tracked from column-to-column, the presence of a poorly correlated signal pair would stop the propagation, practically requiring the selection of a new seed RF line, on the other side of the troublesome area. To reduce the time of the displacement estimation over the entire image, one could divide each image into K sub-regions from the start, each requiring a robust seed RF line. The selection of multiple robust seed RF lines presents the advantage of initializing in

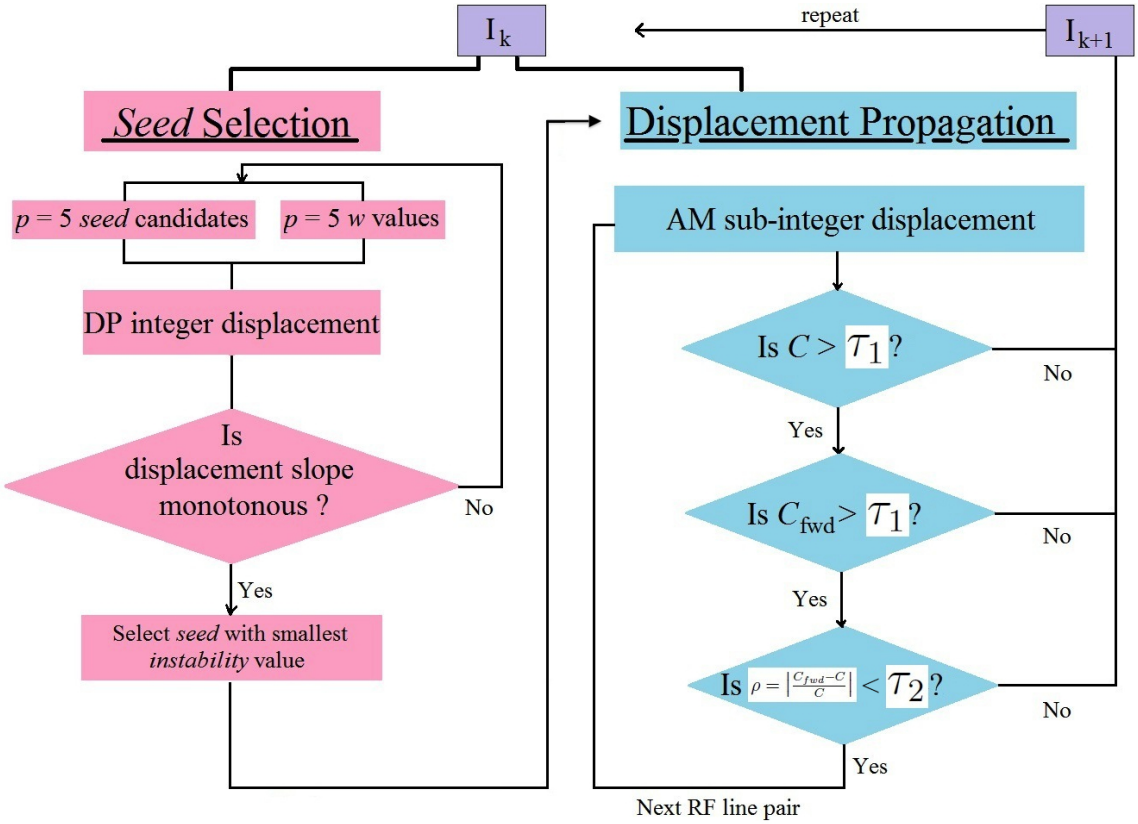

Figure 4.4: Algorithm flowchart. Left side represents the seed selection step, while right side presents the displacement propagation decisions. If the thresholds are not met, propagation stops and the remaining portion of the RF frame will be treated as a new sub-image I_{k+1}, where a new seed RF line will need to be selected.

multiple high correlation regions, increasing the chances for a more robust, artifact-free elastogram.

Let each RF image frame I be divided into K sub-images. Let n_k be the number of RF lines for sub-image I_k $(k = 1..K)$, with each signal sampled at $i = 1,\ 2 \cdots m$. We first select a seed line as follows (Figure 4.4):

1. Select random p potential candidates for the seed RF line pair.

2. Perform integer displacement estimation q times for each pair, using q random w values in a chosen range (Section 3.2.1, Eqn. 3.3).

3. Keep only the pairs for which $\epsilon_{max} \leq 3$ for ALL values of w (Algorithm 1).

4. From the remaining candidates, the pair with the lowest *instability* value As becomes the seed RF line (4.1).

After the selection of a robust seed RF line j, the estimated displacement values are propagated laterally to the adjacent lines until all m_k lines are processed. For each adjacent line pair $j+1$, using as initial displacement estimate the values calculated for pair j, we calculate C, C_{fwd}, and ρ as indicators of data quality (eqs. 4.2, 4.3, 4.4). Two thresholds govern the following set of conditions which will guide the displacement propagation:

1. If the j^{th}'s displacement estimate is a good fit for line pair j, $C > \tau_1$.

2. If the j^{th}'s displacement estimate is a good initial guess for line pair $j+1$, $C_{fwd} > \tau_1$.

3. To ensure a continuity of high quality, highly correlated data, $\rho < \tau_2$.

We study the impact of w on the *instability* value As, as well as the choice of thresholds τ_1 and τ_2 in section 4.3.1. If all the conditions are met, the displacement

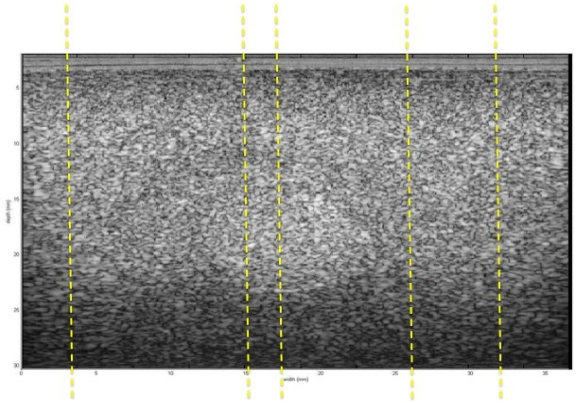

(a)

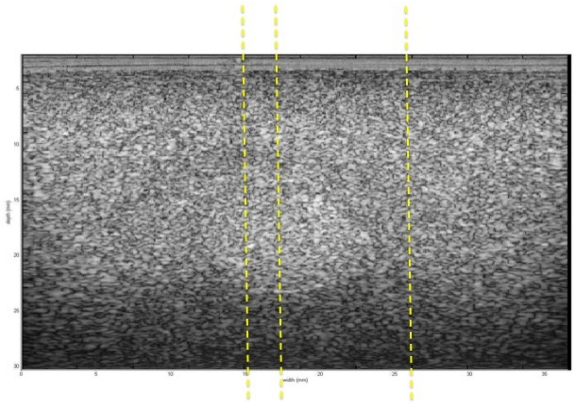

(b)

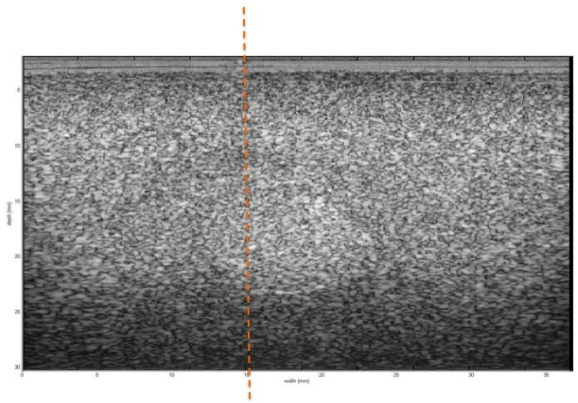

(c)

Figure 4.5: Algorithm flowchart: visualization. Part 1: seed selection. Seed candidates (a), Remaining seed candidates after slope criterion applied (b), Selected seed (c).

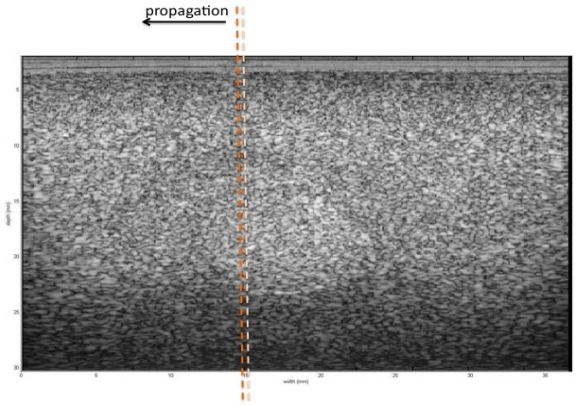

(a)

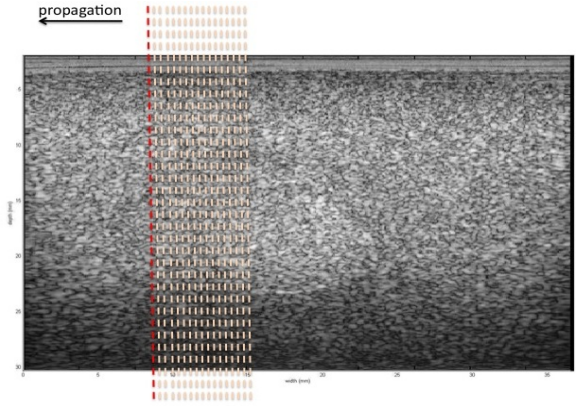

(b)

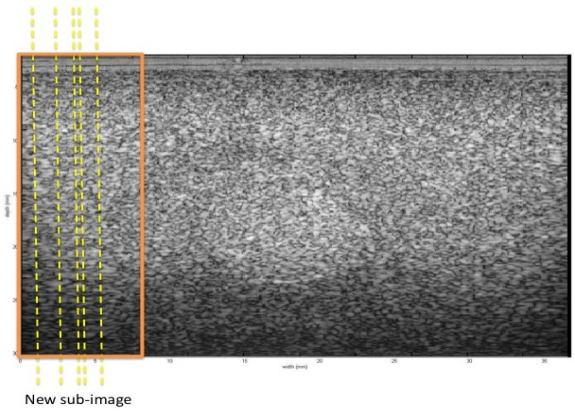

(c)

Figure 4.6: Algorithm flowchart: visualization. Part 2: Displacement propagation. Displacement estimation for the adjacent line pair (a), Displacement propagation continues until unsuitable line pair is encountered (b), A new sub-image is formed and with new seed candidates (c).

for line $j+1$ will be estimated according to equation 3.5, and then the same set of conditions will be used to asses the quality of the next RF line pair $j+2$. If the thresholds are not met, propagation stops and the remaining portion of the RF frame will be treated as a new sub-image I_{k+1}, where a new seed RF line will need to be selected (Figure 4.4).

4.2.4 Robust 3D elastography with multiple seed lines

For 3D displacement estimation we combine the frame selection algorithm of Foroughi et al [37] with the robust 2D methods presented above.

During freehand palpation using a tracked 3D ultrasound transducer, the Foroughi method automatically selects pairs of RF frames with minimal lateral and out-of-plane motions, and also has the possibility to select frames with a predefined compression range with respect to one another [37]. In the case of a 3D transducer, a volume is constructed by sliding a 2D linear array over the sector of a circle with radius r as shown in Figure 4.8. θ is the angle of the slice at each step of the wobbler motor. r and θ are known from the probe manufacturer specifications. As data is acquired while the 2D element array sweeps the volume, synchronized position in-

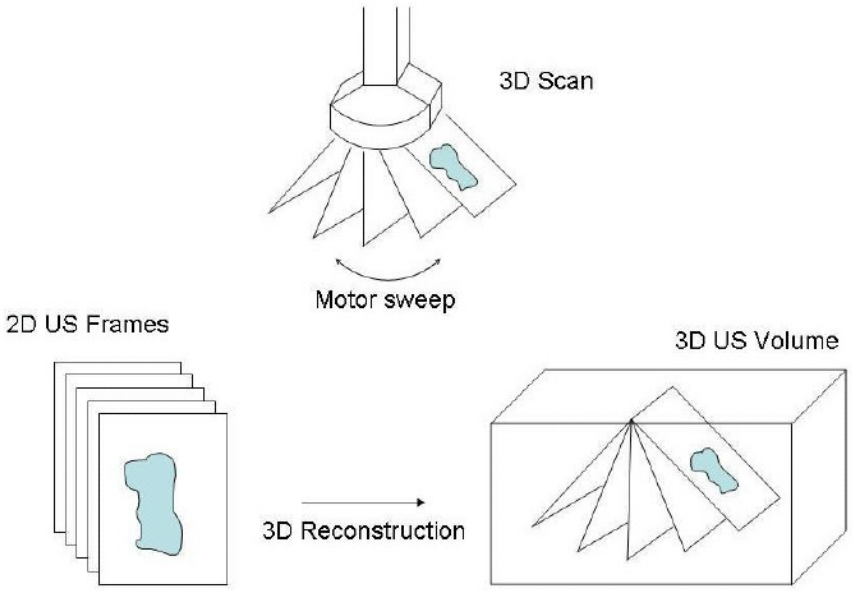

Figure 4.7: 3D wobbler transducer principles: data acquisition and 3D volume reconstruction.

formation is recorded simultaneously. A transformation matrix is computed which determines the position and orientation of every slice. The geometry of the probe and the acquisition angle of the slice determine each transformation matrix.

The position information helps select pairs of RF frames which have a high probability of producing good-quality strain images. The goal is to find frame pairs for which the motion is mainly in axial direction, with minimal lateral and elevational motion (Figure 4.8). Foroughi's solution is found by maximizing the following objective function [37]:

$$Crr(D) = exp(-K_x D_x^2 - K_y \frac{|D_y - topt|^3}{D_y + c} - K_z D_z^2) \tag{4.5}$$

where K_x, K_y, and K_z determine the sensitivity to motion in lateral, axial, and elevational directions respectively, and $D = [D_x D_y D_z]$ is the sample-wise root mean square of the displacement. t_{opt} represents the desired compression, and c is a small number that limits the cost of zero compression.

Due to the continuous freehand deformation, the axial direction for each acquired frame varies depending on the acquisition angle θ (Figure 4.8). Imperfect hand motion is generally an obstacle for elasticity algorithms. Foroughi et al [37] consider it however beneficial for their algorithm, because as they attempt to maximize the objective function for optimal compression in a given axial direction, they can evaluate every frame at the respective motor step location, but also the ones at one preceding and one succeeding location. The result is an improved strain quality at the center slice, and also at the adjacent slices [37].

While the frame selection technique resolves signal decorrelation due to out-of-plane motion, the robust 2D displacement estimation methods address small local decorrelations, which can be present only in a small number of frames in a swept volume. For example the presence of fluid (blood or lymphatic vessels, billiary ducts) in one frame can affect the entire 3D displacement estimation.

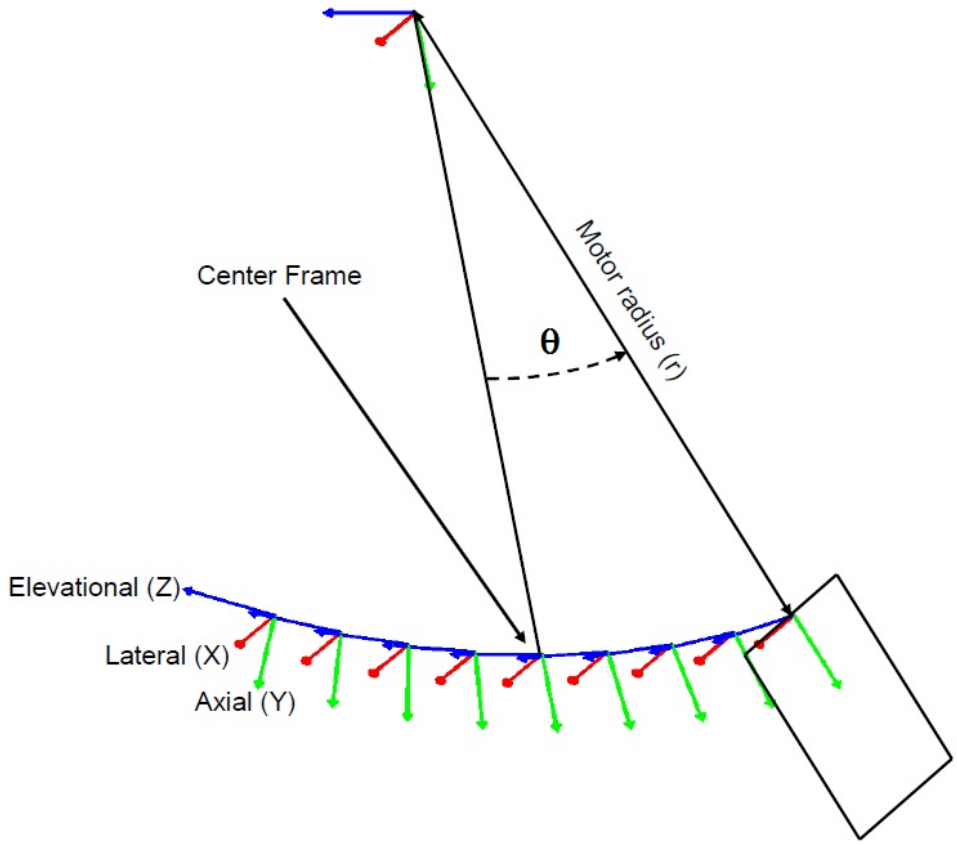

Figure 4.8: Overview of the TrUE approach. Given r and θ, each RF slice within a volume is localized. Courtesy of Foroughi et al [37].

The robust 2D displacement estimation is performed after the frame pair selection. The position of each frame is available to us from the tracking information, so we can use it to automatically adjust the search range for the DP part of the algorithm (ch. 3). This results in a faster integer displacement estimation for the selection of seed lines. A strain image is computed for each frame pair, then all frames are combined in one 3D strain volume by applying a scaling factor represented by a 3D smoothing kernel, weighted by the mean strain of each pair. To display the results, strain images are stacked and scan-conversion is applied to the resulting volume.

4.3 Results and Discussion

4.3.1 Displacement estimation in 2D phantom data

To study the choice of algorithm parameters and their impact, we palpated and scanned a CIRS (CIRS Inc. Norfolk, Virginia) breast elastography phantom model 059 (Figure 4.9). According to the manufacturer specifications, the phantom presented with a 10 mm diameter dense mass at least two times stiffer than the background, which had an elastic modulus of $20kPa \pm 5kPa$. The raw ultrasound data were obtained from ACUSON Antares (Siemens Medical Solutions USA, Malvern, PA, USA), while the tissue was palpated freehand using an ultrasound transducer (VF13-

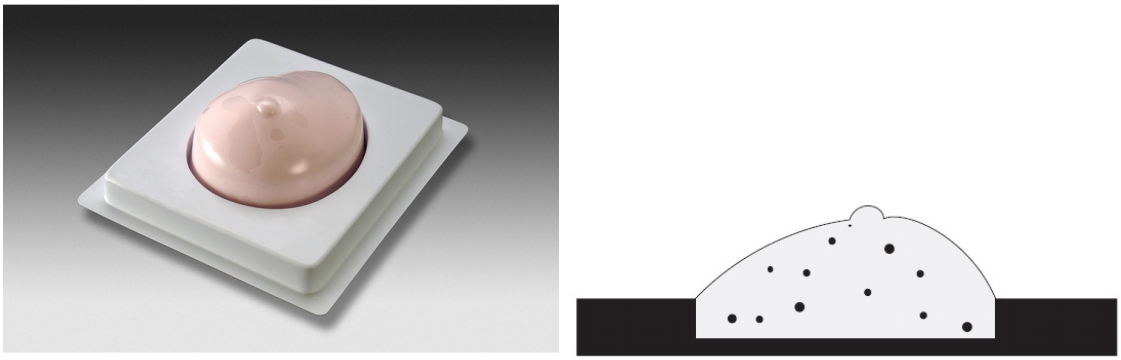

(a) (b)

Figure 4.9: CIRS breast phantom 059. The elasticity of each dense mass is at least two times greater than the elasticity of the background, which has an elastic modulus of $20kPa \pm 5kPa$. They range in size between 3 to 10 mm (b)

5SP) at a center frequency of 7.27 MHz. The Axius Direct Ultrasound Research Interface was used to enable RF acquisition at a sampling rate of 40MHz, with each frame comprising 508 lines of 1700 samples.

Two RF frames were selected which exhibited some unknown regions of poorly correlated RF data. In order to evaluate the magnitude of the problem, we first set out to evaluate the percentage of decorrelated RF line pairs. Integer displacements were estimated for each RF line pair using DP (eq. 3.3). Every line pair was treated as a seed and thus processed individually, using no prior information for an initial guess. Visualizing the individual axial displacements as a unified map makes it easy to observe potential discontinuities and poorly correlated areas (Figure 4.10 - arrows).

Further more, the choice of w value affects the final strain image (Figure 4.11).

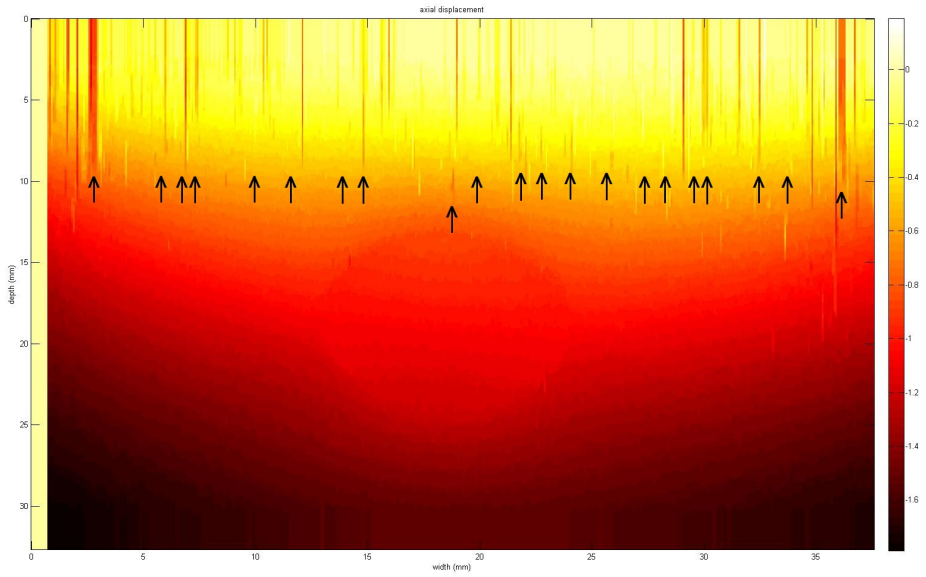

Figure 4.10: Breast phantom data. Integer displacement was estimated using dynamic programming method on each RF line pair (#13 - 498). Many areas prone to produce artifacts are relatively easy to identify (arrows).

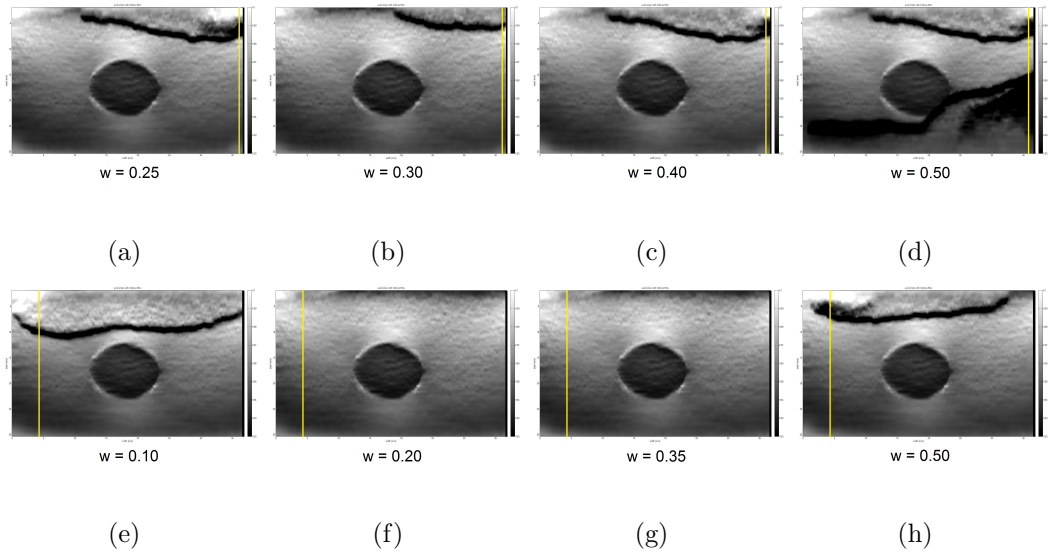

Figure 4.11: Examples of artifacts in strain images for various values of w. First row represents strain images originating from seed RF line #487, second row from seed RF line #55. Seed line is emphasized in color yellow.

Table 4.1: Percentage distribution for seed RF lines, given multiple values for w (smoothness regularization parameter)

	w										
Lines (%)	0.10	0.15	0.20	0.25	0.30	0.35	0.40	0.45	0.50	0.55	0.60
W/o artifacts	44.2	57.8	61.3	68.1	65.0	61.7	53.3	53.1	43.4	32.1	24.3
W/ artifacts	55.8	42.2	33.6	30.0	30.5	32.0	41.8	46.9	56.6	67.9	75.8
Indeterminate	-	-	5.1	1.9	4.5	5.3	4.9	-	-	-	-

In the DP displacement computation, w is a smoothness regularization parameter (eq. 3.3) intended to prevent poorly correlated regions from introducing errors in displacement estimation. 5346 strain images were obtained with the 2D AM method using each RF line as a seed, each for eleven values for w between 0.10 and 0.60. Knowing the shape and size of the expected lesion, we visually inspected each resulting elastogram for the presence of artifacts. Some lines produced very faint, very small artifacts on the order of a couple of pixels which were not propagated to the adjacent lines; if these artifacts were not easily identifiable at first inspection, the corresponding line was categorized as *indeterminate* (Table 4.1).

For the breast phantom data, we focused our remaining analysis on values of w in the 0.20 - 0.35 range, where over 60% of lines produced no strain artifacts (Table 4.1). For this w range, **113 (23.25 %)** lines produced artifacts for all four values of w (0.2, 0.25, 0.3, 0.35), **263 (54.12%)** lines never produced artifacts and **110 (22.63%)** lines varied in their behavior.

For values of w in the 0.20 - 0.35 range, at least 30% of lines presented artifacts. This value motivated our choice for parameters $p = 5$ and $q = 5$. The probability

that all $p = 5$ seed line candidates would be in decorrelated areas is very small ($0.3^5 = 0.0024$, implying at most a 0.24% probability that all 5 candidates would fail). Similarly, the choice of $q = 5$ random values for w in the selected range ensures a good low probability the seed line candidate would fail for all $q = 5$ values.

The monotone displacement slope criterion (Algorithm 1) was very effective as an initial test for filtering out most of the poorly correlated line pairs. As a filter by itself, it had a **74.18%** sensitivity and **77.78%** specificity.

The *instability* metric As (eq. 4.1) clearly differentiated between high quality data and regions of signal decorrelation (Figure 4.12). Our algorithm uses this metric to select from the seed candidates the line pair with the lowest AsI value. For our phantom study, robust lines exhibited values of As less than 5% (Figure 4.12).

Using the phantom data, we also evaluated the magnitude of the normalized cross-correlation $C(I_1(j), I_2(j))$ (eq. 4.2) as an indicator of the degree of matching between the pre- and post-compression data. The spread and distribution of $C(I_1(j), I_2(j))$ with respect to w is presented in Figure 4.13. Once again, w values in the 0.20 - 0.35 range resulted in a clear differentiation of robust vs. artifact producing lines. The results in Figure 4.13 determined our choice of values for correlation-guided displacement propagation. Lines where C or C_fwd less than $\tau_1 = 75\%$ or ρ is higher than $\tau_2 = 10\%$, signal the beginning of a poorly correlated data region, where prop-

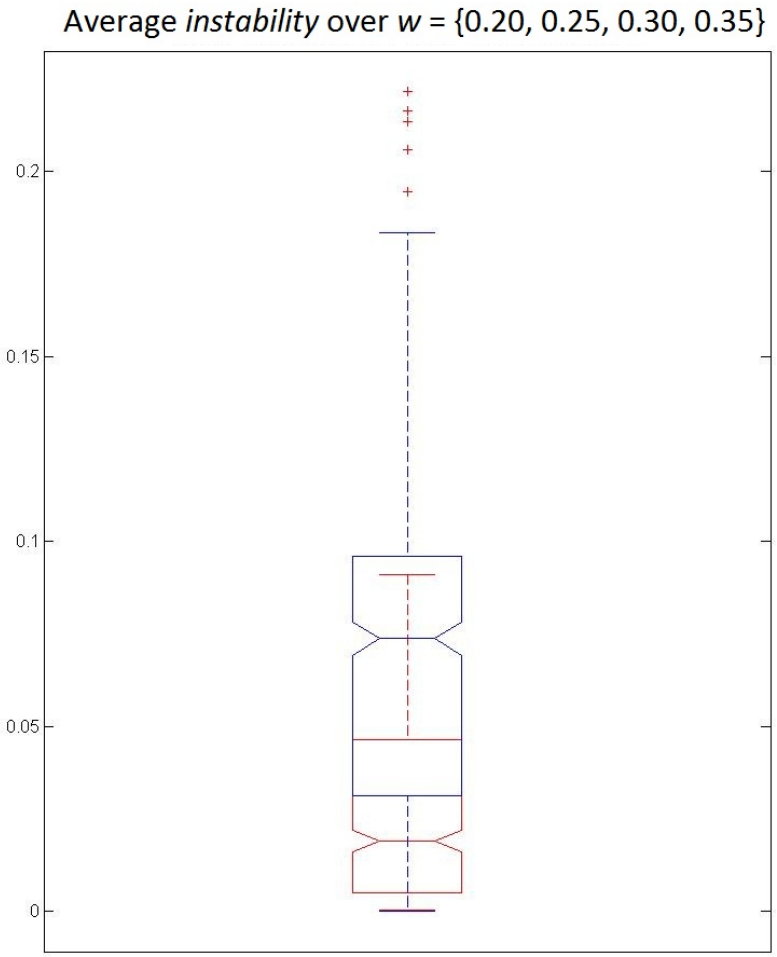

Figure 4.12: Box and whisker plot: *Instability* metric As (averaged over $w = 0.2$, 0.25, 0.3, 0.35). Values corresponding to the artifact producing lines are shown in blue while the robust lines are shown in red.

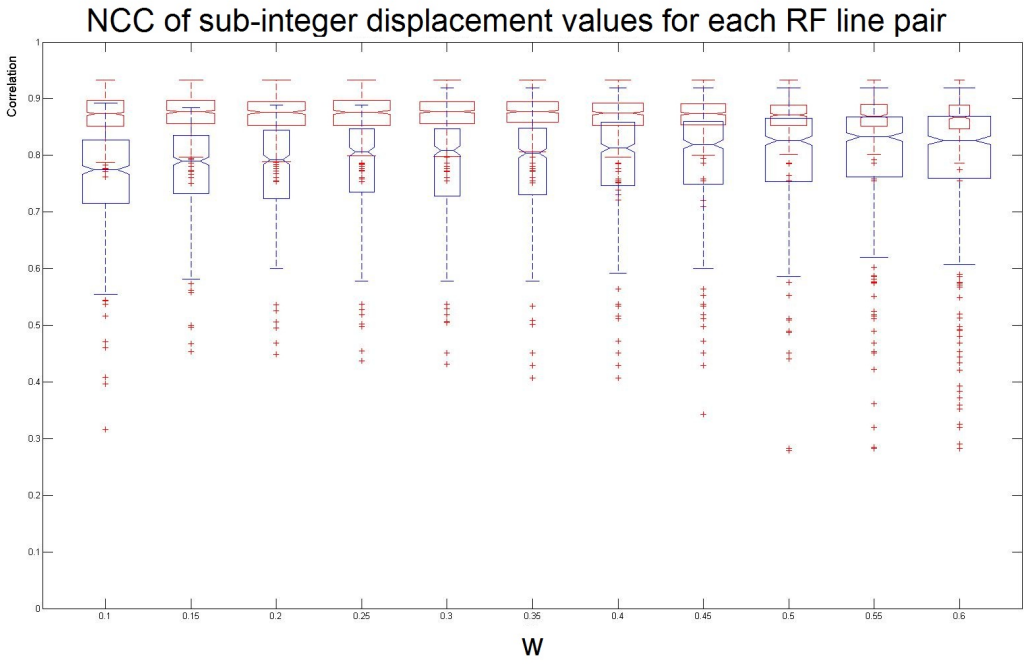

Figure 4.13: Box and whisker plot: magnitude of normalized cross-correlation C. Values corresponding to the artifact producing lines are shown in blue while the robust lines are shown in red.

agation will stop and a new seed RF line is necessary.

4.3.2 Displacement estimation in 2D human prostate *ex vivo* data

We re-evaluated the results of the study presented in Chapter 3, using the new robust tools. The results of the study using the original DP elastography algorithm by Rivaz et al ([93]) are presented in Chapter 3. Here we present improved results

from one specimen, for experimental validation of our algorithm on *ex vivo* data.

Ex vivo ultrasound data was collected from resected human prostates, following prostatectomy. In accordance with the Institutional Review Board approval, each prostate specimen also underwent a post-operative ultra high-resolution MRI at 9.4 Tesla. The RF ultrasound data were obtained from ACUSON Antares (Siemens Medical Solutions USA, Malvern, PA, USA), while the specimen was palpated free-hand using an ultrasound transducer (VF10-5) at a center frequency of 6.67 MHz. The Axius Direct Ultrasound Research Interface was used to enable RF acquisition at a sampling rate of 30MHz, with each frame comprising 350 lines of 2236 samples. Post-operative MR scans were used for anatomical correlation with the strain images.

Compared to the original study where we evaluated the efficacy of the DP elastography algorithm in uncovering hard tumors in the prostate gland, this time we focused on improvement on the displacement estimation values and in our ability to obtain artifact-free elastograms. Local areas of signal decorrelation resulted in artifacts when the original DP algorithm was used (Figure 4.1 a-b). The use of the robust tools resulted in an improved, artifact-free elastogram (Figure 4.1 c).

In order to quantify the improvement in the displacement estimation values, we calculated the ratio between new and old correlation values, line by line in the axial direction. Figure 4.14 c) shows the improvement in correlation values. 100%

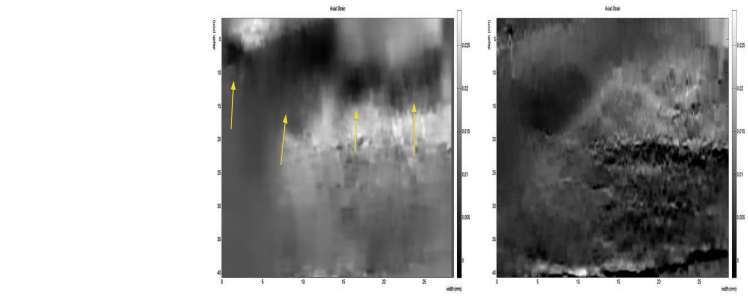

(a) (b)

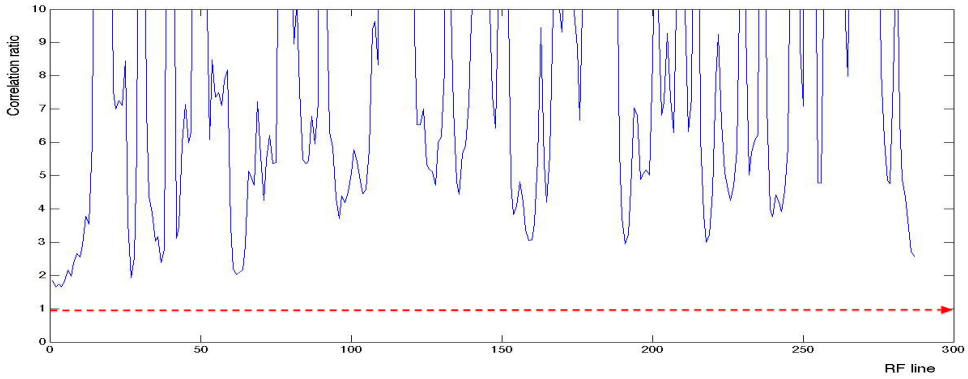

(c)

Figure 4.14: Improvement in estimated displacement correlation: original elastogram (a), improved, artifact-free elastogram with the addition of the robust tools (b) and correlation ratio line by line (c).

of the lines showed improved displacement estimation values, with new correlation improving from 1.7 to 12% over the original values (Figure 4.14).

The robust multi-seed algorithm was used for displacement estimation. w ranged from 0.20 to 0.35 for the seed selection step, and $\tau_1 = 75\%$ and $\tau_2 = 10\%$ for the displacement propagation step. We discuss in detail below how we dealt with two challenging situations. Note: the algorithm is designed to handle all the

steps/decisions mentioned in the situations below automatically.

1. Given sub-image I_k, one or more RF line pairs could be highly decorrelated, preventing displacement propagation and effectively stopping the progression of the algorithm. In this prostate data example, we considered the initial sub-image as the entire frame. RF line pair #146 was selected as seed (Figure 4.15 a, dotted line). During displacement propagation, the algorithm encountered two decorrelated regions indicated by values for C under the threshold τ_1 (see circled areas in Figure 4.15 a). The values for C_{fwd} agreed with C as they were also under the threshold τ_1(Figure 4.15 b, c). Two new sub-images were defined (I_{11} to the left and I_{12} to the right) for which the algorithm started anew by selecting new seed lines.

2. The second situation arises when in a remaining (small) sub-image, the RF data could exhibit such poor correlation that no line would fit the criteria for a robust seed selection. Pseudocode of the **automatic** handling of this situation is presented in Algorithm 2:

   - In our implementation, we maintain an array of size n containing the values of C for each RF line pair. They are initialized to 0 (zero) and, as each sub-image I_k is being processed, we update the values of C for each RF line pair (Alg. 2, lines 1-6).

   - When a seed selection is not possible, some lines remain unprocessed. After

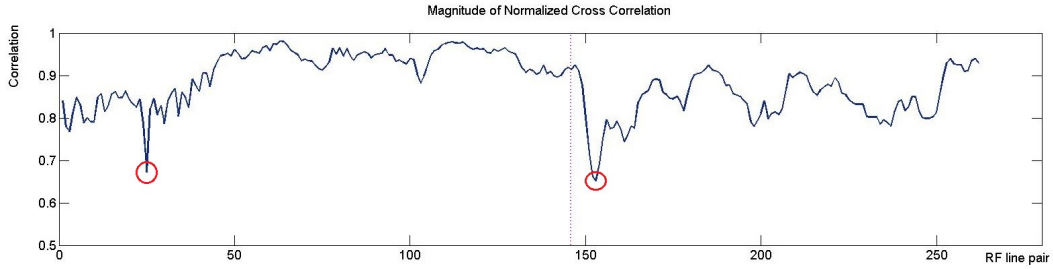

(a)

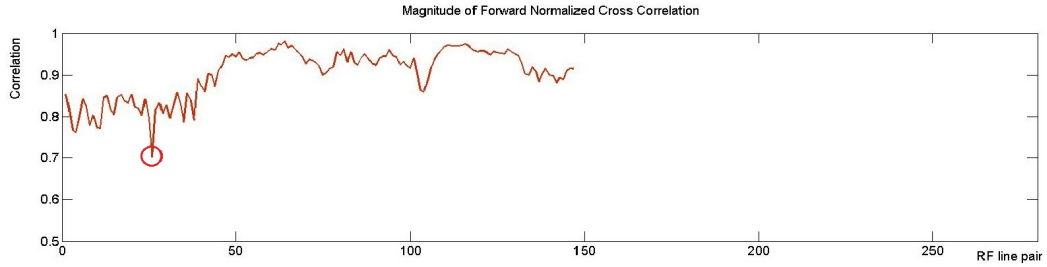

(b)

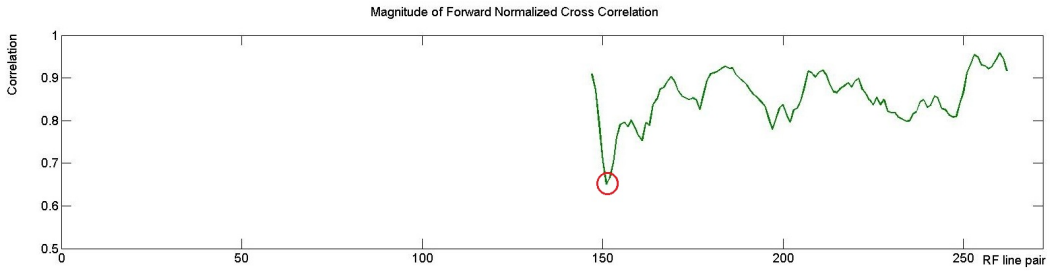

(c)

Figure 4.15: Prostate data set example: correlation values for each line pair (a), forward correlation for displacement propagation in I_{11} (b), and I_{12} (c). seed line is shown by dotted line in (a). Also shown are breaking points due to low correlation values (circles)

all sub-images finish propagation, a linear search is used for the detection of unprocessed lines (Alg. 2, lines 7-8).

- For each such line, a search is initiated to the left adjacent line until a line with a non-zero value of C is found (Alg. 2, lines 9-13).
- Same search is performed to the right adjacent line (Alg. 2, lines 14-18).
- C_{fwd} is calculated for the right and left lines bordering the sub-image without robust seed lines. The highest quality boundary determines which displacement values will be used for propagation (Alg. 2, lines 14-18). This insures possible small artifacts will be confined to small regions and will not impact the displacement estimate of other lines.

In our prostate data example, we needed to select a seed line in sub-image I_{11} defined to the left of the frame, consisting of thirty-four RF line pairs. Only one line pair passed the displacement slope criterion. Continuing on, our threshold τ_1 of 75% was not met, so we were left with a sub-image with no suitable seed line. The lines in I_{11} were processed at the very end, after the search revealed the presence of a sub-image without robust seed lines. The highest quality boundary was found to be line #35, so displacement was propagated from there towards line #1. The final strain image (incorporating the displacement values from sub-image I_{12}) is presented in Figure 4.16 b).

Algorithm 2 Propagate displacement in a sub-image with no suitable seed lines

$C[n] \leftarrow 0, 0, ..., 0$ ▷ initialization, number of lines = n
for $i = 1$ to n **do** ▷ during displacement propagation
  if $C_i > \tau_1$ **then**
    $C[i] \leftarrow C_i$ ▷ update the values as each line is processed
  end if
end for
for $i = 1$ to n **do** ▷ Detect unprocessed lines
  if $C[i] == 0$ **then**
    $j \leftarrow i$
    while $C[j] == 0$ **do**
      $j \leftarrow j - 1$ ▷ check the adjacent line to the left
    end while
    $left \leftarrow j$
    $j \leftarrow i$
    while $C[j] == 0$ **do**
      $j \leftarrow j + 1$ ▷ check the adjacent line to the right
    end while
    $right \leftarrow j$
    if $C_{fwd}[left] > C_{fwd}[right]$ **then**
      Propagate from left.
    else
      Propagate from right.
    end if
    $C[i] \leftarrow C_i$ ▷ update the values as each line is processed
  end if
end for

Figure 4.16 a) illustrates the importance of selecting a high value for threshold τ_1 in order to maintain high quality strain and to limit artifacts due to local decorrelation. In sub-image I_{11}, if we allowed a seed line to be selected with the highest C value, but lower than 75%, the resulting elastogram would present with an artifact (Figure 4.16 a) - arrow). Following through with our threshold of $\tau_1 = 75\%$ resulted in the elastogram Figure 4.16 b), eliminating the artifact.

4.3.3 Displacement estimation in 2D human liver ablation *in vivo* data

Seven patients undergoing open surgical RF ablation for primary or secondary liver cancer were enrolled in our study between February 06, 2008 and July 28, 2008 [2]. All patients had unresectable form of the disease and were deemed candidates for RF ablation following review at our institutional multidisciplinary conference. Patients with cirrhosis or sub-optimal tumor location were excluded from the study. All patients provided informed consent as part of the protocol, which was approved by the institutional review board. RF ablation was administered using the RITA Model 1500 XRF generator (Rita Medical Systems, Fremont, CA). Ultrasound imaging was per-

[2]The study was conducted under the supervision of Hassan Rivaz. The full results of the study using the original DP elastography algorithm were presented at the MICCAI and IEEE ultrasonics conferences in 2008 [94,95]. The data was reprocessed by Ioana Fleming in 2012 using the additional robust methods.

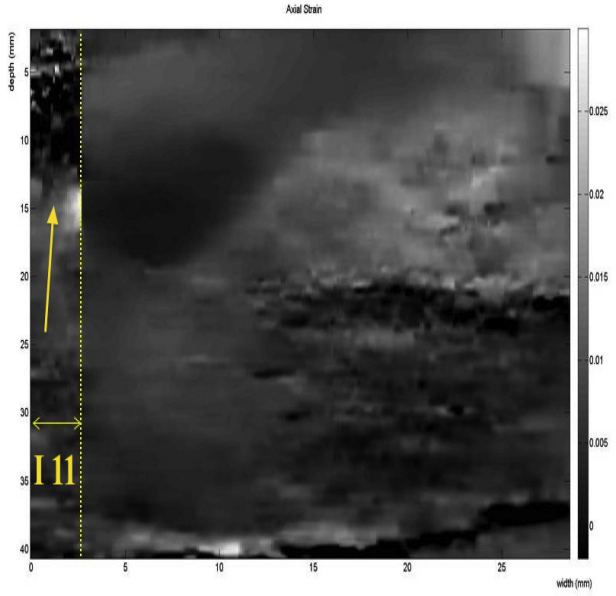

(a)

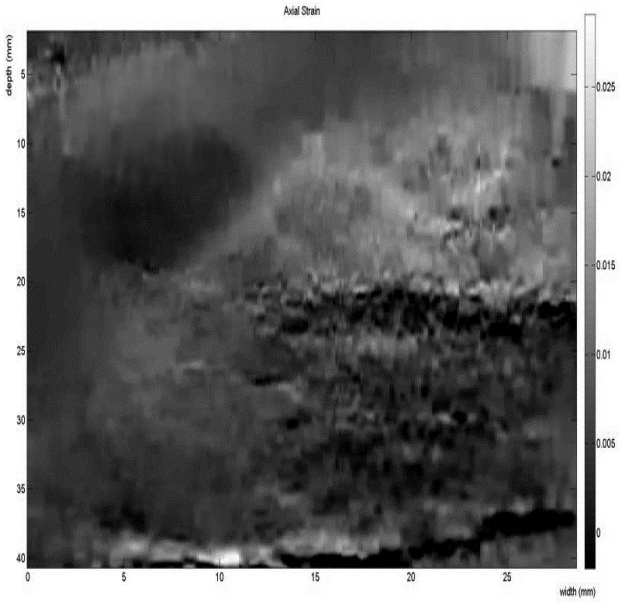

(b)

Figure 4.16: Prostate data set example: Illustration of a sub-image without robust seed lines. Sub-image I_{11} is defined at the left of the frame. (a) Elastogram with artifact (arrow) inside sub-image I_{11}, where the value of threshold τ is set lower than 75% , (b) $\tau = 75\%$. In the absence of any robust seed lines, displacement is propagated from the adjacent sub-image, resulting in an artifact-free elastogram.

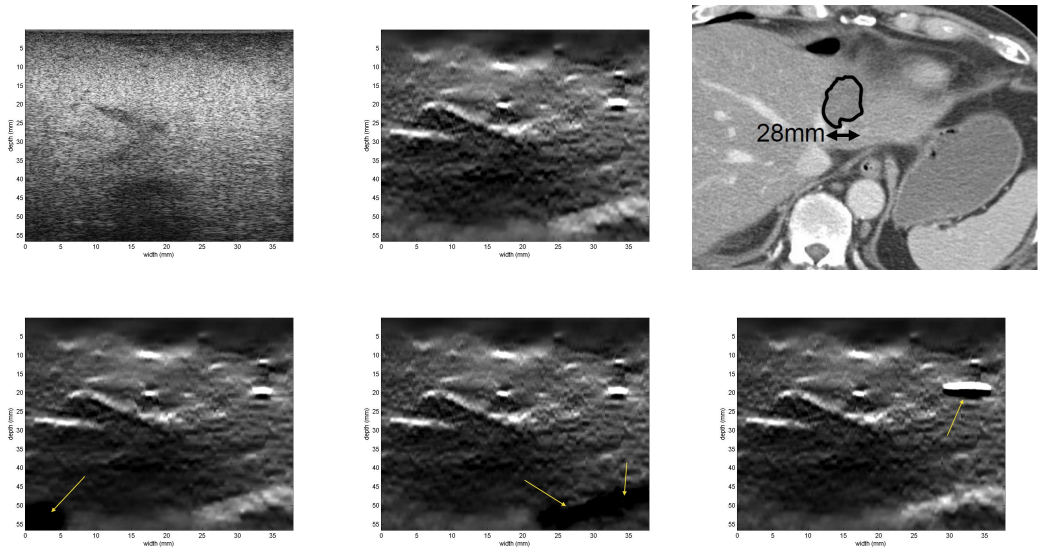

Figure 4.17: RF ablation therapy of liver cancer patient 2. All imaging was acquired after the ablation. B-mode (a), Elastography with the robust method (b) - The thermal lesion shows in as dark, surrounded by normal tissue in white., CT with delineated thermal lesions (c) and Elastography without the robust method (d-f).

formed after the ablation, where the hepatic tissue was compressed freehand through direct interrogation at a frequency of approximately 1 compression per 2 seconds, with no tracking hardware attached to the transducer. After the ablation, the patients underwent CT imaging to asses the size of the ablated area and the efficacy of the procedure.

Strain images were generated offline using acquired ultrasound raw RF data. The study's goal was to investigate elastography's ability to accurately asses the size and location of the ablation thermal lesion. The results of the study with the original DP algorithms were published in 208 [94, 95]. Here we look at the way the robust methods improved over the original Rivaz technique.

Conventional B-mode ultrasound was not enough on its own to asses the size and position of the thermal lesions. Some thermal lesions obscured the deeper structures in B-mode imaging, phenomenon known as *shadowing* (Figure 4.18 a), 4.17 a)). In addition, the thermal lesion has different appearances in the three B-scans. In strain images, the robust elastography algorithm uncovered the thermal areas very well as hard tissue (Figure 4.18 b), 4.17 b), 4.19 b)). After gross correlation between the delineated lesions on post ablation CT scan and the ablated areas in the strain images, the size of the thermal lesion appears to correspond well (Figure 4.18 c), 4.17 c), 4.19 c)). Note: the non-unity aspect ratio in the axes of the B-mode and strain images should be considered when comparing them to the CT scans. A more rigorous validation of the size and shape of the ablated area in the elastography image is necessary; a three dimensional estimate of the volume of the lesion would be more suitable for CT correlation.

We produced displacement estimates for the thermal lesions using Rivaz's technique [93, 92] (Figures 4.18, 4.17, 4.19, (d, e, f)), and also with the additional robust methods (Figures 4.18, 4.17, 4.19, b). The choice of seed RF lines in poorly correlated data regions results in artifacts which sometimes obscure the real lesion (Figures 4.18, 4.17, 4.19, d-f - yellow arrows).

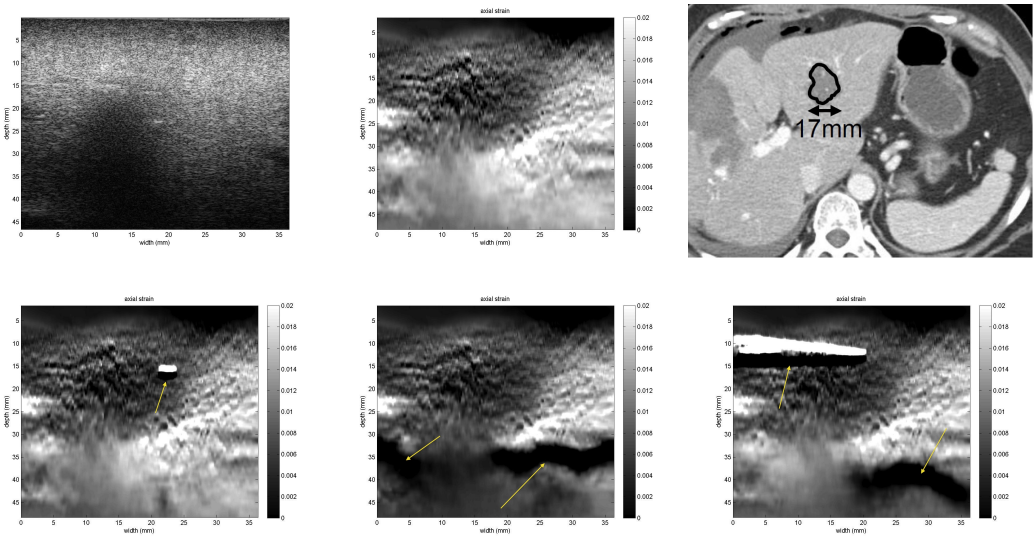

Figure 4.18: RF ablation therapy of liver cancer patient 1. All imaging was acquired after the ablation. B-mode (a), Elastography with the robust method (b) - The thermal lesion shows in as dark, surrounded by normal tissue in white., CT with delineated thermal lesions (c) and Elastography without the robust method (d-f).

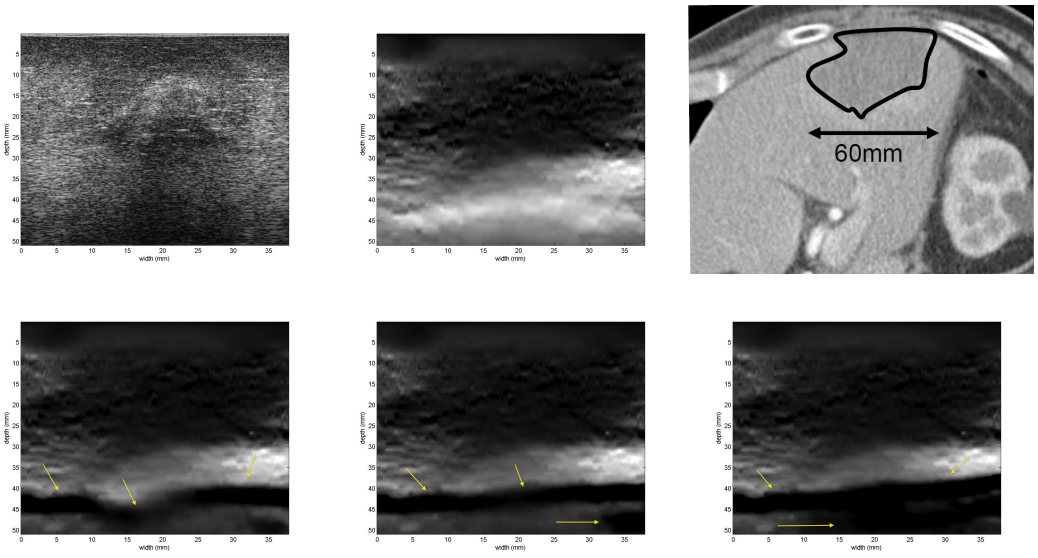

Figure 4.19: RF ablation therapy of liver cancer patient 3. All imaging was acquired after the ablation. B-mode (a), Elastography with the robust method (b) - The thermal lesion shows in as dark, surrounded by normal tissue in white., CT with delineated thermal lesions (c) and Elastography without the robust method (d-f).

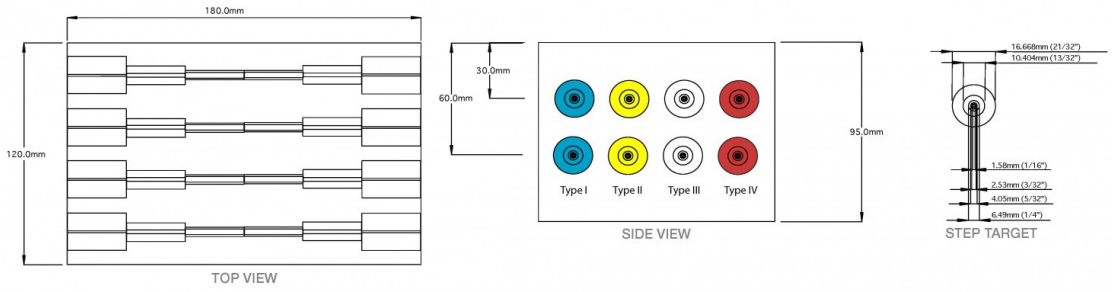

Figure 4.20: Elastogrpahy phantom (CIRS, Norfolk, VA) model 049a, presents multiple stepped cylinders of varying diameters and levels of stiffness.

4.3.4 Displacement estimation in 3D Phantom Data

For 3D evaluation we palpated and scanned a CIRS (CIRS Inc. Norfolk, Virginia) phantom, model 049A (Figure 4.20). The ultrasound data were obtained from SonixCEP ultrasound system (Ultrasonix Medical Corp., Richmond, BC, Canada). The phantom was palpated freehand using the $4DL14-5/38$ transducer at a center frequency of 6.7 MHz. A passive marker was attached to the transducer and was tracked using the Polaris optical tracker (Northern Digital Inc., Waterloo, Ontario, Canada). To enable continuous acquisition of RF data and synchronized tracker readings through the Ultrasonix Research Interface, we used the customizable in-house MUSIIC software platform [111, 52]. The volumes consisted of either 120 or 60 slices. Approximately 15 forward sweep scans were collected for each series of volumes.

Phantom model 49a includes four types of cylinders with varying diameters (Figure 4.20). Our 3D scan captured three of these cylinders with an elasticity of

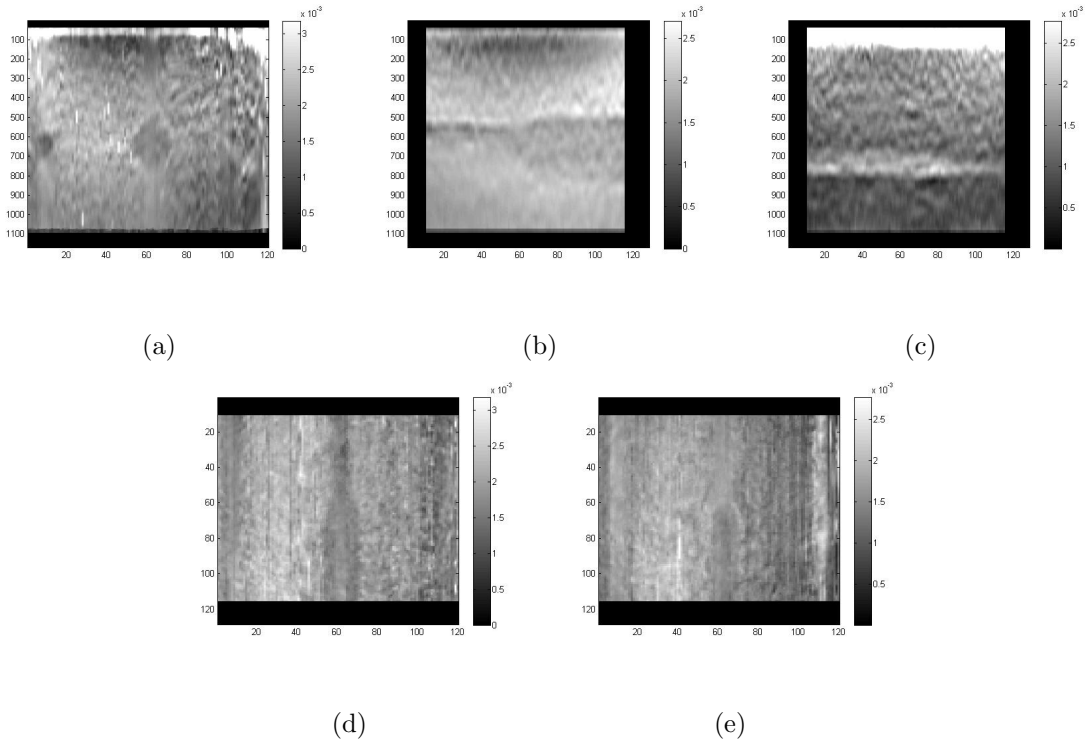

(a) (b) (c)

(d) (e)

Figure 4.21: Phantom model 49a: the cross-section of all three cylinders with different elasticity values can be detected in the elastogram. (a) From left to right, the elasticity of the cylinders is 80 kPa, 45 kPa and 14 kPa, vs. 25 kPa for the background. The harder cylinders appear darker and the softer one appears brighter than the background. (b) middle hard cylinder in axial-lateral view, (c) soft cylinder in axial-lateral view, (d) middle hard cylinder in elevational-lateral view, (e) soft cylinder in elevational-lateral view.

80 kPa, 45 kPa and 14 kPa, vs. 25 kPa for the background. It is interesting to observe that our algorithm captured both the harder and the softer cylinders (Figure 4.21). The harder cylinders appear darker and the softer one appears brighter than the background. This is important as it underscores the advantages of being able to produce a strain volume which shows both soft and hard lesions, using the maximum range of the wobbler probe.

4.3.5 Displacement estimation in 3D in vivo porcine liver ablation data

In the *in vivo* experiment, a pig was prepared to undergo liver ablation surgery[3]. After gaining access to the liver, an ablation needle was placed in a thick portion of the liver under ultrasound guidance. The hepatic tissue was ablated using the RITA ablation device (RITA Medical Systems Inc, Mountain View, California). The resulting thermal lesions were 1 to 2 cm in diameter. The ablated zone was then scanned following the approved protocol during a breath-hold period which lasted less than 20 seconds (Figure 4.22(a)). The strain scans of the two thermal lesions appear in Figure 4.22 d-i, where the ablated regions are clearly visible. The first ablation appears to be smaller than the second one which was confirmed by the gross-pathology (Figure 4.22(b), 4.22(c)). The diameter of the first lesion is about 1.5 cm whereas the second lesion is closer to 2 cm. The surgical gauze placed underneath the liver has created some distortion in the deeper parts of the scans (Figure 4.22(e)).

[3]The study was conducted under the supervision of Pezhman Foroughi. The full results of the study were presented in 2013 [37]. The elastography algorithm used for these results included some of the early versions of the robust methods. The data was reprocessed by Ioana Fleming in 2013 using the additional robust methods developed.

4.4 Conclusion and future work

We have proposed a robust method for displacement estimation in ultrasonic strain imaging. This method enhances the dynamic programming approach to displacement estimation, improving its ability to overcome displacement discontinuities and regions of poorly correlated RF data. The innovative methods proposed for seed line selection focus on robustness as well as stability over varying algorithm parameters. The method also addresses the robustness of displacement propagation using analytic minimization. The new algorithm is one step closer towards achieving repeatable, user-independent elastograms[4].

[4]Enforcing robustness and stability should not add a significant overhead to the total run-time of the displacement algorithm. After the initial DP integer displacement estimation on the seed line, the method is highly parallelizable at every step, from the seed selection tools to the displacement propagation.

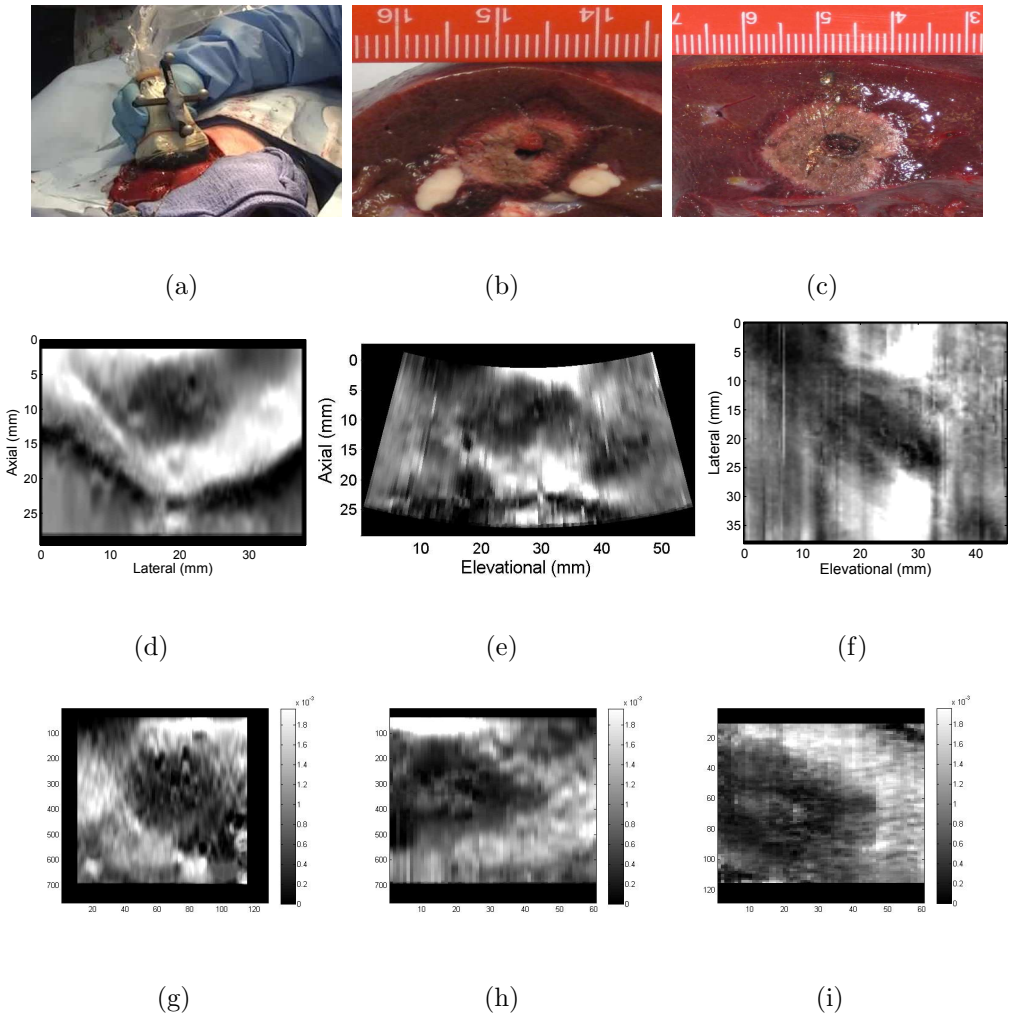

Figure 4.22: *Ex-vivo* hepatic ablation. (a) 3D transducer positioned on top of liver during elastography scan; (b) and (c) Cross-sections of the ablated regions with ruler visible; (d-f) Middle cross-sections of strain volume for ablated lesion #1 and (g-i) lesion #2.

Chapter 5

Ultrasound Elastography Mosaicking

5.1 Background

Compared to other imaging modalities like CT and MR, ultrasound suffers from a limited field of view. Monitoring a structure can be particularly challenging when it is too large to be visualized in a single image or 3D sweep. Size and distance measurements are unreliable in large organs. Panoramic imaging is emerging as a prevalent technique used in widening the field of view (FOV) of medical ultrasound

images. The ultrasound mosaic (also referred to as stitching) aims to achieve several clinical advantages which come along with extended FOV:

1. improving the understanding of spatial relationships among structures when the size of a single image/volume is not large enough to cover the entire area,
2. allowing for measurements of size and distance in large organs and lesions,
3. allowing multi-modal registration and fusion with pre-operative data for guidance in minimally-invasive interventions.

In this work we focus on extended FOV displacement estimation with the goal of creating 2D and 3D elastography mosaics. Elastography maps the mechanical properties of tissue which can add valuable features to the B-mode panorama. Many clinical applications deal with large cancerous lesions which expand beyond the span of one ultrasound image [40]. An ultrasound elastography mosaic can improve the understanding of the size of the lesion and its layout among surrounding structures. In the ablation of hepatic cancerous tissue, the size of the HIFU-induced ablative lesions often exceeds 4 cm in diameter, which is the width of a typical ultrasound transducer. Thermal lesions are not visible in conventional B-mode ultrasound but a panoramic ultrasound elastogram can help visualize and monitor the entire ablation area [126]. In the assessment of venous thrombi, a combination of ultrasound B-mode and Doppler imaging help detect the presence of the blood clot, but it is elastography which can

provide its age and clinical grading [29]. An in-plane ultrasound elastography mosaic can provide mapping of the thrombi all along the femoral vein. It could take up to eight mosaicked volumes to depict an entire organ like the liver or kidney [88]. Having the corresponding elastography mosaic would allow for registration with pre- and post-operative imaging data (CT or MRI) which would help with intra-operative navigation and also with the assessment of treatment efficacy.

Multiple approaches have been published in the literature on 2D and 3D wide FOV ultrasound mosaics [41, 88, 127, 90], but very little of this literature concerns registering the underlying strain field. As various sources of decorrelation are usually affecting the computation of strain images, this problem becomes even more important when attempting to generate a unified, wide displacement field. Furthermore, most elastography algorithms result in qualitative strain; two image pairs with even very slightly different degrees of compression will produce two strain images in which different structures could be visible. Another problem rises in the ambiguity of the interpretation of strain images: low strain can be indicative of high stiffness but this interpretation may not be the right one if the stress field is not uniform throughout the tissue [82,62]. To address these issues and to improve the quality of strain images, several metrics of stability, consistency/persistency and reliability have been developed [63, 51, 36]. Here we propose using techniques and tools developed in Chapter 4 to select a stable pair of RF lines which will become the starting point for generating

a reliable, wide FOV displacement field. Displacement on the seed line pair is calculated using dynamic programming and later propagated in both lateral directions of the mosaic using an analytic minimization approach [92]. Each new image pair adds to the unified displacement field. For proof of concept and validation, we present 2D and 3D elastography mosaics of tissue-mimicking phantom data acquired under a controlled laboratory setup.

5.2 Methods

Consider a sequence of radio frequency (RF) data (I_{11}, I_{12}) collected at position t_0, before and after the compression of tissue using a 2D ultrasound transducer (Figure 5.2(a)). Each sequence is contains n RF lines of length m. A second sequence (I_{21}, I_{22}) is collected (Figure 5.2(b)) after the transducer has been moved in the lateral direction of the probe to position t_1, with the help of a moving stage (Figure 5.1). A vertical stage was used to achieve an almost identical compression rate between the two sequences. The translation between the two image sequences in the controlled setup has only one component in the lateral direction of each RF frame:

$$T_{lines} = T_{mm} * n/w \tag{5.1}$$

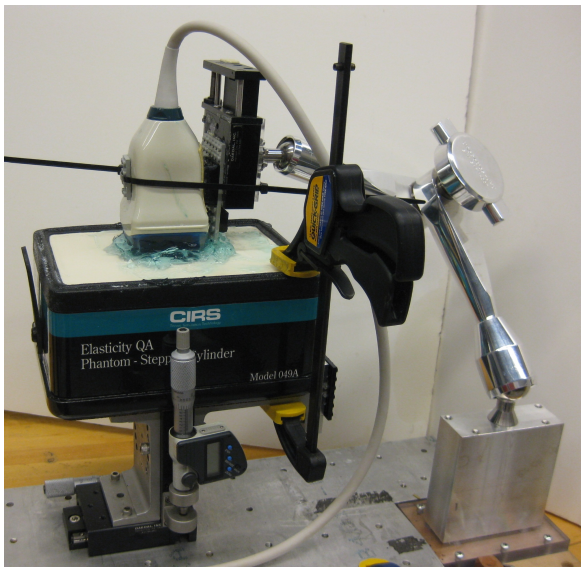

Figure 5.1: Experimental setup.

where w is the width of the ultrasound transducer in millimeters (mm), n is the number of RF lines, T_{mm} is the ground truth translation in mm as read on the stage and T_{lines} is the corresponding translation as number of RF lines. The overlap area consists of (n - T_{lines}) RF lines (Figure 5.3).

5.2.1 2D Pair-wise Mosaicking

The Analytic Minimization (AM) displacement estimation algorithm by Rivaz [92] has been described in Chapter 4. Integer displacements are first obtained using dynamic programming (DP) on a single pair of RF lines and then refined to sub-pixel values using AM (eq. 3.4). They are then propagated laterally, column to column,

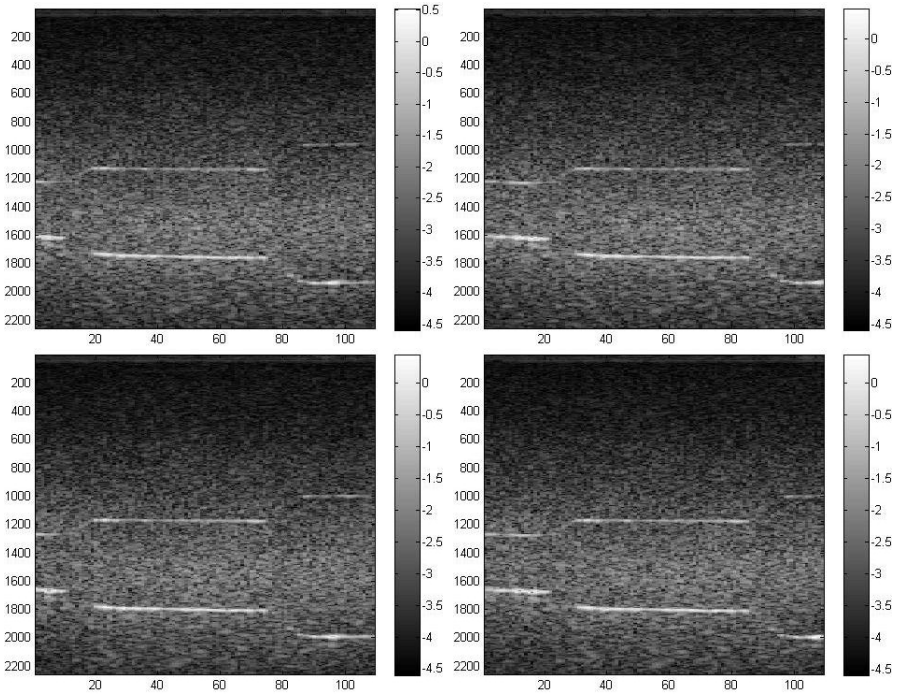

(a) (b)

Figure 5.2: Bmode ultrasound data before and after compression for (a) position t_0, and (b) position t_1.

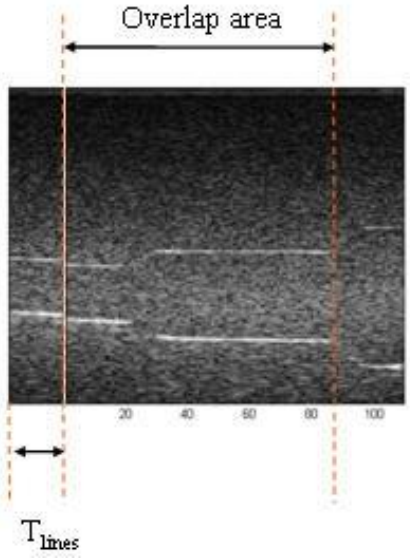

Figure 5.3: Bmode ultrasound data: translation T_{lines} and the length of the overlap area.

to produce 2D subsample displacements for the entire image (eq. 3.5) . For pair-wise mosaicking, we aim to find a robust and stable seed RF line in the overlap area which will serve as the initial guess in the AM propagation.

5.2.1.1 Algorithm Overview

Pair-wise strain mosaicking is implemented as follows:

1. A robust seed RF line from the overlap area is selected using the tools presented in chapter 4, section 4.2.1 (Figure 5.4-a, b, c).

2. At the end of the sub-integer displacement estimation process on each pair of RF lines, $(A_i = a_i + \Delta a_i)$, $(L_i = l_i + \Delta l_i)$ are the axial and lateral displacements at each sample i. The magnitude of the normalized cross-correlation is used to assess the degree of matching between the pre- and post-compression data.

$$C(I_1(s), I_2(s)) = \left| \frac{\sum_m^{i=1} (I_1(i,s) - \bar{I_1})(I_2(i+A_i, s+L_i) - \bar{I_2})}{\sqrt{\sum_m^{i=1} (I_1(i,s) - \bar{I_1})^2 \sum_m^{i=1} (I_2(i+A_i, s+L_i) - \bar{I_2})^2}} \right| \tag{5.2}$$

where $\bar{I_1}$ and $\bar{I_2}$ are the means of RF values along the seed line s. The value of C are used as an additional check to verify if the displacement estimate for the selected seed line is a good fit. If C value falls below a certain threshold $\tau_1 = 75\%$, the seed line would be deemed not suitable and the next stable seed

line would be selected (Figure 5.4-c).

3. Sub-integer displacements values are calculated for seed line s.

4. The sub-integer displacement values are propagated using AM (Figure 5.4-d):

   - in one sequence towards the first RF line,
   - in the second sequence towards the last RF line.

   The unified displacement field will have $n + T_{lines}$ RF lines and the stitching will be at RF line number $s + T_{lines}$ (Fig. 5.5-a).

5. Generate the ultrasound elastography mosaic from the unified displacement field (Fig. 5.5-b).

5.2.2 2D Multi-image Mosaicking

Given an existing n_t wide displacement map, computed for image pairs 1 through t, our goal is to expand the displacement map to include information from image pair $t + 1$. Assuming the ultrasound transducer has been translated towards the 1st RF line (Figure 5.2), and the same compression was applied for image pair $t+1$ as for the previous t pairs, we compute the unified displacement field as follows:

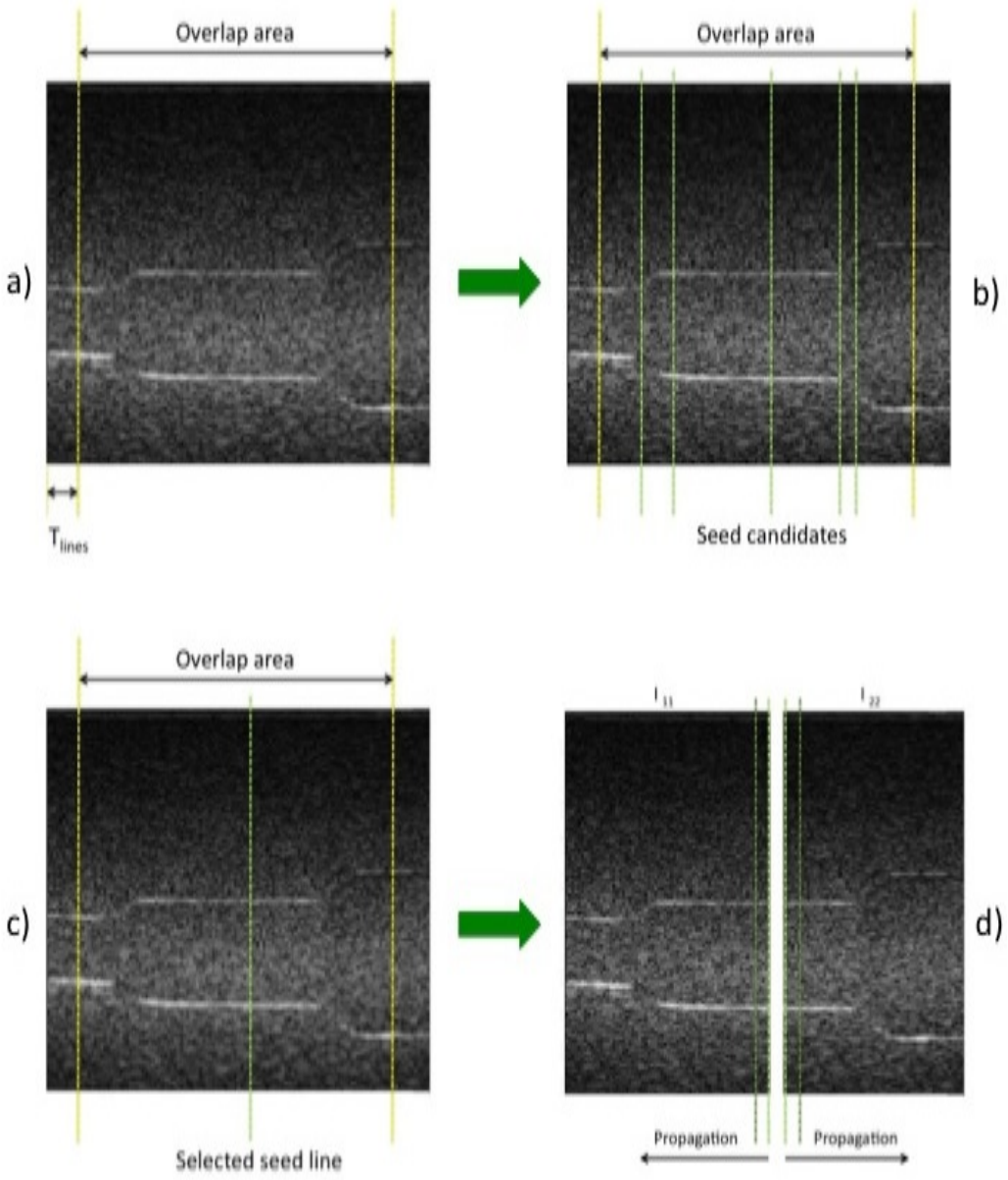

Figure 5.4: Pair-wise Mosaicking workflow: (a) overlap area, (b) candidate seed lines, (c) seed line selection, (d) displacement propagation in the two sub-images.

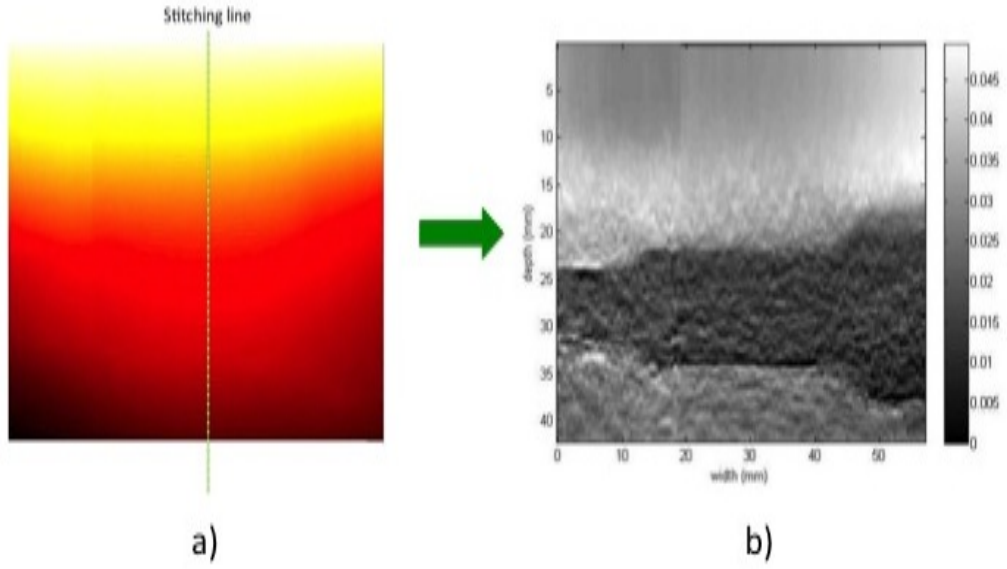

Figure 5.5: Pair-wise Mosaicking workflow, continued: (a) displacement is stitched along the seed line and, (b) the mosaicked elastogram is obtained from the unified displacement field.

5.2.2.1 Algorithm Overview

1. Compute the translation T_{lines}^{t+1} between position t and position $t+1$ and the overlap area.

2. Select the seed RF line s_{t+1} in the new overlap area.

3. Use the subinteger values from the wide FOV displacement map at RF line number $s_{t+1} + T_{lines}$ as initial values to refine and propagate displacement:

   - only in the new sequence towards the first RF line.

Stitch the newly computed $(s_{t+1} + T_{lines})$ lines at the beginning of the previous displacement map. The new mosaicked displacement field will have $n_t + T_{lines}^{t+1}$ RF lines.

4. Generate the new ultrasound elastography mosaic from the updated displacement field.

5.2.3 3D Elastography Mosaicking

In the 3D case, a pair of ultrasound RF volumes (V_{11}, V_{12}) were collected at position t_0, before and after the compression of tissue using a 3D ultrasound wobbler transducer similar with the one used in Chapter 4 (Figure 4.7). Each volume contains k frames and each frame has n RF lines of length m. One or more subsequent pairs of volumes are collected after the wobbler transducer is moved in the lateral direction of the probe with the help of a moving stage. Once again, a vertical stage was used to achieve an almost identical compression rate between the two sequences (Figure 5.1). Using the lateral and axial stages ensures the first frame of the first volume pair is aligned with the first frame of each subsequent pair volume, and all the other frames are similarly aligned, with no out-of-plane motion between each position. The same steps of multi-image mosaicking can be applied on a frame by frame basis, resulting in an unified displacement field for each elevational position of the wobbler motor.

Note: Here we employed a fixed rigid setup to control the acquisition of 3D ultrasound data for the proof of concept of 3D strain mosaics. In a routine 3D ultrasound exam, using stages to control the imaging of a certain human organ or tissue is not feasible. This limitation of our mosaicking algorithm can be addressed by making use of an ultrasound probe equipped with a tracking device [37]. As electromagnetic trackers become integrated into ultrasound transducers, one could use the tracking information to select ultrasound volumes with aligned frames and no out-of-plane rotation. In the literature of 3D ultrasound mosaics (B-mode only), Poon et al. ([88]) have used an ultrasound wobbler probe in combination with a position tracking system. The tracking information was used as an initial estimate for the position of the ultrasound volumes. Further refining is achieved later using a block-matching intensity-based registration.

Using also a wobbler tracked probe, Foroughi et al [37] have successfully implemented and tested a frame selection algorithm which selects pairs of images with an optimal amount of deformation for strain calculation. The work presented here makes a case for in-plane mosaicking where lateral translation is the only component of the transformation between two ultrasound volumes. The Foroughi algorithm ([37]) can select co-planar frame pairs which can be suitable for generating 2D elastography mosaics using the technique described in this thesis. To account for uneven rates of compression between frame pairs and also for potential tracker error, the al-

gorithm performs a fast search for the global deformation and then applies a motion compensation factor to each frame pair.

5.3 2D Mosaicking Experimental Setup

For experimental validation we palpated a CIRS (Norfolk, VA) elastography phantom model 049a using a high-frequency ultrasound transducer (L14-5W/60) at center frequency of 10 MHz (Figure 5.1). Ultrasound RF data was acquired from an Ultrasonix system (Vancouver, BC) at 40MHz sampling rate. The CIRS phantom model 049a consists of a series of stepped cylinders of varying diameters (Figure 4.20). The transducer was placed on top of one of the cylinders, parallel with its direction. The phantom was placed on a stage which controlled the compression in the axial direction and the translation in the lateral direction (Figure 5.1). RF data sequences were acquired from four axial compression levels ($c_0 = 0$, $c_1 = 2.54$ mm, $c_2 = 5.08$ mm, $c_3 =$ back to 0), for each of four lateral translation positions of the transducer ($t_0 = 0$, $t_1 = 5.08$ mm, $t_2 = 10.16$ mm, $t_3 = 20.32$ mm), for a total of sixteen data sets. The width of the ultrasound transducer L14-5W is 59 mm, and as a consequence any two sets were separated by a minimum lateral translation overlap of 38.68 mm.

Ultrasound elastography images were obtained for each translation position t_0

- t_3 ((Fig. 5.6a-d). A pairwise elastography mosaic was produced from positions t_0 and t_1 (Fig. 5.7 - a), and then multi-image elastography mosaics from positions t_0, t_1 and t_2 (Fig. 5.7 - b), and t_0, t_1, t_2 and t_3 (Fig. 5.7 - c).

5.3.1 Validation

Mosaicking more than two images is usually accomplished by stitching together pairwise aligned images. The drawback to this technique is that while processing a new pair in the pipeline, registration errors can be accumulated leading to a false global alignment the end. If we combine (accumulate) all the pairwise transformations between consecutive images, we don't arrive to the same result as by computing the transformation between the first and last images.

Simultaneous registration of multiple images is an area of active research in computer vision and have been recently used successfully in 3D B-mode ultrasound registration ([127]). The accumulation of transformation error is a potential drawback of our approach. To quantify the extent of this error, we compared the unified displacement map between positions t_0 and t_3 (Figure 5.8 a) with the displacement field computed by pairwise mosaicking of positions t_0, t_1, t_2 and t_3 (Figure 5.8 b). We aimed to quantify the possible quality loss due to the accumulation of transformation errors in the pairwise approach by looking at the differences (in pixels) between the

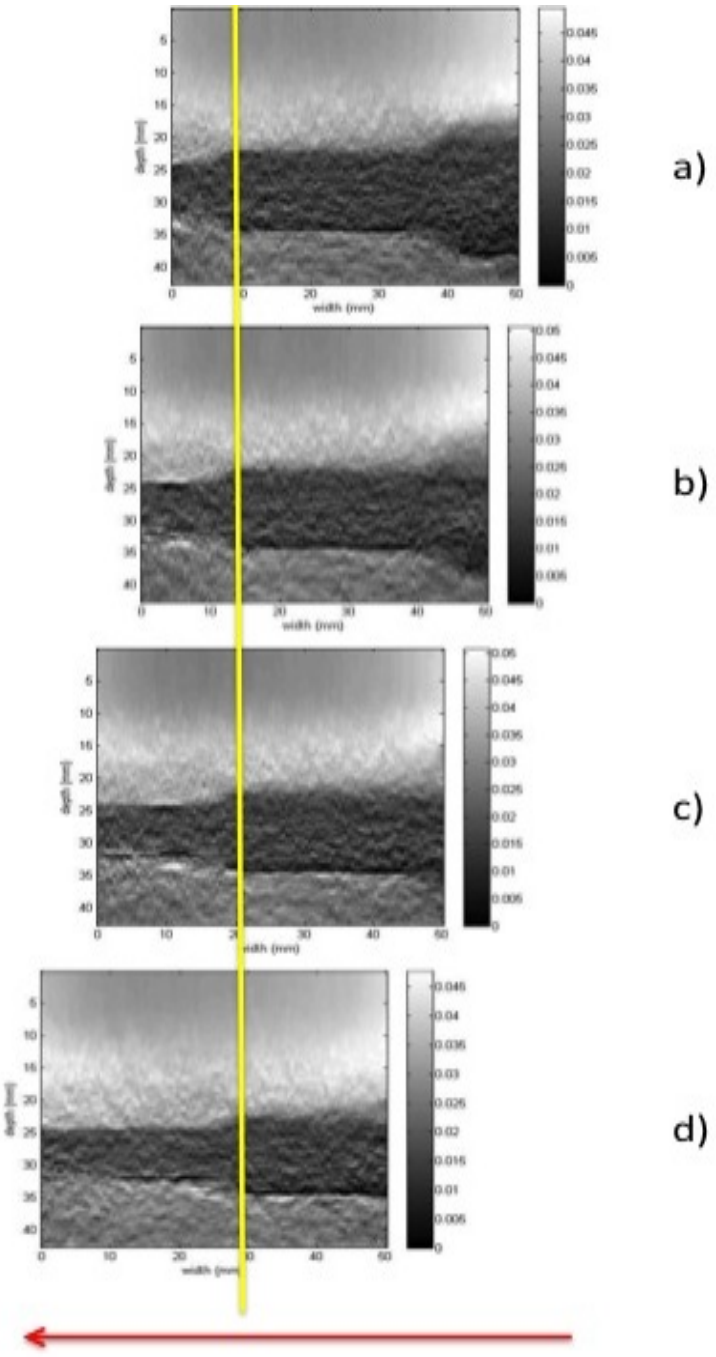

Figure 5.6: Ultrasound elastography from data acquired at position t_0 (a), t_1 (b), t_2 (c), t_3 (d). Yellow line represents a reference line to illustrate the motion between the positions. Red arrow shows the transducer's direction of motion during data acquisition.

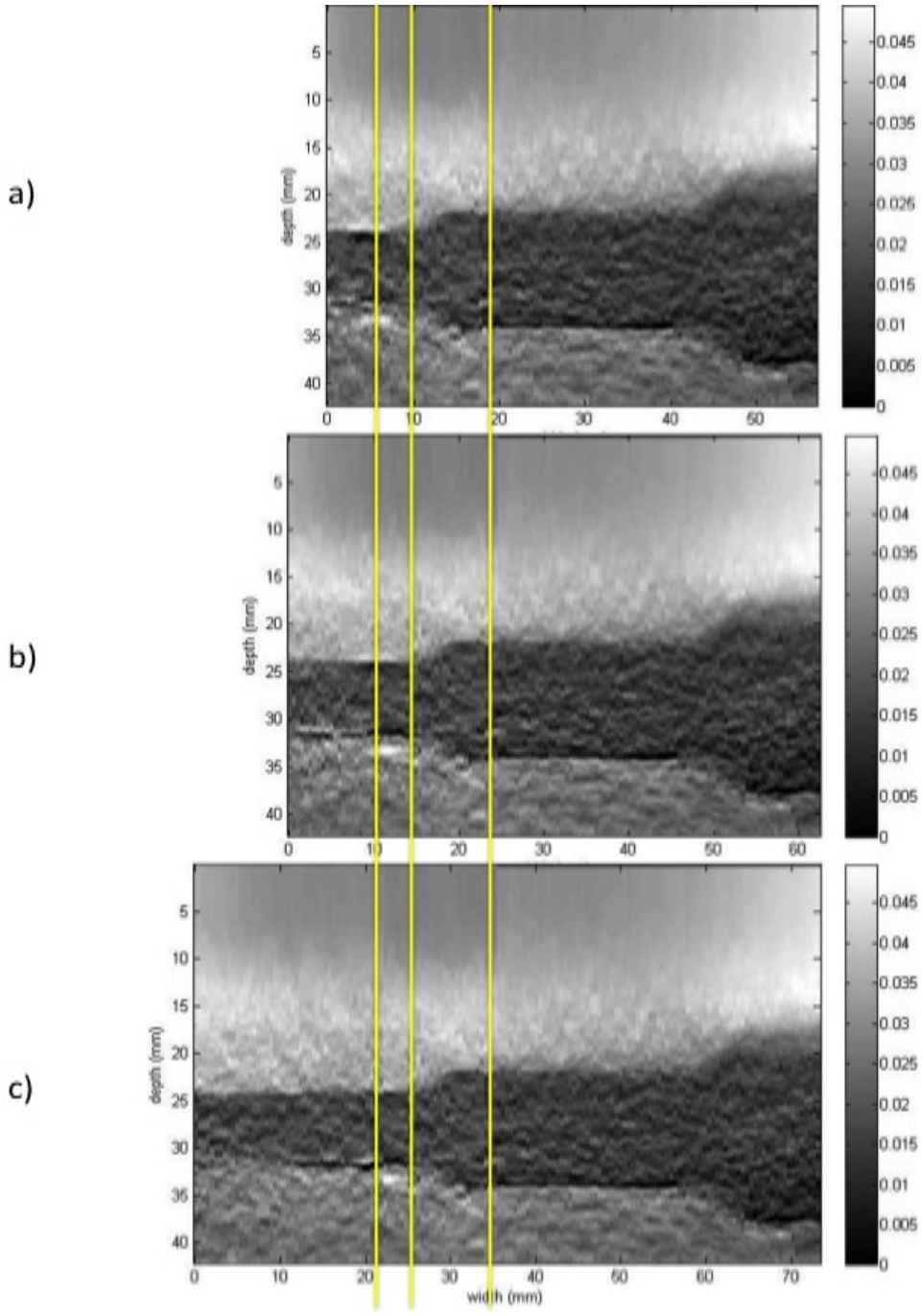

Figure 5.7: Ultrasound elastography mosaics of positions t_0 and t_1 (a), t_0, t_1 and t_2 (b), and t_0, t_1, t_2 and t_3 (c). Stitching lines are shown in yellow.

two displacement maps and at their effect on the final mosaicked elastograms.

5.3.2 Phantom Results

Figure 5.8 shows the results of the validation experiment. The two panoramic displacement maps agree almost exactly; the absolute difference for the entire image had a mean of **0.0755** and a standard deviation of **0.2386** pixels. The maximum difference was 2.0168 pixels and it did not exceed 1 pixel on a mean, per-line basis. For a metric correspondence, 2.0168 pixels, is the equivalent of **0.0406** mm in the axial direction. Once the displacement maps are converted into elastogram mosaics (Fig. 5.8 e,f), the difference becomes indistinguishable even on close inspection. With the clinical application in mind, we conclude that these small differences are acceptable.

5.4 3D Mosaicking Experimental Setup

For 3D validation, RF data was acquired using an Ultrasonix system (Vancouver, BC) at 20MHz sampling rate. The same CIRS (Norfolk, VA) phantom model **049a** was palpated with a 38mm width linear 4D volumetric transducer (4DL14-5/38). Similarly with the 2D experiment, the phantom was placed on a stage to control the compression in the axial direction and the translation in the lateral di-

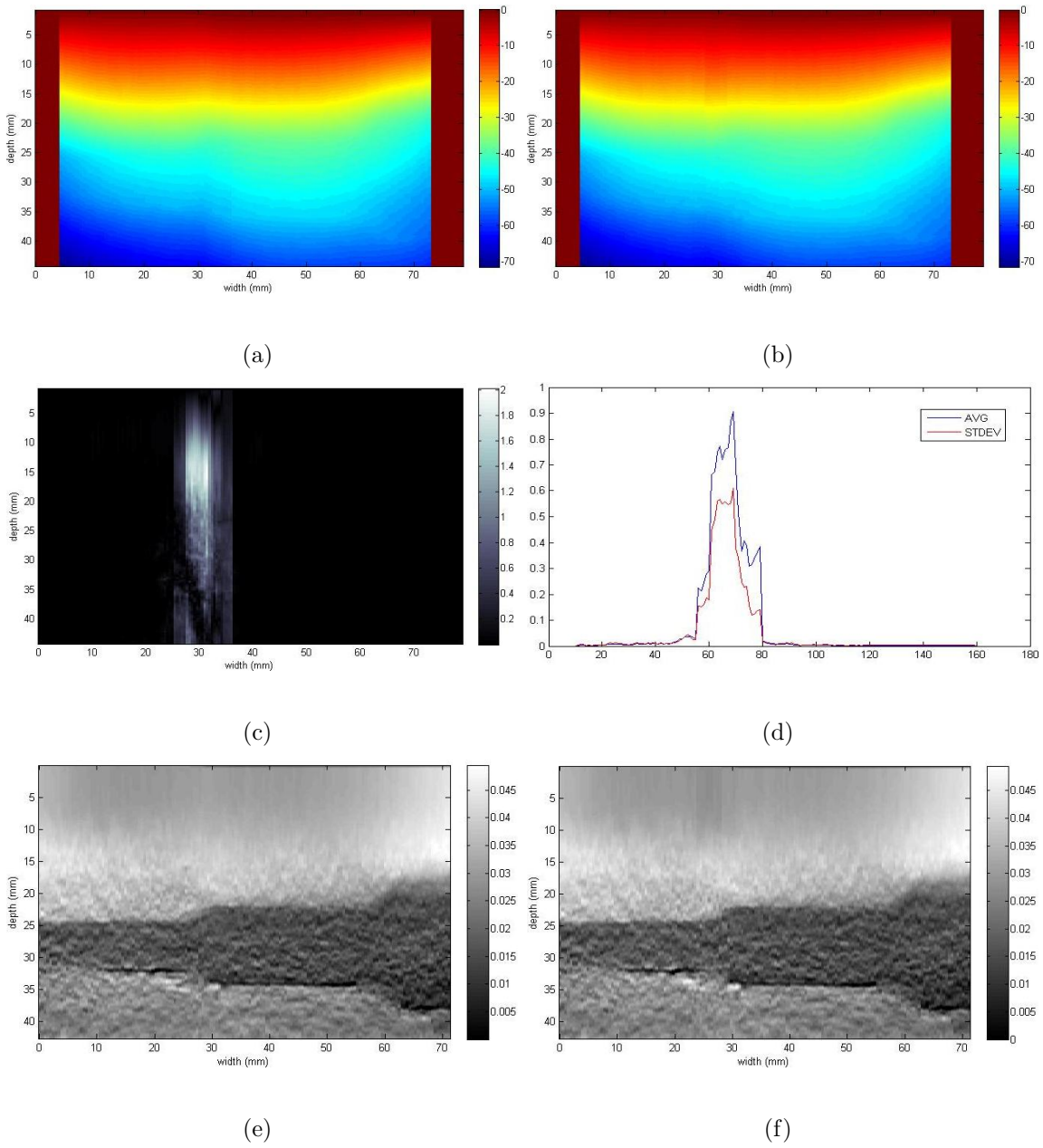

(a) (b)

(c) (d)

(e) (f)

Figure 5.8: Panoramic displacement map of positions t_0 and t_3 (a), and of positions t_0, t_1, t_2 and t_3 (b), the absolute difference between them (c), and the mean and standard deviation of this difference, per line (d). The unit of displacement is pixels. Corresponding ultrasound elastography mosaics of positions t_0 and t_3 (e), and t_0, t_1, t_2 and t_3 (f).

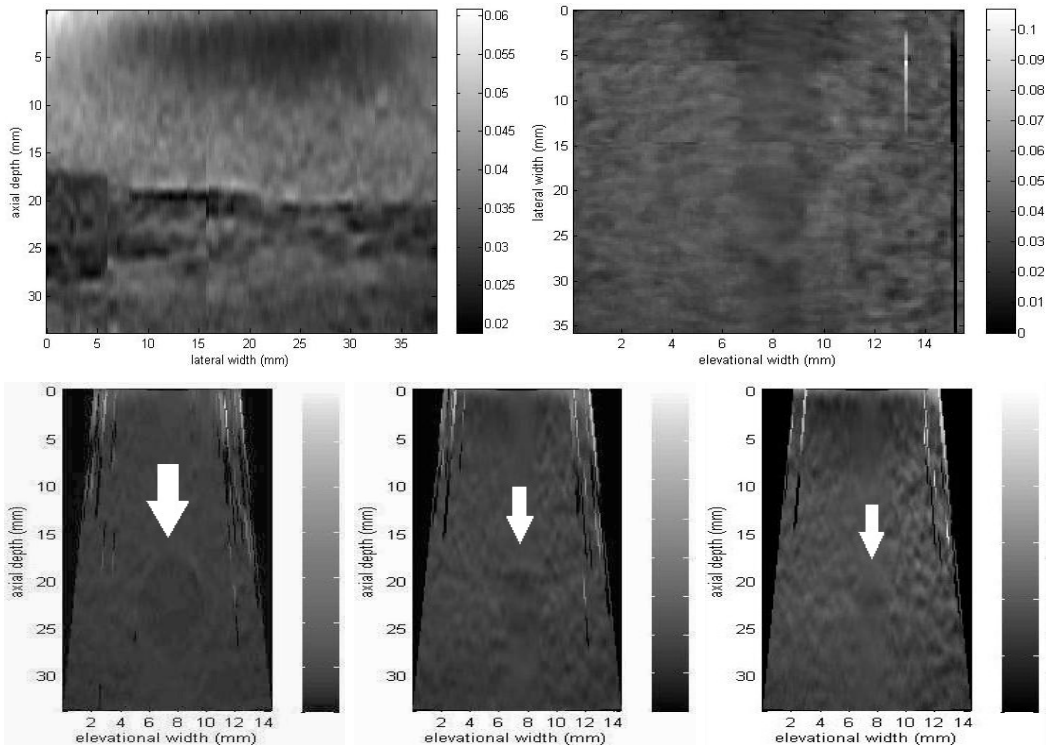

Figure 5.9: 3D ultrasound elastography mosaic: axial-lateral plane (a), lateral-elevational plane (b), and three axial-elevational planes through the three different diameters of the stepped cylinders (c, d, e)

rection (Fig. 5.1). RF data sequences were acquired from four axial compression levels ($c_0 = 0$, $c_1 = 2.54$mm, $c_2 = 5.08$mm, $c_3 =$ back to 0), for each of five lateral translation positions of the transducer ($t_0 = 0$, $t_1 = 5.08$mm, $t_2 = 10.16$mm, $t_3 = 20.32$mm, $t_4 = 22.86$mm), for a total of twenty data sets.

5.4.1 Phantom Results

Figure 5.9 shows the results of the 3D ultrasound elastography mosaic. Strain in the middle frames of the axial-lateral plane (Figure 5.9a), lateral-elevational plane (Figure 5.9b), and 3 axial-elevational planes (Figure 5.9c-e) is shown.

5.5 Conclusion and Future Work

We have presented an algorithm for generating reliable multi-image ultrasound elastography mosaics, robust to regions of decorrelation. For proof of concept, we validated our algorithm on a phantom data set collected under carefully controlled conditions. Further work is needed to expand the elastography mosaicking technique for the unconstrained general case. The challenge of mosaicking while freehand scanning can be met by incorporating frame position information from probe tracking. Efforts are under way to incorporate electromagnetical (EM) tracking in ultrasound transducers. Additional work is needed to address out-of-plane motion in 3D mosaicking. Panoramic B-mode ultrasound has been reported with success in the literature and the addition of corresponding panoramic elastograms improves the potential of ultrasound imaging as a clinical diagnostic and monitoring tool.

Chapter 6

Thermal Imaging

6.1 Background

Thermal ablation therapies aim to destroy specific tissues of interest in the human body using energy sources like RF, laser, microwave, or focused ultrasound. One important area of research is in monitoring the ablative area during treatment. The success of the procedure lies in delivering the appropriate required thermal dose in order to insure complete destruction of the targeted tissue, while at the same time protecting surrounding critical structures.

Among imaging techniques, computerized tomography (CT) and magnetic res-

onance imaging (MRI) have been used to guide the percutaneous placement of RF ablation probes ([99]). MRI is generally considered to currently be the only available method for reliable quantification of temperature changes *in vivo* ([60, 70]). Despite this, MRI is seldom used as it is expensive and requires suitable ablation equipment compatible with high magnetic fields, which also makes it difficult to use intraoperatively, for real-time monitoring.

Ultrasound imaging has been proposed as a guidance and monitoring tool for thermal ablation. Conventional B-mode ultrasound was found to be mostly suitable as a non-invasive visualization tool but not accurate enough for monitoring the changes in tissue temperature throughout the ablation. Other approaches focused on estimating changes in tissue due to increased temperature. Initial efforts focused on the change in speed of sound ([75]), followed by frequency-dependent attenuation ([119]), backscattered power ([112]), and thermal expansion ([103]). A combination of speed of sound and thermal expansion effects was explored several research groups [65, 66, 104, 106, 115], who tracked the heat-induced echo-shift in the raw RF ultrasound data. This technique relies on the fact that both effects of tissue heating translate in real or apparent motion in tissue. While thermal expansion creates physical displacement in the ultrasound images, changes in speed of sound result in an apparent shift, but both effects introduce time-shifts into the received echo signal along the A-line or beam axis direction ([125]). By tracking this shifts in the time-

domain and differentiating the displacement estimates along the axial direction one can obtain the temperature profile.

As discussed in the previous chapters, one of the common challenges for most tracking-based algorithms is signal decorrelation. In the case of thermal ablation procedures, this can be due to drift of probes/equipment used, the motion of the transducer due to patient respiration, cardiac cycle and also to environment factors like electronic noise. Without proper detection and compensation the estimated displacement map may suffer from motion artifacts, and in turn affect the temperature map. An accurate estimation of the displacement map is more crucial in the thermal imaging application where a temperature change of 1^o Celsius causes a very tiny tissue movement of approximately $0.5\mu m$. Solutions for motion compensation in ultrasound thermal strain images have been attempted recently by several groups. Simon et al ([106]) applied the axial derivative to the displacement field in conjunction with 2D low-pass filtering in order to remove the motion artifacts. Bayat *et al.* ([7]) focused on motion compensation during HIFU therapy. They trained an adaptive filter before the start of therapy and used the filter coefficients and interference data for enhancement of the estimated temperature during the HIFU operation . The proposed algorithm managed to effectively suppress the motion artifacts but it was only tested for a brief time period of 4 seconds. The authors also acknowledged their model could be adversely affected by heat diffusion, which means the points chosen for training should

always be outside the effects of heating from the HIFU beam, which for long periods of monitoring might prove difficult. Dutta et al ([28]) looked at heat-induced strain imaging for atherosclerotic plaque evaluation. They used exponential smoothing of their time-series data in an attempt to separate heat-induced strain from mechanical strain due to the pulsatile nature of blood flow.

In this thesis we propose an iterative motion compensation method for heat-induced strain estimation. Tissue displacement is first estimated using the dynamic programming 2D AM technique by Rivaz et al [92], with the additional robust methods presented in Chapter 4. In the remainder of this chapter we present the iterative motion compensation approach which can detect and remove displacement of tissue due to motion and noise in the environment, thus improving the resulting heat-induced strain map. The method was validated in phantom data experiments.

6.2 Methods

For ultrasound images acquired during a thermal ablation procedure, we are proposing a method to detect motion which is not due to the change in temperature of the tissue.

Consider I_K ultrasound RF frames with $K = 0, ..., k$, acquired during the

ablation procedure at times t_0, t_1, ..., t_k. I_0 was acquired at time t_0, when the ablation probe was just turned on. I_k was acquired at time t_k, when the ablation was considered complete and was followed by the ablation probe being turned off. Let n be the number of RF lines for each frame, with each signal sampled at $i = 1,\ 2 \cdots m$.

We estimate the displacement between frame I_0 and each of the other frames I_1 - I_k, using the robust methods presented in Chapter 4. At the end of the displacement estimation process, for the I_0 and I_K pair of RF frames ($K = 1, ..., k$), on the j^{th} pair of RF lines, ${A_i}^K$ and ${L_i}^K$ are the axial and lateral displacements at each sample i (eq. 3.5). We obtain k sets of axial and lateral displacement maps A^K and L^K, from which, after differentiation along the axial direction, we obtain $origS_a$ and $origS_l$ which we will refer to as the *original strain* maps.

We continue with the Iterative Motion Compensation algorithm as follows. For each time t_K ($K = 1, ..., k$):

1. Compute an interpolated image ${I_K}'$ based on I_K and the cumulative axial and lateral displacement estimates up to time t_K.

2. Estimate displacement between ${I_K}'$ and I_{K+1} using same robust methods as in the first iteration. Save $A^{K'}$ and $L^{K'}$. Compute axial and lateral strain maps ${S_a}'$ and ${S_l}'$.

3. Compute a mask using the strain maps $S_a{}'$ and $S_l{}'$. A mask is meant to detect the region which would exhibit the lowest amount of motion due to changes in temperature. Some examples of possible masks are given in the following subsection.

4. Compute a motion vector (a^K, l^K), representative of the axial and lateral displacement observed in the mask region.

5. Compensate for the detected motion and obtain new sets of axial and lateral displacements:

$$newA^K = A^{K'} - a^K; \tag{6.1}$$

$$newL^K = L^{K'} - l^K \tag{6.2}$$

6. After differentiation along the axial direction, we obtain $newS_a$ and $newS_l$ which we will refer to as the *new strain* maps.

The motion vector (a^K, l^K) was chosen as the *median* value of axial and lateral displacements observed in the mask region. Given the variable area of the mask region, combined with the fact that we are observing growing values for the displacements during the ablation process, made us choose the median instead of the mean value. A choice of mean value can also be affected by pixels within the mask with extreme high or low displacements.

Studying the motion detected at each time t_K ($K = 1, ..., k$) can offer insight into its origin. An experiment where the probe is hand-held would be corrupted by physiological hand tremor motion. This kind of motion would not be encountered in experiments where the probe is fixed or supported by a robotic arm. We use the amplitude of the motion vector (a^K, l^K) to detect if at any time cycle of the ablation procedure our data could have been corrupted by high motion in the environment. One such time cycle has the potential to disrupt the rest of the ultrasound data and it could affect the final heat-induced strain estimation. Detecting and removing the data points associated with these events would be beneficial in the clinical setting, especially for lengthy procedures. We define as an *outlier* any cycle at time K ($K = 1, ..., k$) for which displacement $d^K = \sqrt{(a^{K^2} + l^{K^2})}$ is the displacement at time t_K is outside one standard deviation from the mean:

$$d^K \geq \bar{d} + STD_d; \tag{6.3}$$

$$d^K \leq \bar{d} - STD_d, \tag{6.4}$$

where $\bar{d}$ = is the mean value of d^K and STD_d = standard deviation of d^K ($K = 1, ..., k$). We chose the use one standard deviation from the mean as our threshold because we wanted to reduce the effect of disruptive high non-heat induced motion. Setting the threshold higher/lower would Increase the potential to overlook these unwanted data points.

The Iterative Motion Compensation algorithm continues as follows:

1. Remove all data points from *outlier* time cycles.
2. Repeat the same steps as in the first iteration for the remaining data points.
3. Detect *outlier* time cycles for the new motion vectors. Remove data points and repeat. The algorithm stops when no more *outlier* cycles are detected.

6.2.1 Low-Motion Area Masks

Our goal was to identify an area of tissue which should be unaffected by the effects of heating, up to the time the respective ultrasound image was acquired.

A simple and readily available solution was to select everything outside a circle, centered at the ablation probe tip and of a certain diameter, according with previous research findings in the literature. We guided our choice of diameter based on reported literature outcomes of RF ablation in tissue, using along our own experiences as well. A diameter of 20 mm was considered suitable for our experimental data set (Figure 6.1 top row). From here on, we will refer to this solution as the *geometric mask* and will consider it as a benchmark, off-the-shelf solution.

Another approach to low-motion area identification is to use the strain values

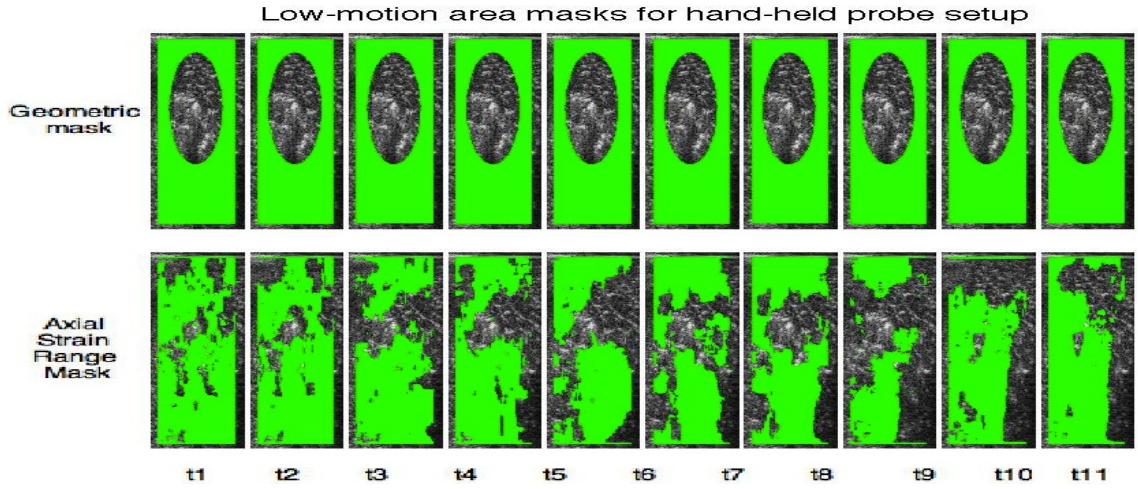

Figure 6.1: Low-motion area masks for the hand-held probe experiment. Top row: geometric mask with 20 mm diameter. Bottom row: Axial strain based mask with $x = 5$ (lowest 5% of strain range).

obtained after displacement estimation. We wanted to select areas of low relative strain but unlike Bayat *et al* ([7]), who used a threshold strain value for their adaptive filter, our mask used a variable threshold as follows:

$$mask_{threshold} = \frac{x * (max(S_a{}') - min(S_a{}'))}{100} \tag{6.5}$$

where $S_a{}'$ is the axial strain obtained at the second iteration using interpolated image data. At each time point in the iteration, the mask selected points for which axial strain was under a certain x percentage of the maximum strain range: This approach was more suitable for our method, as strain range would certainly increase over time, especially in HIFU ablation procedures which can take up to 15-30 minutes, as opposed to the experiment by Bayat *et al* ([7]) which took only 4 seconds. Figure 6.1

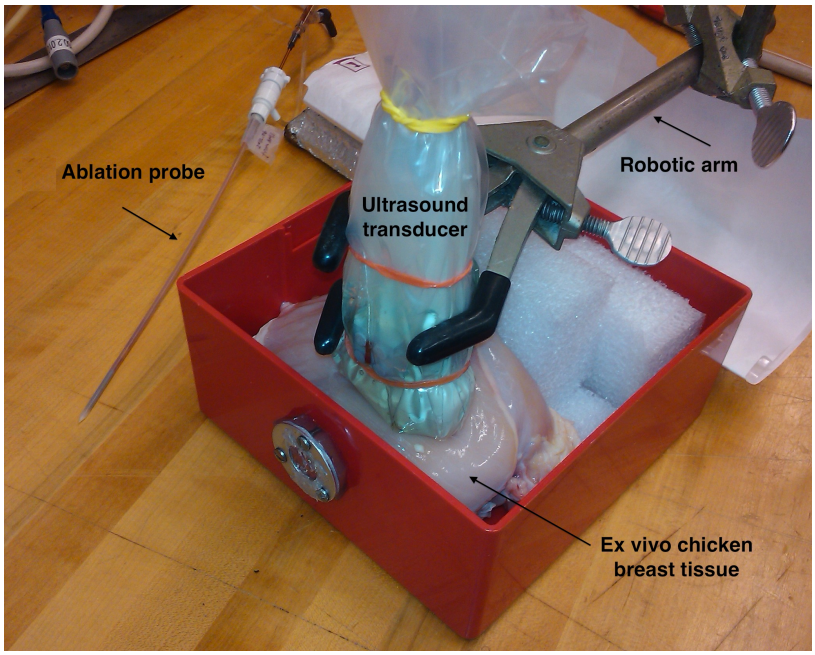

Figure 6.2: Experimental setup for data collection. The *ex vivo* chicken breast tissue was heated using a pulser/receiver HIFU ablation device. Also visible in the image are the ultrasound probe and the passive arm used to support the transducer in one part of the experiment.

bottom row shows the evolution of an axial strain based mask for $x = 5$, where we select areas with axial strain within the lowest 5% of the strain range.

6.3 Experimental Setup

To evaluate our method, we conducted HIFU ablation experiments on *ex vivo* chicken breast tissue. Figure 6.2 shows the components of our experimental setup. The HIFU pulse/receiver unit was accompanied by a passive pump with fluid circulation for cooling the HIFU applicators. A robotic arm was used to support the

ultrasound transducer in one part of the experiment. The tissue was interrogated using the SonixCEP ultrasound system (Ultrasonix Medical Corp., Richmond, BC, Canada) with $4DL14-5/38$ transducer at the center frequency of 6.7 MHz. During the data collection, the temperature of the tissue was monitored and logged using a temperature reading probe inserted into the tissue. The distance between the temperature reading probe and the ablator probe tip was between $7.00-10.31$ mm. The temperature was read every 1 second and the readings were saved to a file for later evaluation. For raw RF ultrasound data capture we used the MUSIIC RF server (Figure 6.3) [111, 52]. A conventional B-mode image is at the center of the screen capture, with the ablation probe visible at the center, and also a temperature reading probe 8.37 mm away from it (Figure 6.3).

Three data sets were collected using this setup. In the first two experiments, the ultrasound transducer was held by the operator's hand. The operator attempted to keep their arm very still throughout the entire data collection time. This was a difficult task to accomplish, as both ablations lasted almost 20 minutes. In the third experiment, the ultrasound probe was supported by a passive robot arm (Figure 6.2).

The ablation process consisted of cycles of 100 seconds each, followed by a pause of 2 seconds, during which the raw ultrasound data was collected. The pause insured no ablator interference with the ultrasound RF signal. The entire experiment lasted 10 cycles for the hand-held probe experiments and 11 cycles for the robot-held

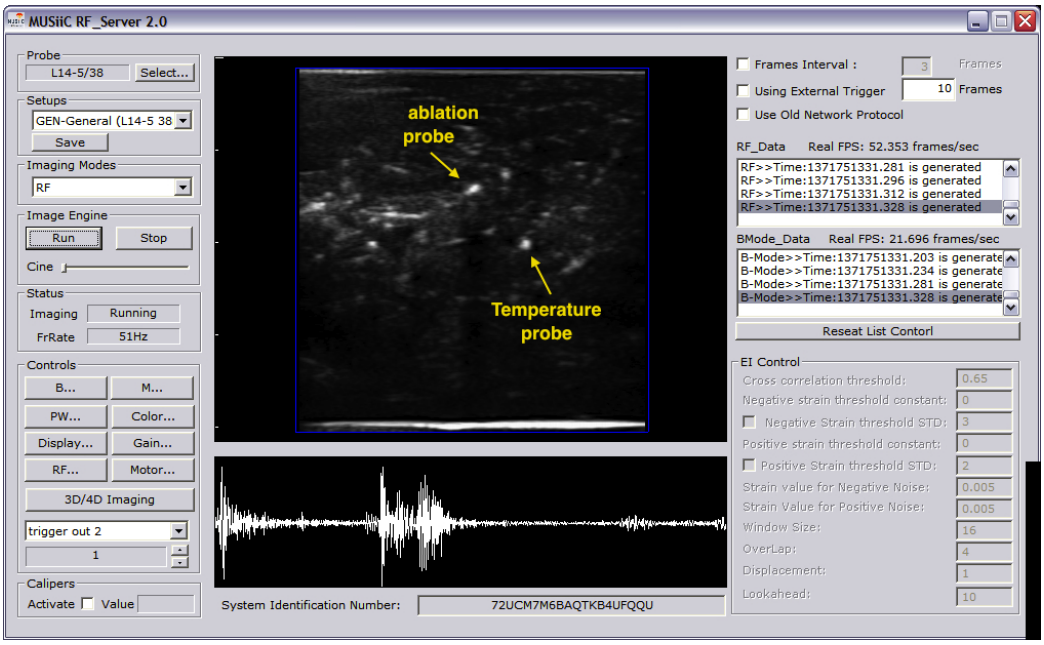

Figure 6.3: Screen capture of the MUSIIC RF server data acquisition system. Visible on conventional B-mode ultrasound image of the tissue are the ablator probe tip and also the tip of the temperature reading probe.

experiment. This amounted to 17 minutes for the hand-held probe experiments and 19 minutes for the robot-supported one. The temperature readings started a couple of seconds before the first cycle. The maximum temperature recorded was 49.7^oC and 51.8^oC for the hand-held probe experiment, and 47.5^oC for the robot-held one.

The goal of our experiment was to evaluate the efficacy of the iterative motion compensation algorithm in detecting non-heat induced motion in the ablated tissue. We hypothesized the detected motion would have a higher amplitude in the hand-held probe setup than in the robot-held one. We also wanted to assess the improvement in the estimated heat-induced echo strain and its correlation with the pathology results. We hypothesized the iterative motion compensation algorithm would improve

on the strain SNR and CNR of the ablated lesions. Our final goal was to assess the accumulation of strain with the increase in temperature in regions of interest around the ablation probe.

6.4 Experimental Results

Gross pathology results from the ablation experiments are presented in Figure 6.4. Cross-sections of the ablated regions are visible, along with a ruler for dimension estimation. Also visible in every image is the small hole created by the ablation probe which is generally positioned at the center of the ablated area. Lesions were 1-2 cm in diameter. For the hand-held probe experiments, the lesions were round and equally distributed radially from the ablation probe position in the center. In the robot-held probe experiment however, the ablated area took the shape of a kidney bean, with more affected tissue positioned on top and to the left of the ablation probe (Figure 6.4 c).

6.4.1 Motion Detection

The first test for the efficacy of our method was in the quality of the detected non-heat-induced motion in our experimental data. Our hypothesis was that the

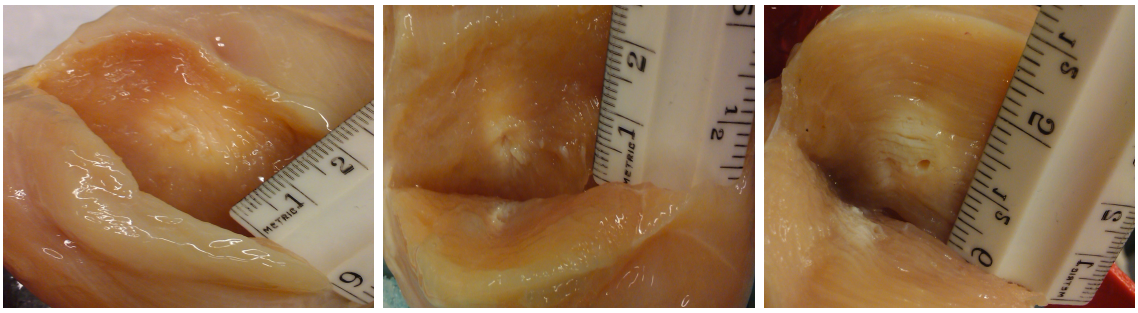

(a) (b) (c)

Figure 6.4: Gross pathology of *ex vivo* tissue. Cross-sections of the ablated regions with ruler visible. Also visible is the position of the ablation probe, at the center of the ablated tissue. First hand-held probe experiment (a), second hand-held probe experiment (b) and robot-held probe experiment (c).

amplitude of the detected motion in the robot-held probe data set will be lower than in the hand-held probe experiments. Figure 6.5 shows the amplitude of the detected motion in the three experimental setups. Each sub-plot shows the motion vectors (axial and lateral motion in millimeters) for each time step of the experiment. Each experiment is shown in one column, with the subplot in each row representing the motion vectors as detected through the use of four different masks in the IMC algorithm. The top row used the geometric mask with a 20 mm diameter, while the other three rows used axial-strain based masks, with thresholds given by $x = 5$, 10 and 15 % of the strain range (eq. 6.5).

The motion values are also given in Table 6.1. The amplitude of the detected motion in the robot-held probe data set is one order of magnitude lower than in the hand-held probe experiments. The unpaired t-test results showed a two-tailed

Table 6.1: Amplitude of detected non-heat-induced motion in hand-held and robot-held probe experiments (in mm)

	Hand-held Expr. 1		Hand-held Expr. 2		Robot-held Expr.	
	mean	stdev	mean	stdev	mean	stdev
Geometric Mask	0.133	0.114	0.291	0.169	0.017	0.009
Axial-strain based mask A	0.127	0.101	0.286	0.419	0.016	0.008
Axial-strain based mask B	0.116	0.091	0.378	0.614	0.019	0.012
Axial-strain based mask C	0.105	0.075	0.248	0.364	0.019	0.012

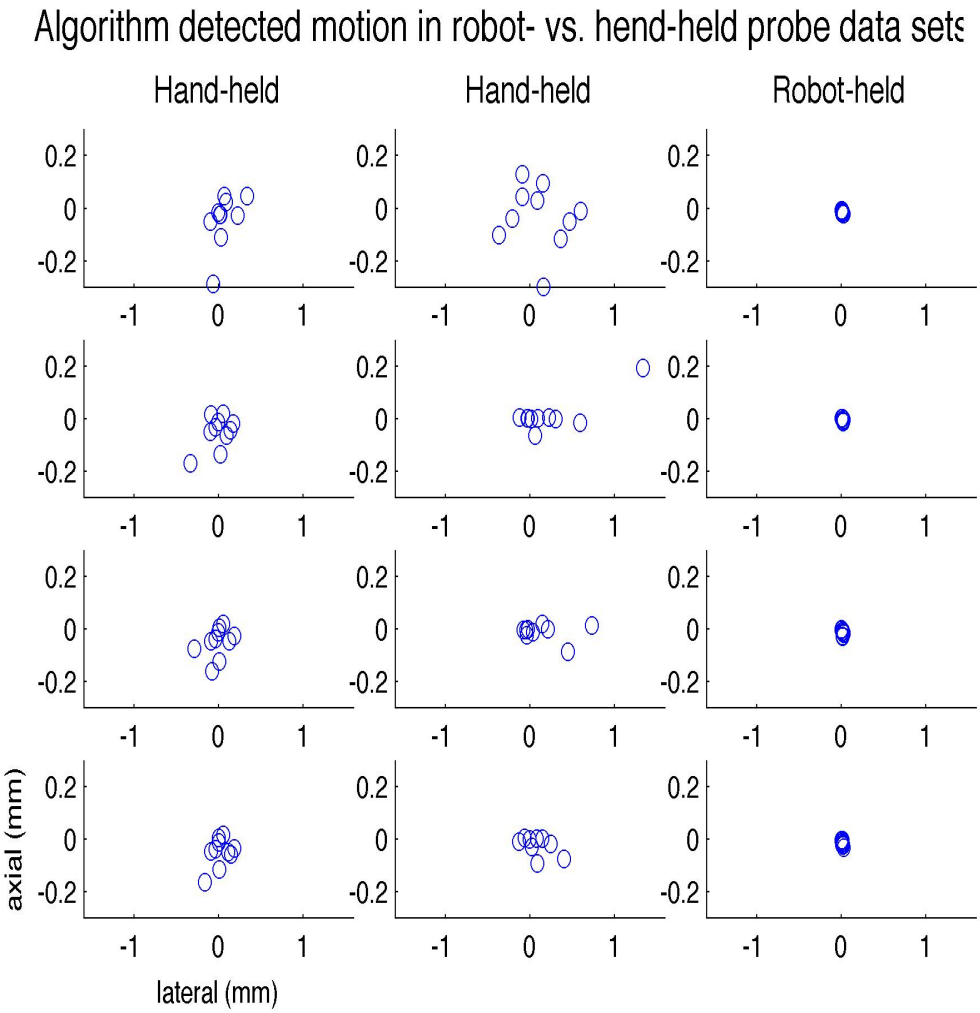

Figure 6.5: Algorithm detected motion in robot- (right most column) versus hand-held probe (left columns) data sets. Each row corresponds to a different mask used during IMC, from top to bottom: geometric mask (20 mm diameter), axial strain based masks with thresholds given by $x = 5$, 10 and 15 % of the strain range

Table 6.2: Amplitude of detected non-heat-induced motion in hand-held vs. robot-held probe experiments: t-test results. Mean, standard deviation (StDev) and standard error of mean (SEM) are presented for each group.

Group	Hand-held	Robot-held		Group	Hand-held 1	Hand-held 2
Mean	0.2105	0.0174		Mean	0.1203	0.3006
StDev	0.3075	0.0099		StDev	0.0932	0.4076
SEM	0.03438	0.0015		SEM	0.01474	0.0645
p-value <0.0001				**p-value <0.0079**		

$p - value$ of less than 0.0001, which is considered by conventional criteria to be an extremely statistically significant difference (see also Table 6.2).

The amplitude of physiological human hand tremor in an operating room setting has been shown to be around $100\mu m$ ([107]). Our observed motion amplitude in the hand-held probe setting was on average $210\mu m$, which suggests our operator was probably not as skilled as the retinal surgeons in [107], and also that we probably encountered motion interference from other sources as well. The observed motion amplitude in the robot-held probe setup was on average $17.4\mu m$.

When relying on a stable hand from the operator for 15-20 minutes, one has to consider the possibility of fatigue. An unpaired t-test between the first and second experiments with the probe hand-held revealed a statistically significant difference between the amplitude of the detected motion in the two groups, with a two tailed $p - value$ of less than 0.0079 (see also Table 6.2). This can be explained in part by growing operator fatigue. We also expected to find more *outliers* (eq. 6.4) in the detected motion from cycles in the second half of the ablation procedures.

1. In the first hand-held probe experiment, we found 2 to 4 outlier cycles, depending on the mask used. The outliers were spread throughout the procedure.

2. The second hand-held probe experimental data was acquired right after the first one. Our expectation was that it would be more influenced by operator fatigue. The average amplitude of the motion vectors was more than two times higher than for the first hand-held probe experiment (Table 6.1). The standard deviation was also much higher, showing a bigger range for the motions detected at each cycle. For the geometric mask, we found 4 outlier cycles. For the axial-strain based masks, we only found 1 outlier cycle, but the amplitude of the motion vector was higher than $(mean + 2 * stdev)$. All cycles which exhibited outlier behavior were positioned in the last half of their procedure, supporting our hypothesis of operator fatigue.

3. In the robot-held probe experiment, we found between 3 and 5 outlier cycles. The interesting thing to notice is that were found among the first two and and last three cycles in the robot-held probe experiment. The middle 6 cycles were outlier-free regardless of the mask used. In the robot-held probe data set, no cycle exhibited motion amplitudes higher/lower than $(mean \pm 2 * stdev)$.

6.4.2 Improving Heat-Induced Strain Maps

Our study's goal was to improve the heat-induced strain map such that it would correlate positively to the gross pathology results. Figures 6.6, 6.8 and 6.10 show the original strain maps (top row) and the resulting strain after only one iteration of the IMC method. In every figure, strain maps are presented at each cycle of the ablation experiment. The geometric mask with a diameter of 20 mm was used on the second row, while the last three rows show the result of using axial-strain based masks with different values for x.

The original strain maps fail to capture the ablation lesion in all three experiments. The robot-held probe experiment benefits the most from the motion compensation approach. The ablation lesion is clearly visible in the new strain maps (Figure 6.10). Further more, the lesion's shape, approximate dimensions and position clearly correlate positively with the pathology results (Figure 6.4 (c)). Our algorithm compensated for non-heat induced motion present in the environment which, at just tens of μm, was enough to compromise the original strain estimation.

For the hand-held probe data sets, improvement can be seen at some points during the ablation process, but the result is not as clearly visible as in the robot-held probe data set (Figures 6.6, 6.8).

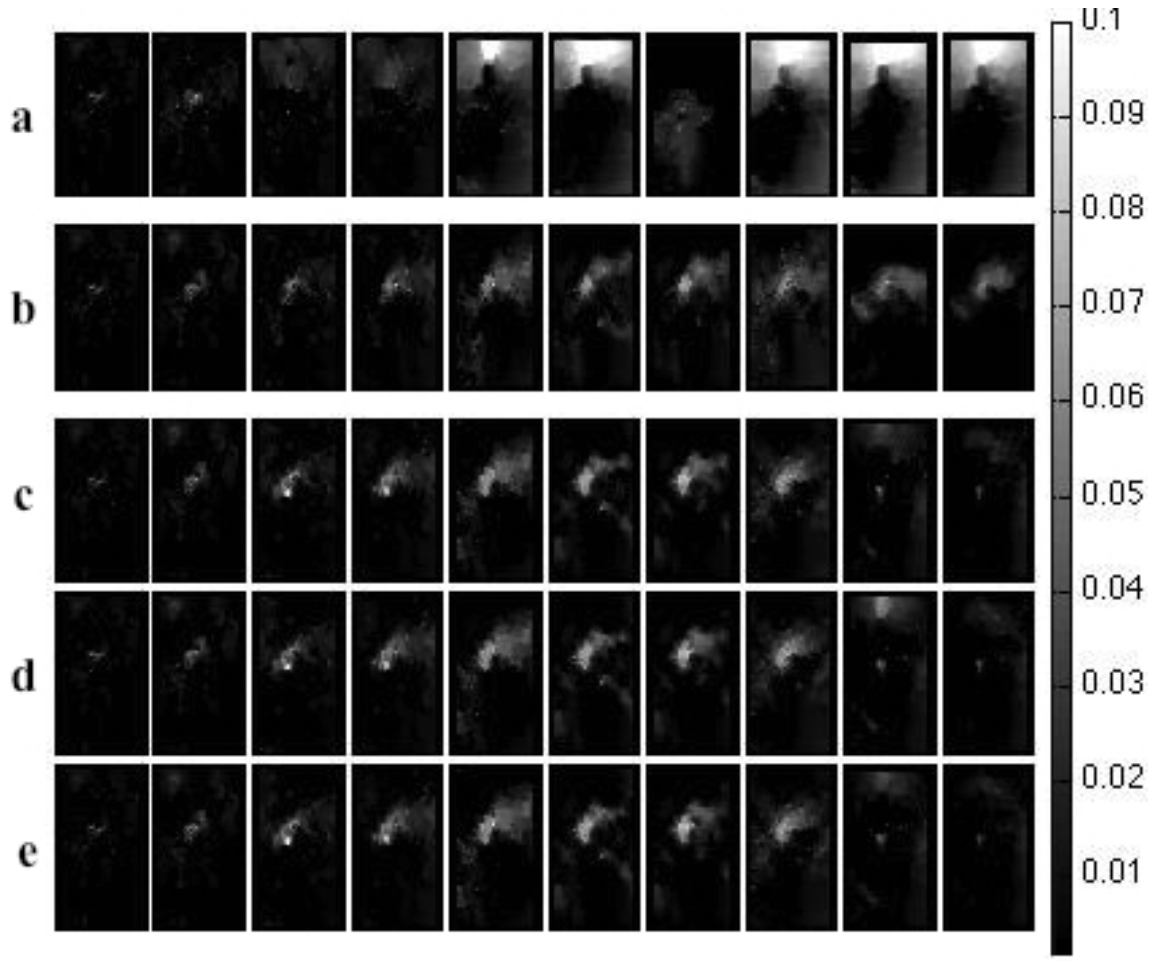

Figure 6.6: Axial strain in the first hand-held probe experiment. Original strain at the ten data collection points (a). Strain after IMC, from top to bottom: geometric mask (b), axial strain based masks with thresholds given by $x = 5$, 10 and 15 % of the strain range (c-e).

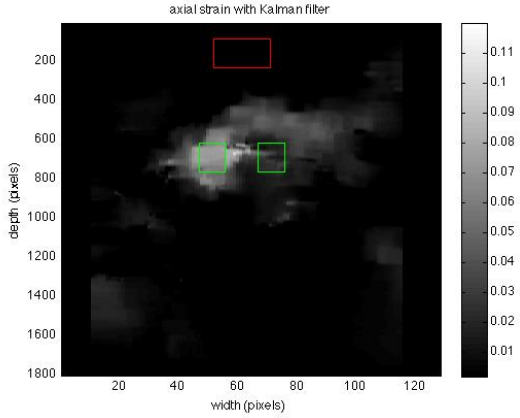

(a)

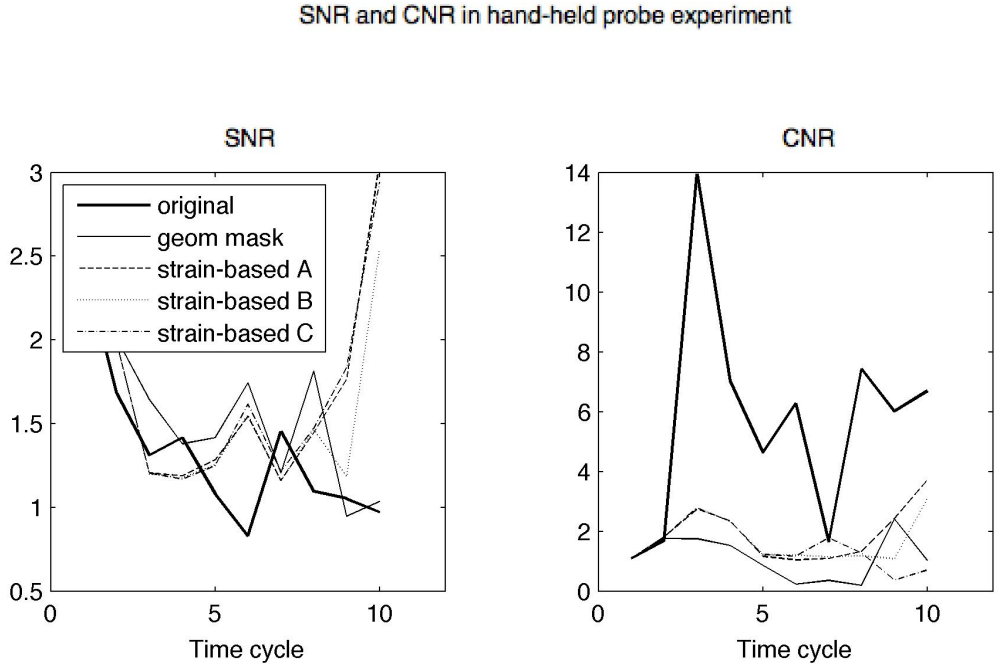

(b)

Figure 6.7: SNR and CNR of axial strain in the first hand-held probe experiment. Background and target windows a shown in (a).

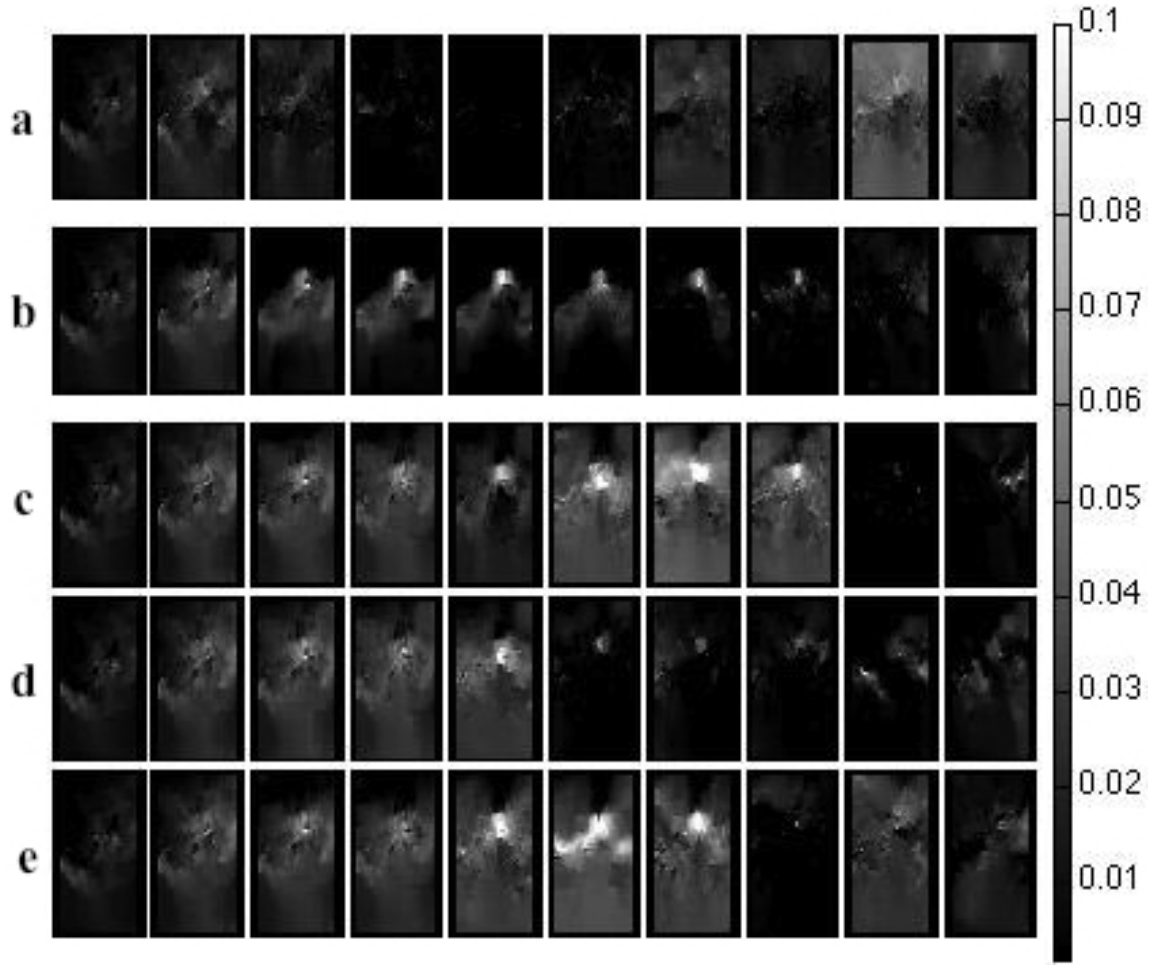

Figure 6.8: Axial strain in the second hand-held probe experiment. Original strain at the ten data collection points (a). Strain after IMC, from top to bottom: geometric mask (b), axial strain based masks with thresholds given by $x = 5$, 10 and 15 % of the strain range (c-e).

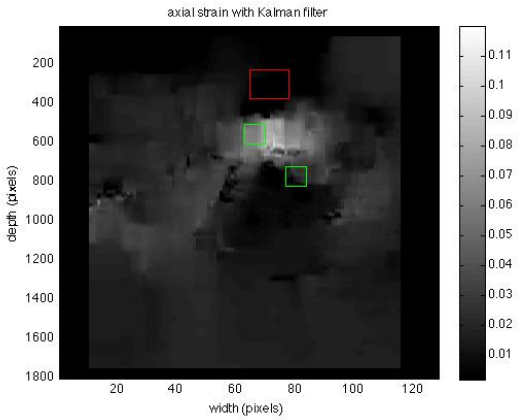

(a)

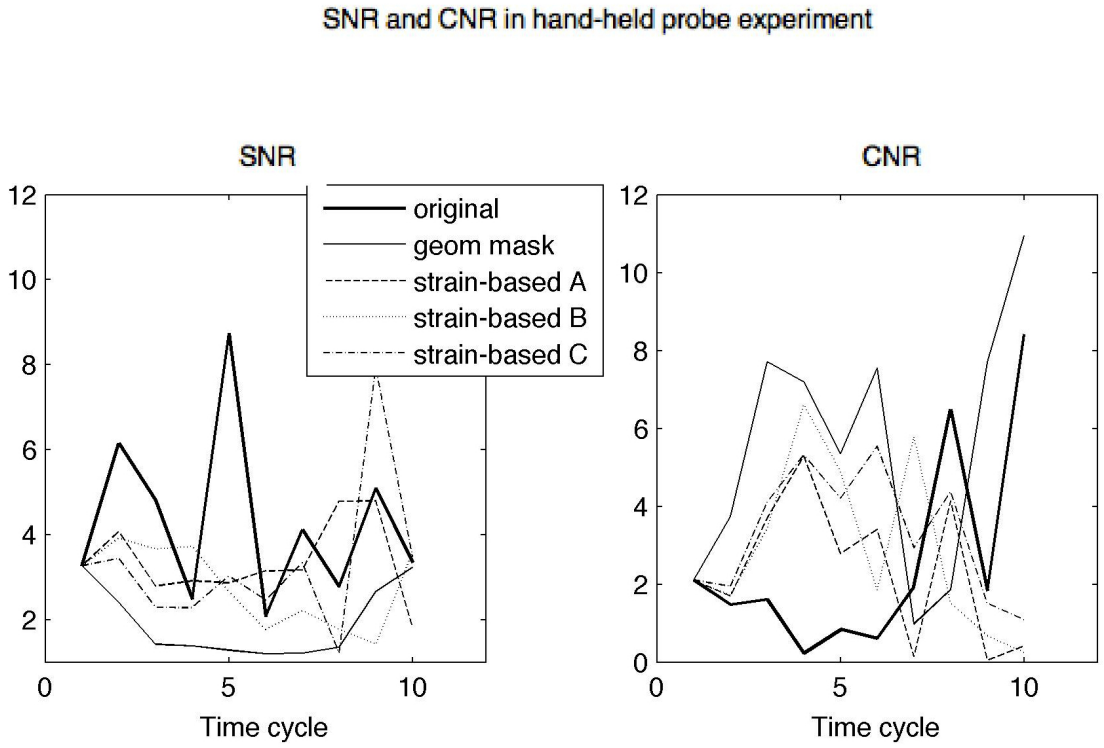

(b)

Figure 6.9: SNR and CNR of axial strain in the second hand-held probe experiment. Background and target windows a shown in (a).

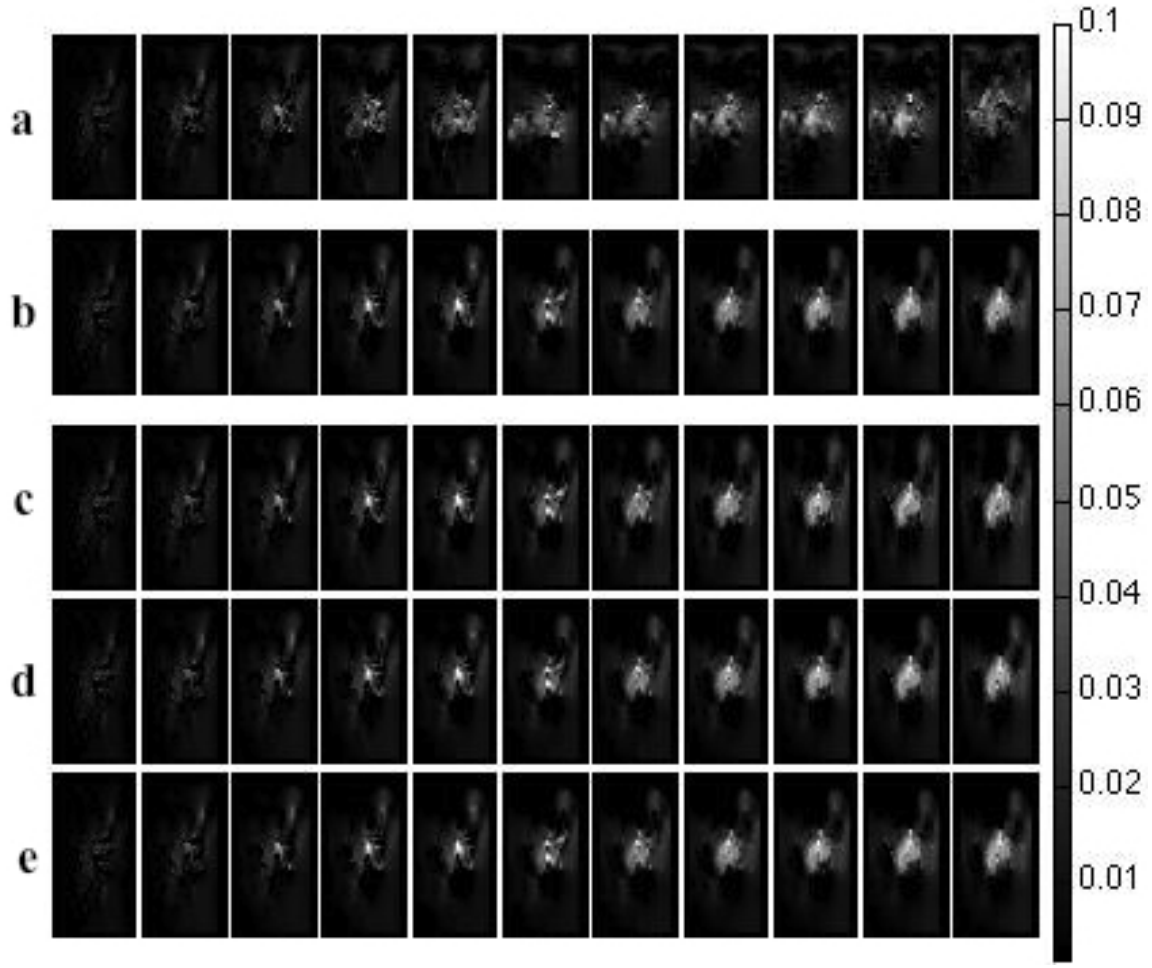

Figure 6.10: Axial strain in the robot-held probe experiment. Original strain at the ten data collection points (a). Strain after IMC, from top to bottom: geometric mask (b), axial strain based masks with thresholds given by $x = 5$, 10 and 15 % of the strain range (c-e).

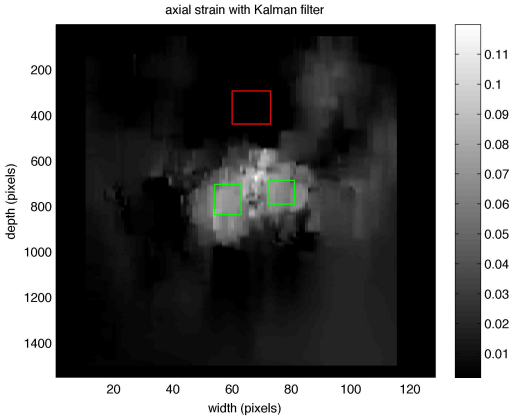

(a)

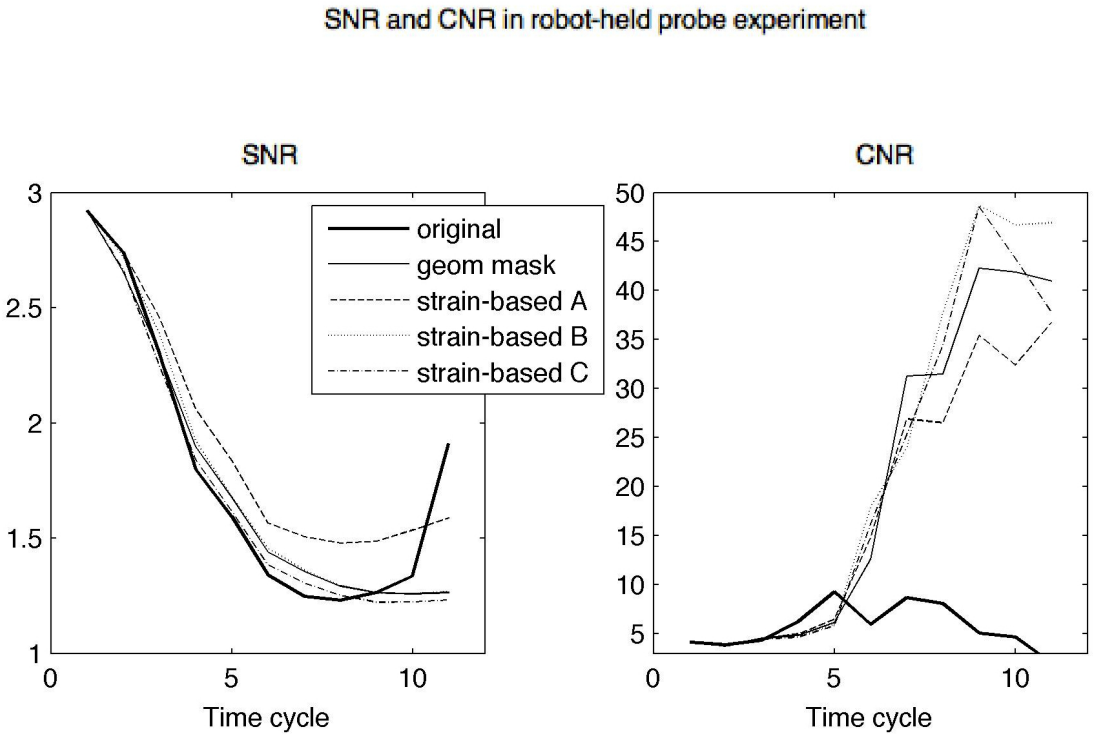

(b)

Figure 6.11: SNR and CNR of axial strain in the robot-held probe experiment. Background and target windows a shown in (a).

The unitless metrics signal to noise ratio (SNR) and contrast to noise ratio (CNR) are frequently used as quality indicators for strain images:

$$SNR = \frac{\bar{s}}{\sigma}, \tag{6.6}$$

$$CNR = \frac{C}{N} = \sqrt{\frac{2 * (\bar{s}_b - \bar{s}_t)^2}{(\sigma_b)^2 + (\sigma_t)^2}} \tag{6.7}$$

where $\bar{s}_b$ and $\bar{s}_t$ are the spatial strain average of the target and background windows, $(\sigma_b)^2$ and $(\sigma_t)^2$ are the spatial strain variance of the background and target, and $\bar{s}$ and σ are the spatial average and variance of a window in the strain image respectively.. Figures 6.7, 6.9 and 6.11 show at the top the axial strain images along with the target and background windows used for CNR calculation. The SNR was calculated for the entire image. The values are presented in Table 6.3.

The improvement in SNR as calculated (for the entire strain image) is inconclusive for this data set. In the robot-held experiment, average SNR over the eleven data points stays approximately constant ($96 - 99\%$). The improvement in CNR however, is clear for every data point in the robot-held probe experiment with $215 - 292\%$ average (Table 6.3). For the hand-held probe experiments, some SNR and CNR improvement is noticed, but not all data points are following the trend (Figures 6.9 and 6.11, Table 6.3).

Table 6.3: Axial strain SNR and CNR in hand-held and robot-held probe experiments

	Hand-held E1		Hand-held E2		Robot-held Expr.	
	SNR	CNR	SNR	CNR	SNR	CNR
Original	1.335	5.645	4.287	2.553	1.789	5.672
Geometric Mask	1.566	1.122	1.939	5.515	1.757	20.368
Axial strain-based mask A	1.709	1.878	3.365	2.375	1.926	17.869
Axial strain-based mask B	1.599	1.695	2.801	2.884	1.776	22.269
Axial strain-based mask C	1.715	1.458	3.277	3.315	1.719	20.772

To get a clearer picture of the efficacy of the IMC algorithm we needed quantitative measures of the improvement in strain estimation. For each data set, we selected two regions of interest, ROI1 and ROI2, positioned equidistantly between the ablator probe and temperature reading probe. The ROIs dimensions were approximately 2 mm x 2 mm. Figures 6.12, 6.13 and 6.14 show at the top the position of the two ROIs (red and blue) superimposed over B-mode images of the tissue for every experimental setup. Our goal was to look at the evolution of axial strain vs. temperature in these two regions of interest. Temperature data was available only at the tip of the temperature reading probe, so no ground truth temperature data was available for the selected ROIs. Our two hypothesis were:

1. The axial strain values in the two regions would follow the temperature trend, with the strain increasing as more heat was deposited into the tissue.

2. The axial strain values in the ROI1, positioned closer to the ablator, would be higher than the values in ROI2.

For the robot-held probe data set, all our hypothesis were confirmed: 1) as the temperature of the tissue increased, the axial strain values in the selected ROIs also increased. 2) the values of axial strain in the ROI1 (closer to the ablator probe and thus, warmer) were consistently higher than those in ROI2. Small values for standard deviation resulted in very tight confidence regions for all the masks used. Figure 6.14 shows the temperature readings from the robot-held probe experiment in the top subplot, followed by subplots presenting axial strain measurements in ROI1 (left column) and ROI2 (right column). Each row corresponds to a different mask used during the IMC algorithm, from top to bottom: geometric mask (20 mm diameter), axial strain based masks with thresholds given by $x = 5$, 10 and 15 % of the strain range We chose to present the mean axial strain in the respective ROI for every time step, and also the confidence region ($mean \pm 1 * stdev$) as a shaded area.

For the hand-held probe experiments, our algorithm estimated higher strain for the warmer ROI closer to the heat source. The axial strain values however, did not always follow the temperature rise for the entire length of the procedure. For both experiments, the detected motion field influenced the estimated axial strain. Cycles where the motion vector was deemed an *outlier* translated into axial strain values which were either very high or very low when compared with the previous time step. We noticed discrepancies between the axial strain values estimated using different masks, as the outlier cycle(s) differed with the mask used. Confidence regions were

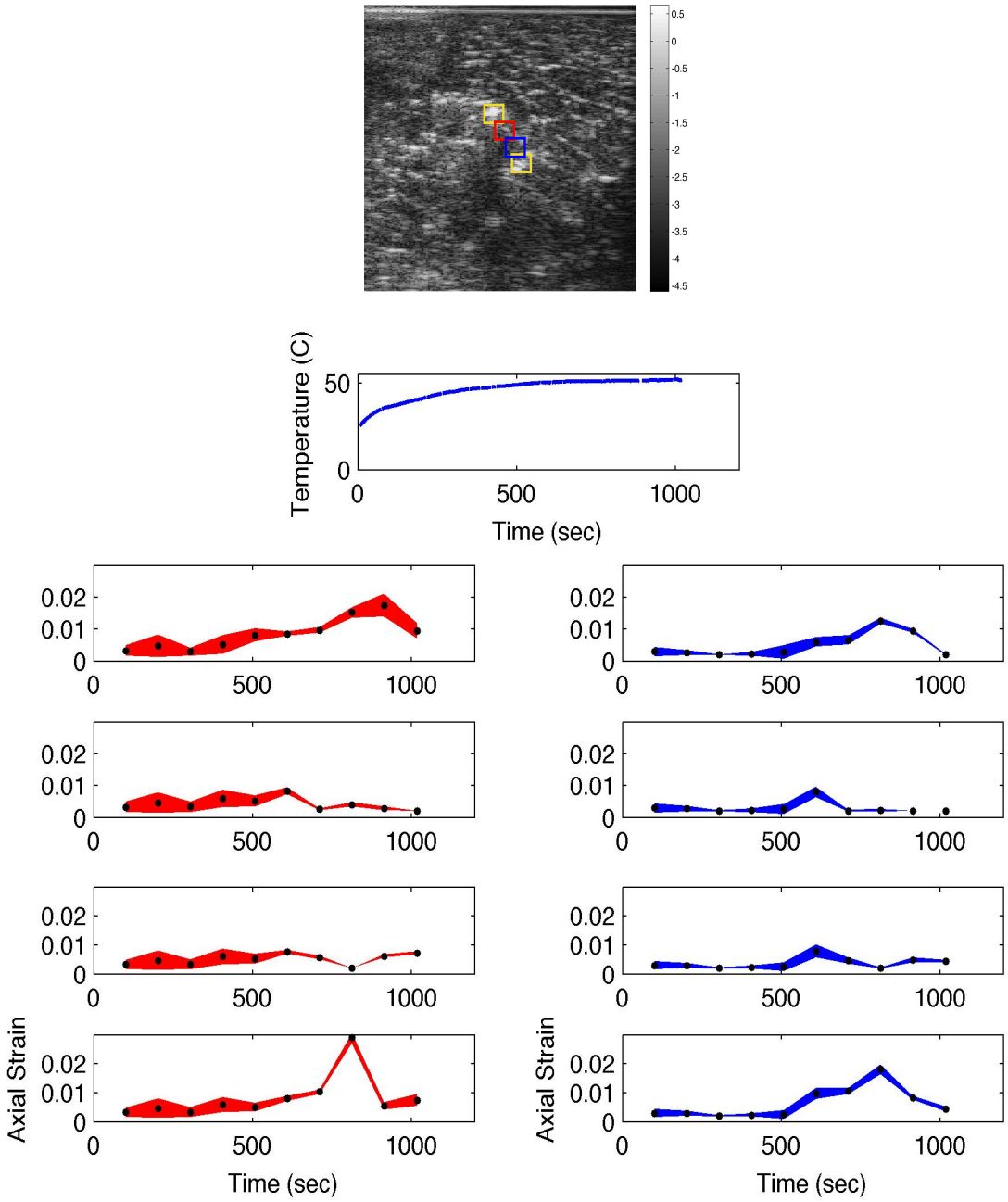

Figure 6.12: Two regions of interest (ROI1 red and ROI2 blue) were selected at equal distances to the ablator probe, to the temperature reading probe (both yellow) and to each other. (b) Temperature readings from the first hand-held probe experiment (top subplot), followed by subplots presenting axial strain measurements in ROI1 (left column) and ROI2 (right column). From top to bottom: geometric mask (20 mm diameter), axial strain based masks with thresholds given by $x = 5$, 10 and 15 % of the strain range Mean axial strain values were calculated for every time step (black dots); the confidence region ($mean \pm 1 * stdev$) is shown as a shaded area.

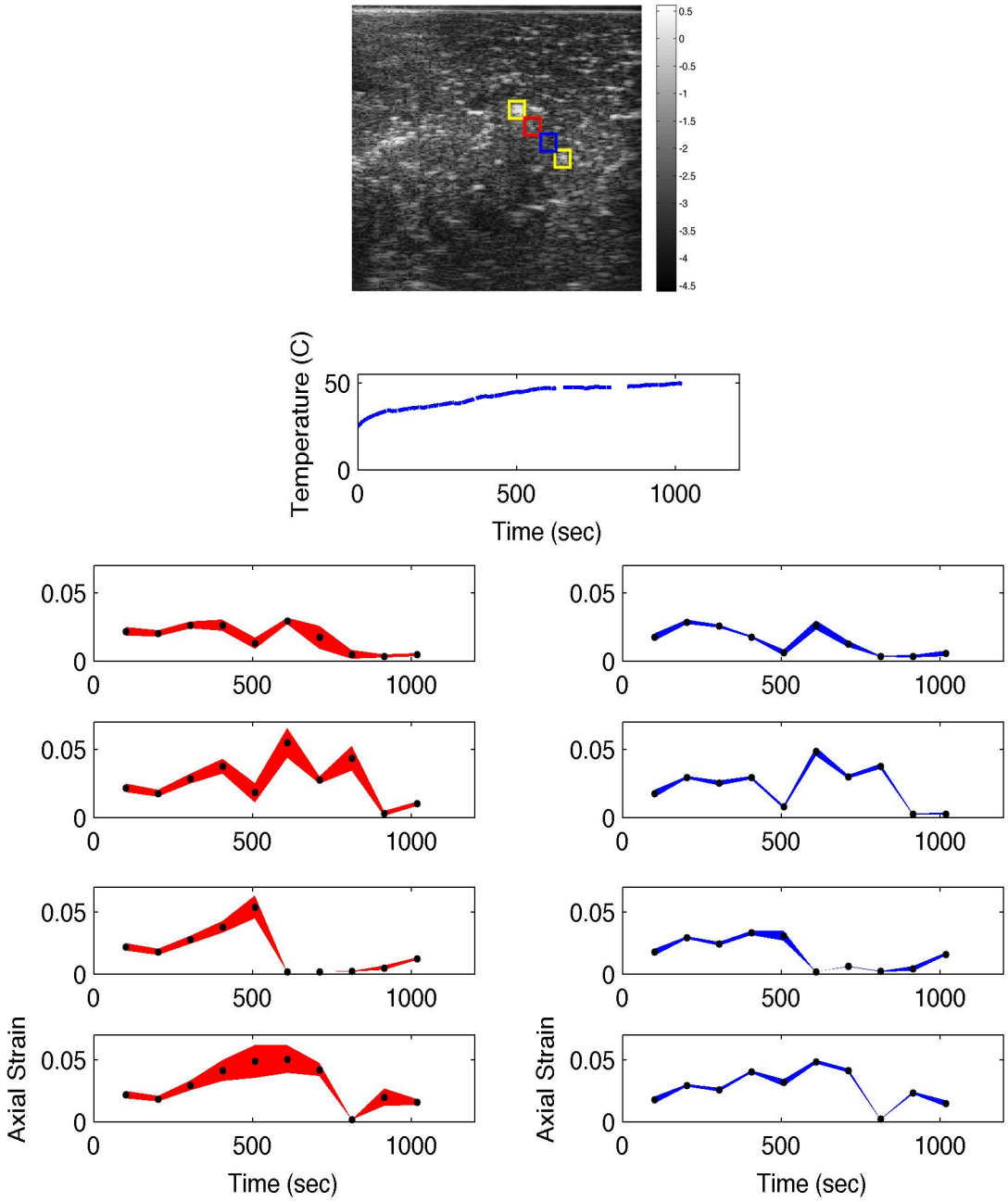

Figure 6.13: Two regions of interest (ROI1 red and ROI2 blue) were selected at equal distances to the ablator probe, to the temperature reading probe (both yellow) and to each other. (b) Temperature readings from the second hand-held probe experiment (top subplot), followed by subplots presenting axial strain measurements in ROI1 (left column) and ROI2 (right column). From top to bottom: geometric mask (20 mm diameter), axial strain based masks with thresholds given by $x = 5$, 10 and 15 % of the strain range Mean axial strain values were calculated for every time step (black dots); the confidence region ($mean \pm 1 * stdev$) is shown as a shaded area.

also variable between masks, but also from one time step to another and between the two ROIs (Figures 6.12 and 6.13).

The hand-held probe data sets were great candidates to test the efficacy of the second part of our IMC algorithm. Both experiments had time cycles with high motion, which our algorithm could detect and remove. Figure 6.15 shows the original strain maps (top row), the strain after the first iteration of motion compensation (middle row) and after the second iteration where data corresponding to outlier time cycles had been removed (bottom row).Improvement in the heat-induced strain estimation makes the ablation lesion clearly visible at the end of the procedure. The accumulation of axial strain in the two ROIs shows improved correlation with the temperature curve (Figure 6.16).

We identified two potential situations when the second (and subsequent) iterations of the IMC algorithm might fail to improve the final strain estimate:

1. The corrupted cycles are at the very end of the procedure. Removing them from the data set cannot improve the previous cycles and it would also leave us without a final heat-induced strain estimation.

   Figure 6.17 is representative of this situation. Although the strain estimation clearly improved due to the removal of the first 3 outlier cycles, we are still missing a final evaluation of the position and dimensions of the ablated area.

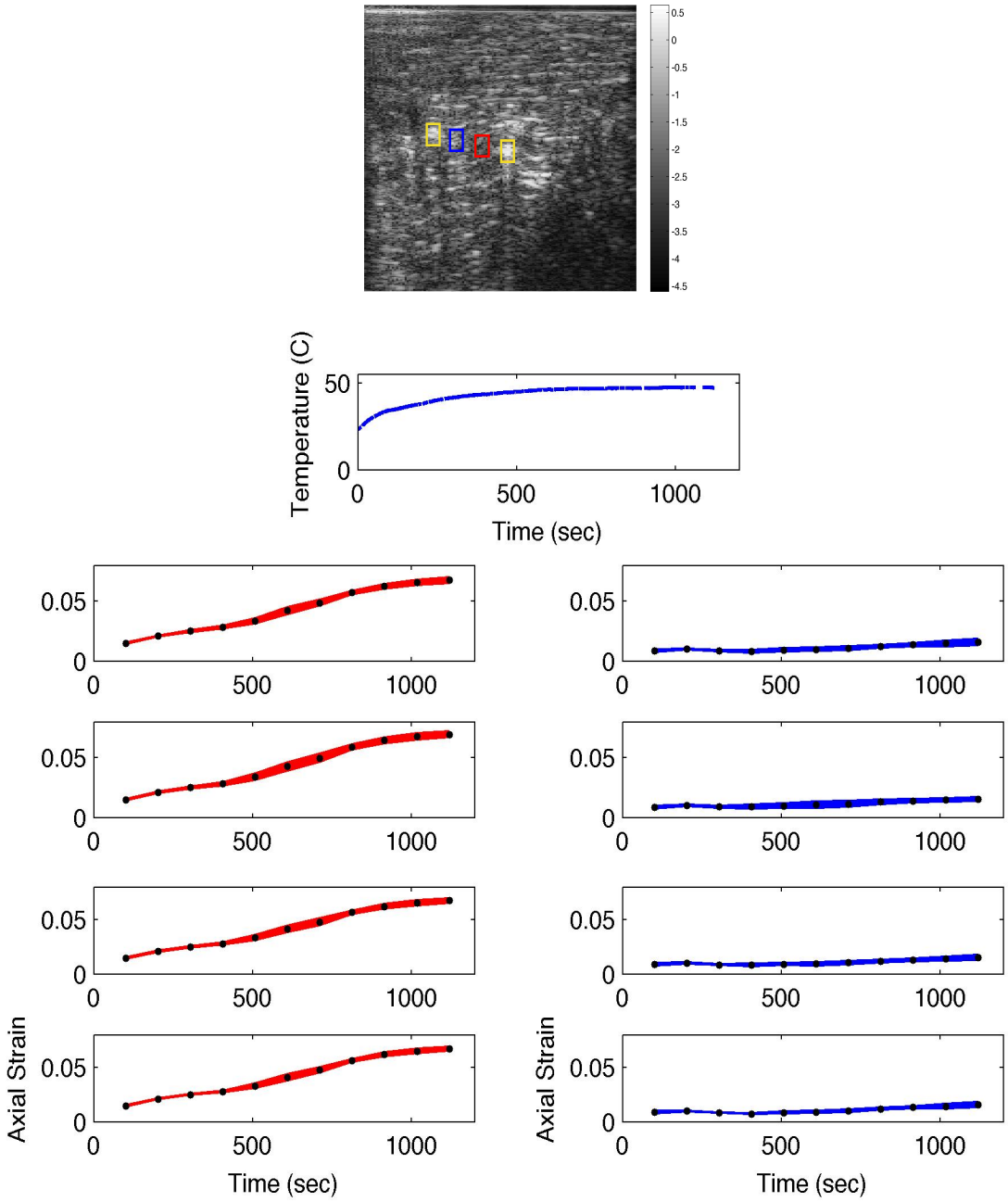

Figure 6.14: Two regions of interest (ROI1 red and ROI2 blue) were selected at equal distances to the ablator probe, to the temperature reading probe (both yellow) and to each other. (b) Temperature readings from the robot-held probe experiment (top subplot), followed by subplots presenting axial strain measurements in ROI1 (left column) and ROI2 (right column). From top to bottom: geometric mask (20 mm diameter), axial strain based masks with thresholds given by $x = 5$, 10 and 15 % of the strain range Mean axial strain values were calculated for every time step (black dots); the confidence region ($mean \pm 1 * stdev$) is shown as a shaded area.

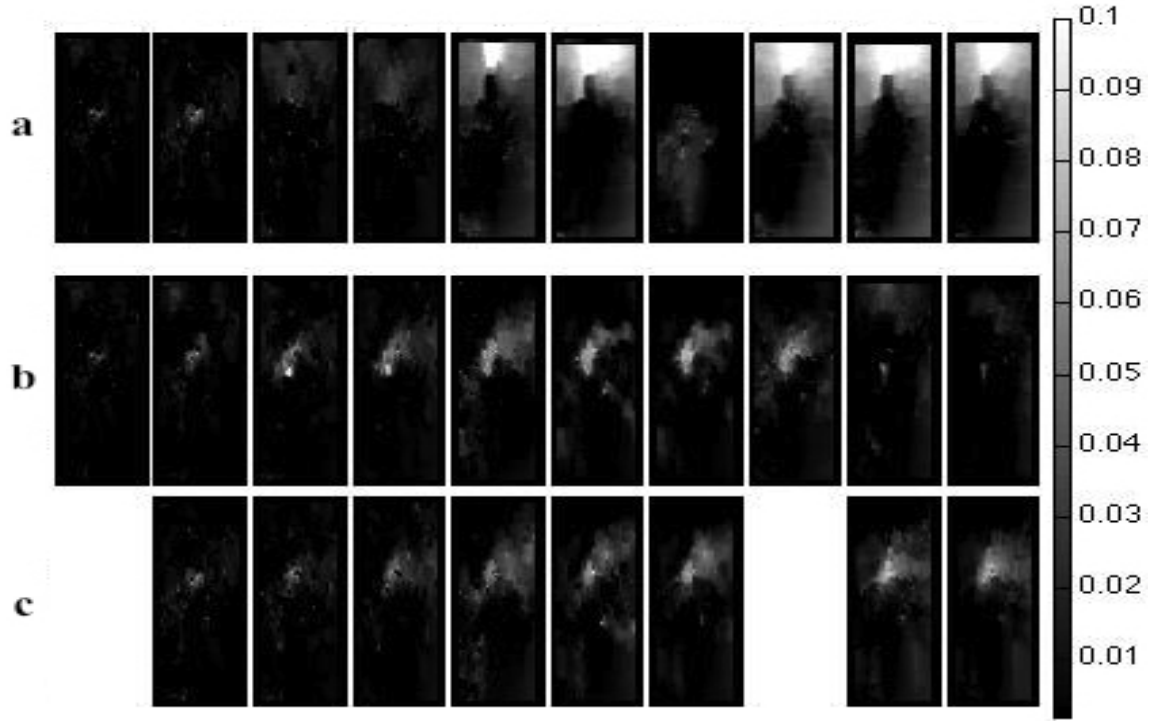

Figure 6.15: Axial strain in the first hand-held probe experiment, before and after removal of outliers. Original strain at the ten data collection points is shown on the top row (a). The strain in the remaining rows was generated using mask A for IMC: before (b) and after (c) outlier removal. Note the missing strain data for outlier cycles.

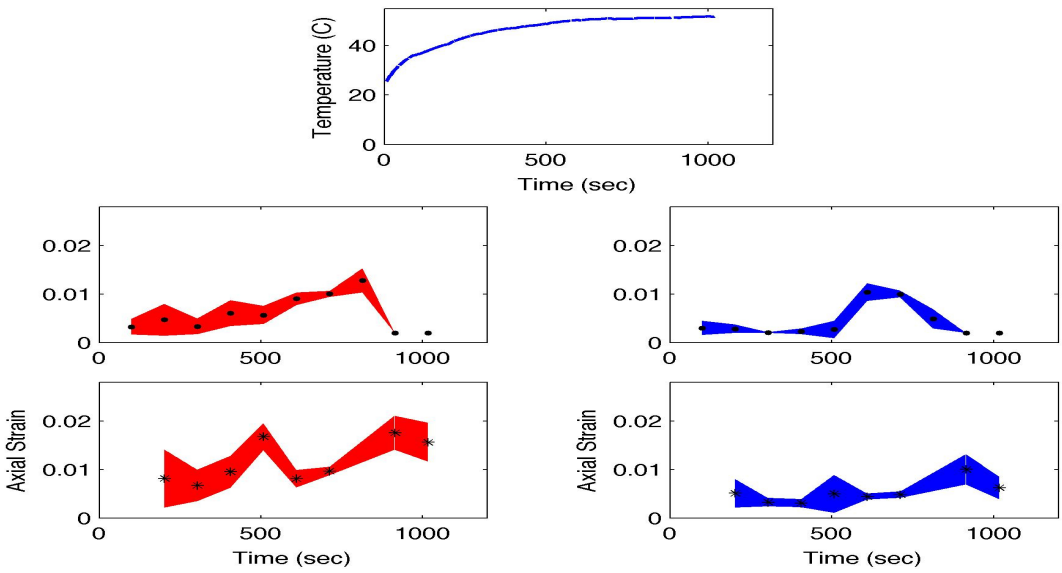

Figure 6.16: Temperature readings from the first hand-held probe experiment (top subplot), followed by subplots presenting axial strain measurements in ROI1 (left column) and ROI2 (right column), before (middle row) and after (bottom row) outlier removal. Note the missing strain data for outlier cycles.

The accumulation of axial strain in the two ROIs shows improved correlation with the temperature curve (Figure 6.18), but the missing data points prevent us from clearly unmasking the ablation lesion.

2. One cycle exhibits very high motion which corrupts all/some subsequent cycles.

   The second hand-held probe experiment is the one that experienced the highest non-heat-induced motion. The outlier cycles had very high amplitude of the detected motion vector. Figure 6.19 shows the strain results for this data set after the first iteration of motion compensation (middle row) and after the second iteration where data corresponding to outlier time cycles had been removed (bottom row). Although only one outlier cycle was detected and then removed,

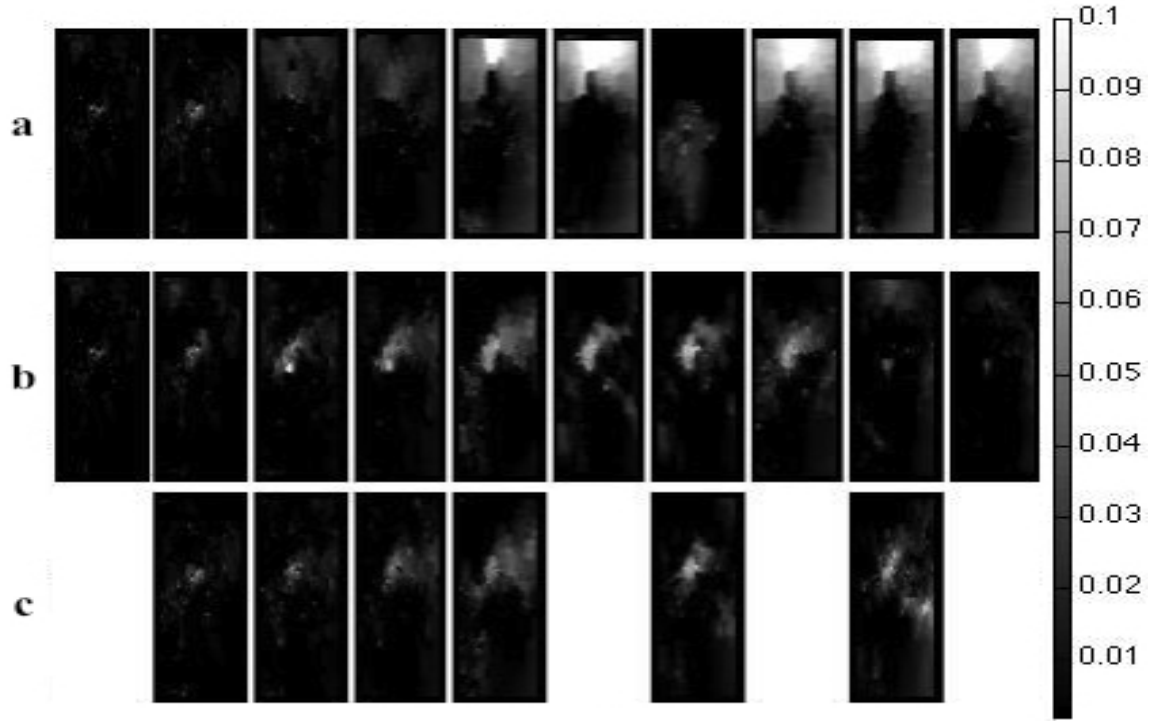

Figure 6.17: Axial strain in the first hand-held probe experiment, before and after removal of outliers. Original strain at the ten data collection points is shown on the top row (a). The strain in the remaining rows was generated using mask C for IMC: before (b) and after (c) outlier removal. Note the missing strain data for outlier cycles.

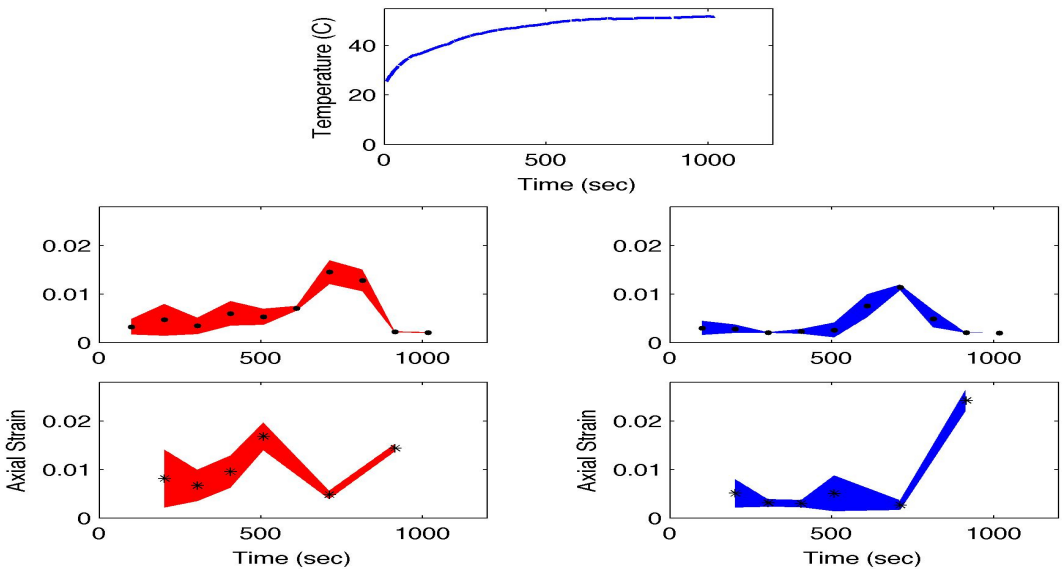

Figure 6.18: Temperature readings from the first hand-held probe experiment (top subplot), followed by subplots presenting axial strain measurements in ROI1 (left column) and ROI2 (right column), before (middle row) and after (bottom row) outlier removal. Note the missing strain data for outlier cycles.

there is no improvement in the strain estimation. One explanation could be that given the very high motion experienced at cycle 9 corrupted the data from the following cycle as well. In the outlier cycles the amplitude of the motion vector was on average $1.53mm$, more than 10 times higher than the average outlier amplitude in the first hand-held probe experiment $0.128mm$. The last cycle becomes the outlier of the second IMC iteration but it's removal in a potential third iteration has no finality, as it would not be able to produce a final strain image of the ablation lesion. There is no improvement in the correlation of the accumulation of axial strain with the temperature curve (Figure 6.20).

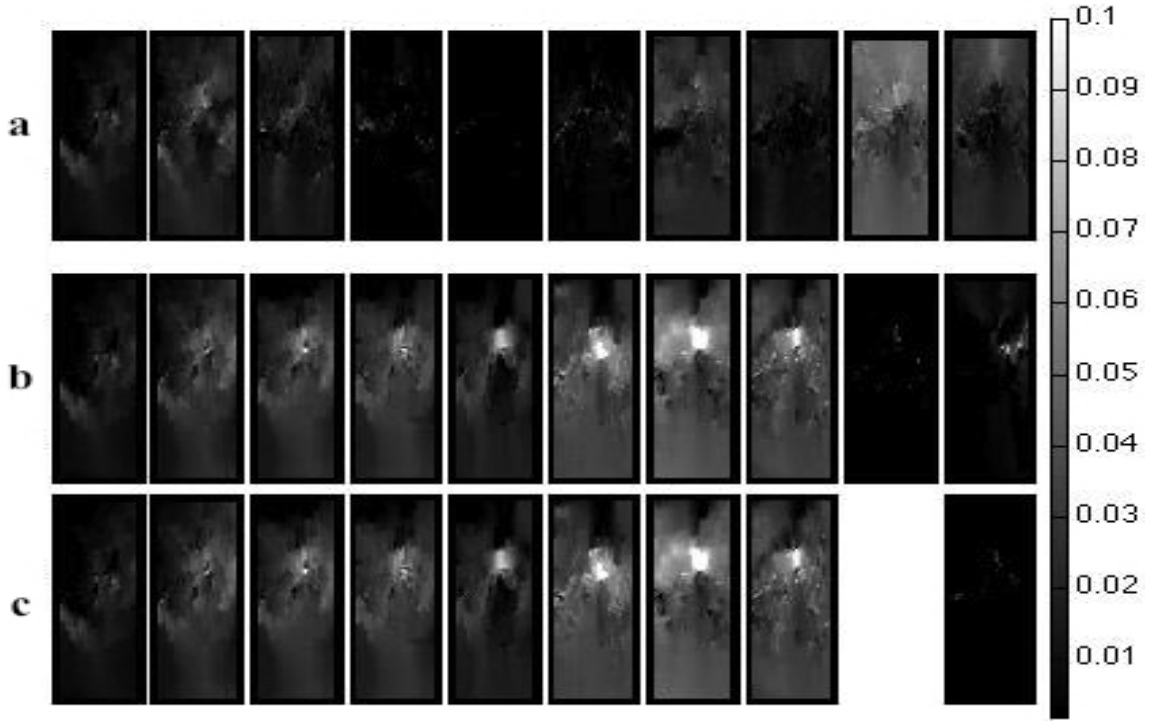

Figure 6.19: Axial strain in the second hand-held probe experiment, before and after removal of outliers. Original strain at the ten data collection points is shown on the top row (a). The strain in the remaining rows was generated using mask A for IMC: before (b) and after (c) outlier removal. Note the missing strain data for outlier cycles.

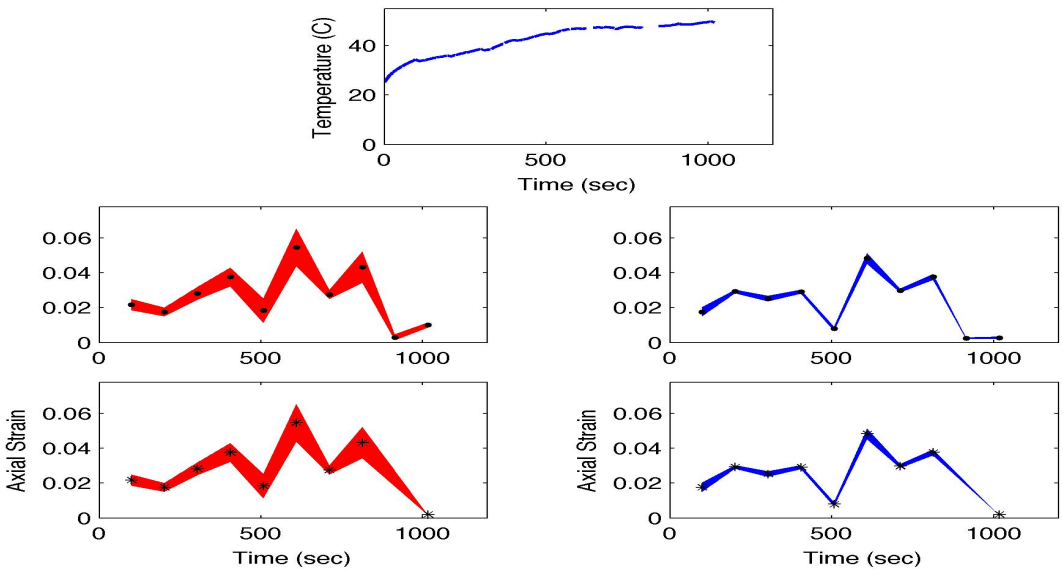

Figure 6.20: Temperature readings from the second hand-held probe experiment (top subplot), followed by subplots presenting axial strain measurements in ROI1 (left column) and ROI2 (right column), before (middle row) and after (bottom row) outlier removal. Note the missing strain data for outlier cycles.

6.5 Discussion and Conclusion

We have presented an algorithm for the detection and compensation of non-heat induced motion in tissue during thermal ablation. Our approach addresses the motion after each cycle of the ablation procedure. It can detect abnormally high motion in one cycle and consecutively remove the corrupted data from the heat-induced strain estimation. The motion compensation experiments run for 17 and 19 minutes respectively, which is much higher than anybody has attempted so far, to our knowledge. Our results show good estimation of the amplitude of the motion observed, with higher motion in setups where the ultrasound probe is held by the

operator versus a robot arm. Our estimated high strain areas aligned well in position and dimensions with the ablated lesions in gross pathology. Our motion compensation algorithm significantly improves the strain estimation in the robot-help probe setup. In hand-held probe experiments, a second iteration for motion compensation might be needed, as the strain estimation can be further improved by detecting and removing data points where outliers are detected among the motion vectors. If the detected motion is too high (above $1mm$ in amplitude), the algorithm may not be able to compensate.

Chapter 7

Conclusions and Future Work

7.1 Conclusions

Motion estimation in ultrasound has been suffering from the effects of signal decorrelation. We have developed robust tools in Chapter 4 which deal with areas of low signal correlation. We have shown improvement in displacement estimation and the ability to obtain artifact-free elastograms. Building onto the original DP elastography algorithm by Rivaz ([93, 92], we have addressed both the seed selection part of the algorithm and also the displacement propagation step. Our algorithm was validated on phantom, 2D and 3D *in vivo* and *ex vivo* animal and human data. Results were presented in Chapter 4.

CHAPTER 7.

In Chapter 5 we attempted to mosaic two or more motion maps in order to obtain an extended field of view elastogram. We succeeded to prove the concept in a very controlled laboratory setting, where we constrained the motion between image pairs at just the lateral direction. 2D and 3D phantom elastography mosaics were generated in this setting.

In thermal imaging, the heat-induced echo motion is on the order of microns and can be easily disturbed by motion from the operator, the patient or other environment sources. In Chapter 6 we developed a motion compensation algorithm capable of detecting and compensation for non heat-induced motion. Our algorithm was capable of detecting motion in two experimental settings: when the ultrasound probe was held by a human operator and also by a fixed robotic arm. Previous motion compensation techniques reported good results in thermal imaging experiments lasting less than 10 seconds. Our experiments lasted for 17 and 19 minutes during ex vivo ablation procedures, which is a significant improvement over previous literature reports. Results showed good estimation of the amplitude of the motion observed, with higher motion in the experimental setup where the ultrasound probe was held by the operator versus a robot arm. In the robot-held experiment, our motion compensation algorithm significantly improved the strain estimation. In the hand-held probe experiments, outlier data points were detected and removed and a second iteration of our motion estimation algorithm improved the strain estimation as well.

7.2 Future Work

Improvements in ultrasound elastography are difficult to quantify. Although our robust displacement estimation tools improve our ability to generate artifact-free elastograms, the lack of a clear ground truth data with respect with hard vs soft tissue makes it hard to assess this improvement quantitatively. An *in vivo* study is needed where gross pathology sections can be perfectly aligned with the ultrasound data planes. This can insure one-to-one correspondences when trying to assess parameters such as size and position of detected lesions. Furthermore, rigorous clinical trials are needed to asses the true clinical impact of our improved elastography technique.

Many clinical applications can benefit from improved ultrasound displacement estimation. Our lab has been working on integrating a laparoscopic ultrasound probe with the DaVinci surgical robot. Efforts are under way to incorporate a robust elastography algorithm for prostatic, renal and other abdominal surgery applications. The integration with the MUSIIC ultrasound pipeline is under way, which will ensure seamless data acquizition, processing, visualization and interaction with the results. Graphical processing units can be used for the displacement estimation step of the algorithm as parallelization can significantly speed up run times. More experiments are needed to assess the frame-per rate capability in this environment.

With respect to ultrasound elastography mosaics, more efforts are needed to

validate the algorithm beyond the proof-of-concept presented in Chapter 5. In three dimensional data, integration with the frame selection technique of Foroughi ([37]) needs testing in *in vivo* and *ex vivo* applications. As the laparoscopic ultrasound probe has a limited size, the surgical application would benefit most from extended field of view elastography capabilities. Efforts are also needed for visualizing the resulting strain mosaics. A big area of future work should include a special evaluation of elastography (and 2D/3D mosaicking) in the robotic environment:

1. How the elastography results are presented to the user (surgeon)?,
2. How the user is allowed to interact with the data?
3. What are the resulting surgical outcomes specific to each application?

Thermal imaging results presented in Chapter 6 relied on data from three experiments. More validation is needed in laboratory setting, followed by *in vivo* animal or human experiments. Clinical trials with high quality ground truth data are also needed here (just like in elastography), where pathology data needs to be evaluated from sections oriented in the same plane with the ultrasound data acquisition areas. Another line of future work is to compare heat-induced echo strain with MRI strain imaging in *in vivo* experiments.

Bibliography

[1] S. K. Alam, D. W. Richards, and K. J. Parker. Detection of intraocular pressure change in the eye using sonoelastic doppler ultrasound. *Ultrasound Medicine & Biology*, 20:751–758, 1994.

[2] A. N. Amini, E. S. Ebbini, and T. Georgiou. Noninvasive estimation of tissue temperature via high-resolution spectral analysis techniques. *IEEE Trans. Biomed. Eng.*, 52(2):221–228, 2005.

[3] W. Artibani, S. Fracalanza, S. Cavalleri, M. Iafrate, M. Aragona, G. Novara, M. Gardiman, and V. Ficarra. Learning curve and preliminary experience with da vinci-assisted laparoscopic radical prostatectomy. *Urologia Internationalis*, 80(3):237–244, 2008.

[4] S. I. Awad and J. T. Yen. 3D Strain Imaging Using a Rectilinear 2D Array. *Ultrasonic Imaging*, 29(4):220–230, 2007.

BIBLIOGRAPHY

[5] K. K. Badani, S. Kaul, and M. Menon. Evolution of robotic radical prostatectomy: assessment after 2766 procedures. *Cancer*, 110(9):1951–1958, 2007.

[6] M. J. Barry, P. M. Gallagher, J. S. Skinner, and F. J. Fowler. Adverse effects of robotic-assisted laparoscopic versus open retropubic radical prostatectomy among a nationwide random sample of medicare-age men. *Journal of Clinical Oncology*, 30(5):513–518, 2012.

[7] M. Bayat, J. Ballard, and E. Ebbini. Adaptive motion compensation for in vivo ultrasound temperature estimation. In *Ultrasonics Symposium (IUS), 2013 IEEE International*, pages 1797–1800, July 2013.

[8] J. Berryhill, Roy, J. Jhaveri, R. Yadav, R. Leung, S. Rao, A. El-Hakim, and A. Tewari. Robotic prostatectomy: a review of outcomes compared with laparoscopic and open approaches. *Urology*, 72(1):15–23, 2008.

[9] A. Bill-Axelson, L. Holmberg, M. Ruutu, H. Garmo, J. R. Stark, C. Busch, S. Nordling, M. Hggman, S. Andersson, S. Bratell, A. Spngberg, J. Palmgren, G. Steineck, H. Adami, and J. Johansson. Radical prostatectomy versus watchful waiting in early prostate cancer. *The New England Journal of Medicine*, 364(18):1708–1717, 2011.

[10] S. Billings, N. Deshmukh, H. J. Kang, R. H. Taylor, and E. Boctor. System for robot-assisted real-time laparoscopic ultrasound elastography. In *Proceedings of the SPIE Medical Imaging*, volume 67, pages 8316–8316, February 2012.

[11] E. Boctor, G. Fichtinger, A. Yeung, M. Awad, R. Taylor, and M. Choti. Robotic strain imaging for monitoring thermal ablation of liver. In C. Barillot, D. Haynor, and P. Hellier, editors, *Medical Image Computing and Computer-Assisted Intervention C MICCAI 2004*, volume 3217 of *Lecture Notes in Computer Science*, pages 81–88. Springer Berlin Heidelberg, 2004.

[12] E. Boctor, G. Fischer, M. Choti, G. Fichtinger, and R. Taylor. A dual-armed robotic system for intraoperative ultrasound guided hepatic ablative therapy: a prospective study. In *Robotics and Automation, 2004. Proceedings. ICRA '04. 2004 IEEE International Conference on*, volume 3, pages 2517–2522 Vol.3, April 2004.

[13] G. N. Box and T. E. Ahlering. Robotic radical prostatectomy: long-term outcomes. *Current Opinion in Urology*, 18(2):173–179, 2008.

[14] A. L. Burnett. Erectile dysfunction following radical prostatectomy. *JAMA: the journal of the American Medical Association*, 293(21):2648–2653, 2005.

[15] I. Céspedes, J. Ophir, H. Ponnekanti, and N. Maklad. Elastography: elasticity imaging using ultrasound with application to muscle and breast in vivo. *Ultrasonic Imaging*, 15:73–88, 1993.

[16] C. H. Cha, F. T. J. Lee, J. M. Gurney, B. K. Markhardt, T. F. Warner, F. Kelcz, and D. M. Mahvi. Ct versus sonography for monitoring radiofrequency ablation in a porcine liver. *AJR Am J Roentgenol*, 175(3):705–711, 2000.

BIBLIOGRAPHY

[17] R. Chandrasekhar, J. Ophir, T. Krouskop, and K. Ophir. Elastographic image quality vs. tissue motion in vivo. *Ultrasound Med Biol*, 32(6):847–855, Jun 2006.

[18] P. Chaturvedi, M. Insana, and T. Hall. 2D companding for noise reduction in strain imaging. *IEEE Transactions on Ultrasonics, Ferroelectrics, and Frequency Control*, 45(1):179–191, January 1998.

[19] L. Chen, G. M. Treece, J. E. Lindop, A. H. Gee, and R. W. Prager. A quality-guided displacement tracking algorithm for ultrasonic elasticity imaging. *Medical Image Analysis*, 13(2):286–296, 2009.

[20] D. Christensen. *Ultrasonic Bioinstrumentation*. Third Edition. Press, 2004.

[21] D. L. Cochlin, R. H. Ganatra, and D. F. R. Griffiths. Elastography in the detection of prostatic cancer. *Clinical Radiology*, 57(11):1014–1020, 2002.

[22] R. J. Cohen, B. A. Shannon, M. Phillips, R. E. Moorin, T. M. Wheeler, and K. L. Garrett. Central zone carcinoma of the prostate gland: a distinct tumor type with poor prognostic features. *The Journal of Urology*, 179(5):1762–1767, 2008.

[23] C. M. Coley, M. J. Barry, C. Fleming, and A. G. Mulley. Early detection of prostate cancer. part i: Prior probability and effectiveness of tests. the american college of physicians. *Annals of Internal Medicine*, 126(5):394–406, 1997.

[24] J. Colombo, Jose R, B. Santos, J. Hafron, T. Gianduzzo, G. Haber, and J. H.

Kaouk. Robotic assisted radical prostatectomy: surgical techniques and outcomes. *International Braz J Urol: Official Journal of the Brazilian Society of Urology*, 33(6):803–809, 2007.

[25] W. F. Daehnert, U. M. Hamper, J. C. Eggleston, P. C. Walsh, and R. C. Sanders. Prostatic evaluation by transrectal sonography with histopathologic correlation: the echopenic appearance of early carcinoma. *Radiology*, 158(1):97–102, 1986.

[26] C. L. DeKorte, E. I. Cespedes, A. F. W. van der Steen, and C. T. Lancee. Intravascular elasticity imaging using ultrasound: feasibility studies in phantoms. *Ultrasound in Medicine & Biology*, 23:735–746, 1997.

[27] J.-F. Deprez, E. Brusseau, C. Schmitt, G. Cloutier, and O. Basset. 3D estimation of soft biological tissue deformation from radio-frequency ultrasound volume acquisitions. *Medical Image Analysis*, 13(1):116–127, 2009.

[28] D. Dutta, A. Mahmoud, S. Leers, and K. Kim. Motion artifact reduction in ultrasound based thermal strain imaging of atherosclerotic plaques using time-series analysis. *Ultrasonics, Ferroelectrics and Frequency Control, IEEE Transactions on*, 60(8):1660–1668, August 2013.

[29] S. Y. Emelianov, X. Chen, M. O'Donnell, B. Knipp, D. Myers, T. W. Wakefield, and J. M. Rubin. Triplex ultrasound: elasticity imaging to age deep venous thrombosis. *Ultrasound in Medicine & Biology*, 28(6):757–767, 2002.

[30] H. Eskandari, S. E. Salcudean, and R. Rohling. Viscoelastic parameter estimation based on spectral analysis. *IEEE Trans Ultrason Ferroelectr Freq Control*, 55(7):1611–1625, Jul 2008.

[31] D. H. Evans, J. A. Jensen, and M. B. Nielsen. Ultrasonic colour doppler imaging. *Interface Focus*, 1(4):490–502, 2011.

[32] A. Fenster and D. Downey. 3-D ultrasound imaging: a review. *Engineering in Medicine and Biology Magazine, IEEE*, 15(6):41–51, 1996.

[33] V. Ficarra, S. Cavalleri, G. Novara, M. Aragona, and W. Artibani. Evidence from robot-assisted laparoscopic radical prostatectomy: a systematic review. *European Urology*, 51(1):45–55, 2007.

[34] T. Fisher, J. Jiang, and T. Hall. Volumetric strain imaging. In *Ultrasonics Symposium (IUS), IEEE*, pages 355–358, 2007.

[35] T. G. Fisher, T. J. Hall, S. Panda, M. S. Richards, P. E. Barbone, J. Jiang, J. Resnick, and S. Barnes. Volumetric Elasticity Imaging with a 2-D CMUT Array. *Ultrasound in Medicine and Biology*, 36(6):978–990, 2010.

[36] I. Fleming, H. Rivaz, E. Boctor, and G. Hager. Robust dynamic programming method for ultrasound elastography. *Proceedings of the SPIE Medical Imaging*, 8320(1):83201–83206, 2012.

[37] P. Foroughi, H.-J. Kang, D. A. Carnegie, M. G. van Vledder, M. A. Choti,

G. D. Hager, and E. M. Boctor. A Freehand Ultrasound Elastography System With Tracking for *In Vivo* Applications. *Ultrasound in Medicine & Biology*, 39(2):211–225, 2013.

[38] P. Foroughi, H. Rivaz, I. N. Fleming, G. D. Hager, and E. M. Boctor. Tracked ultrasound elastography (TrUE). In *Proceedings of the International Conference on Medical Image Computing and Computer-Assisted Intervention*, MICCAI'10, pages 9–16, 2010.

[39] L. Gao, K. J. Parker, R. M. Lerner, and S. F. Levinson. Imaging of the elastic properties of tissue – a review. *Ultrasound in Medicine & Biology*, 22(8):959–977, 1996.

[40] B. Garra, E. Céspedes, J. Ophir, S. Spratt, R. Zuurbier, C. Magnant, and M. Pennanen. Elastography of breast lesions: initial clinical results. *Radiology*, 202(1):79–86, 1997.

[41] A. H. Gee, G. M. Treece, R. W. Prager, C. J. Cash, and L. Berman. Rapid registration for wide field of view freehand three-dimensional ultrasound. *IEEE Transactions on Medical Imaging*, 22(11):1344–1357, 2003.

[42] S. N. Goldberg, G. S. Gazelle, C. C. Compton, P. R. Mueller, and K. K. Tanabe. Treatment of intrahepatic malignancy with radiofrequency ablation: radiologic-pathologic correlation. *Cancer*, 88(11):2452–2463, 2000.

[43] J. Greenleaf, M. Fatemi, and M. Insana. Selected methods for imaging elastic properties of biological tissues. *Annu. Rev. Biomed. Eng.*, 5:57–78, April 2003.

[44] T. J. Hall. AAPM/RSNA Physics Tutorial for Residents: Topics in US Beyond the Basics: Elasticity Imaging with US. *Radiographics*, 23:1657–1671, 2003.

[45] T. J. Hall, Y. Zhu, and C. S. Spalding. In vivo real-time freehand palpation imaging. *Ultrasound Med Biol*, 29(3):427–435, Mar 2003.

[46] R. J. Housden, L. Chen, A. H. Gee, G. M. Treece, C. Uff, J. Fromageau, L. Garcia, R. W. Prager, N. L. Dorward, and J. C. Bamber. A new method for the acquisition of ultrasonic strain image volumes. *Ultrasound in Medicine & Biology*, 37(3):434–441, 2011.

[47] T. H. Hsu, M. E. Fidler, and I. S. Gill. Radiofrequency ablation of the kidney: acute and chronic histology in porcine model. *Urology*, 56(5):872–875, Nov 2000.

[48] J. C. Hu, Q. Wang, C. L. Pashos, S. R. Lipsitz, and N. L. Keating. Utilization and outcomes of minimally invasive radical prostatectomy. *Journal of Clinical Oncology: Official Journal of the American Society of Clinical Oncology*, 26(14):2278–2284, 2008.

[49] A. Itoh, E. Ueno, E. Tohno, H. Kamma, H. Takahashi, T. Shiina, M. Yamakawa, and T. Matsumura. Breast disease: clinical application of us elastography for diagnosis. *Radiology*, 239(2):341–350, May 2006.

[50] J. Jiang and T. Hall. A regularized real-time motion tracking algorithm using dynamic programming for ultrasonic strain imaging. In *IEEE Ultrasonics Symp.*, pages 606–609, Vancouver, Canada, October 2006.

[51] J. Jiang, T. J. Hall, and A. M. Sommer. A novel image formation method for ultrasonic strain imaging. *Ultrasound in Medicine & Biology*, 33(4):643–652, 2007.

[52] H. Kang, P. Stolka, and E. Boctor. OpenITGLinkMUSiiC: A Standard Communications Protocol for Advanced Ultrasound Research. *The Midas Journal - Computer Assisted Intervention; MICCAI 2011, International Workshop on Systems and Architectures for Computer Assisted Interventions*, August 2011.

[53] M. Z. Kiss, M. J. Daniels, and T. Varghese. Investigation of temperature-dependent viscoelastic properties of thermal lesions in ex vivo animal liver tissue. *J Biomech*, 42(8):959–966, May 2009.

[54] K. Koenig, U. Scheipers, A. Pesavento, A. Lorenz, H. Ermert, and T. Senge. Initial experiences with real-time elastography guided biopsies of the prostate. *The Journal of Urology*, 174(1):115–117, 2005.

[55] T. A. Krouskop, D. R. Dougherty, and S. F. Levinson. A pulsed doppler ultrasonic system for making noninvasive measurements of the mechanical properties of soft tissues. *Journal Rehabil Res Dev*, 24:1–8, 1987.

[56] M. Krueger, A. Pesavento, H. Ermert, K. Hiltawsky, L. Heuser, H. Rosenthal, and A. Jensen. Ultrasonic strain imaging of the female breast using phase root seeking and three-dimensional optical flow. In *Ultrasonics Symposium (IUS), 1998 IEEE*, volume 2, pages 1757 –1760, 1998.

[57] R. M. Lerner, S. R. Huang, and K. J. Parker. Sonoelasticity images derived from ultrasound signals in mechanically vibrated tissues. *Ultrasound in medicine & Biology*, 16:231–239, 1990.

[58] R. M. Lerner and K. J. Parker. Sono-elasticity in ultrasonic tissue characterization and echographic imaging. In *Proceedings of 7th European Community Workshop (Ed. J. M. Thijssen), Nijmegen, The Netherlands*, 1987.

[59] J. Leven, D. Burschka, R. Kumar, G. Zhang, S. Blumenkranz, X. D. Dai, M. Awad, G. D. Hager, M. Marohn, M. Choti, C. Hasser, and R. H. Taylor. DaVinci canvas: a telerobotic surgical system with integrated, robot-assisted, laparoscopic ultrasound capability. *Medical Image Computing and Computer-Assisted Intervention: MICCAI ... International Conference on Medical Image Computing and Computer-Assisted Intervention*, 8(Pt 1):811–818, 2005.

[60] J. S. Lewin, C. F. Connell, J. L. Duerk, Y.-C. Chung, M. E. Clampitt, J. Spisak, G. S. Gazelle, and J. R. Haaga. Invited. interactive mri-guided radiofrequency interstitial thermal ablation of abdominal tumors: Clinical trial for evaluation

of safety and feasibility. *Journal of Magnetic Resonance Imaging*, 8(1):40–47, 1998.

[61] J. R. Leyendecker, G. D. r. Dodd, G. A. Halff, V. A. McCoy, D. H. Napier, L. G. Hubbard, K. N. Chintapalli, S. Chopra, W. K. Washburn, R. M. Esterl, F. G. Cigarroa, R. E. Kohlmeier, and F. E. Sharkey. Sonographically observed echogenic response during intraoperative radiofrequency ablation of cirrhotic livers: pathologic correlation. *AJR Am J Roentgenol*, 178(5):1147–1151, May 2002.

[62] J. Lindop, G. Treece, A. Gee, and R. Prager. 3D elastography using freehand ultrasound. *Ultrasound in Medicine & Biology*, 32(4):529–545, 2006.

[63] J. Lindop, G. Treece, A. Gee, and R. Prager. An intelligent interface for free-hand strain imaging. *Ultrasound in Medicine & Biology*, 34(7):1117–1128, 2008.

[64] A. Lorenz, A. Pesavento, M. Pesavento, and H. Ermert. Three-dimensional strain imaging and related strain artifacts using an ultrasonic 3D abdominal probe. In *Ultrasonics Symposium (IUS), 1999 IEEE*, volume 2, pages 1657–1660, 1999.

[65] R. Maass-Moreno and C. A. Damianou. Noninvasive temperature estimation in tissue via ultrasound echo-shifts. Part I, Analytical Model. *J Acoust Soc Am*, 100(4):2514–2521, 1996.

[66] R. Maass-Moreno, C. A. Damianou, and N. T. Sanghvi. Noninvasive temperature estimation in tissue via ultrasound echo-shifts. Part II. In Vitro study. *J Acoust Soc Am*, 100(4):2522–2530, 1996.

[67] S. Mallidi, T. Larson, J. Tam, P. P. Joshi, A. Karpiouk, K. Sokolov, and S. Emelianov. Multiwavelength photoacoustic imaging and plasmon resonance coupling of gold nanoparticles for selective detection of cancer. *Nano Letters*, 9(8):2825–2831, 2009.

[68] J. A. Mann and W. Walker. A constrained adaptive beamformer for medical ultrasound: initial results. In *Ultrasonics Symposium, 2002. Proceedings. 2002 IEEE*, volume 2, pages 1807–1810 vol.2, Oct 2002.

[69] G. Mase, R. Smelser, and G. Mase. *Continuum Mechanics for Engineers, Third Edition*. Computational Mechanics and Applied Analysis Series. CRC Press, 2009.

[70] N. McDannold. Quantitative mri-based temperature mapping based on the proton resonant frequency shift: Review of validation studies. *International Journal of Hyperthermia*, 21(6):533–546, 2005.

[71] J. P. McGhana and G. D. r. Dodd. Radiofrequency ablation of the liver: current status. *AJR Am J Roentgenol*, 176(1):3–16, 2001.

[72] J. E. McNeal, E. A. Redwine, F. S. Freiha, and T. A. Stamey. Zonal distribution

of prostatic adenocarcinoma. correlation with histologic pattern and direction of spread. *The American Journal of Surgical Pathology*, 12(12):897–906, 1988.

[73] M. F. Meloni, S. N. Goldberg, T. Livraghi, F. Calliada, P. Ricci, M. Rossi, D. Pallavicini, and R. Campani. Hepatocellular carcinoma treated with radiofrequency ablation: comparison of pulse inversion contrast-enhanced harmonic sonography, contrast-enhanced power doppler sonography, and helical ct. *AJR Am J Roentgenol*, 177(2):375–380, Aug 2001.

[74] N. R. Miller, J. C. Bamber, and P. M. Meany. Fundamental limitations of noninvasive temperature imaging by means of ultrasound echo strain estimation. *Ultrasound in Medicine & Biology*, 28:1319–1333, 2002.

[75] R. L. Nasoni and T. Bowen. Ultrasonic speed as a parameter for noninvasive thermometry. *Automedica*, 8:269–281, 1987.

[76] National Cancer Institutes. Tracking the rise of robotic surgery for prostate cancer. *NCI Cancer Bulletin*, 8(16):4, August 2011.

[77] B. Nelson, M. Kaufman, G. Broughton, M. S. Cookson, S. S. Chang, S. D. Herrell, R. G. Baumgartner, and J. Smith, Joseph A. Comparison of length of hospital stay between radical retropubic prostatectomy and robotic assisted laparoscopic prostatectomy. *The Journal of Urology*, 177(3):929–931, 2007.

[78] K. Nightingale, M. S. Soo, R. Nightingale, and G. Trahey. Acoustic radiation

force impulse imaging: in vivo demonstration of clinical feasibility. *Ultrasound Med Biol*, 28(2):227–235, Feb 2002.

[79] M. Nikfarjam and C. Christophi. Interstitial laser thermotherapy for liver tumours. *Br J Surg*, 90(9):1033–1047, Sep 2003.

[80] M. O'Donnell, A. R. Skovoroda, and B. M. Shapo. Measurement of arterial wall motion using fourier based speckle tracking algorithms. In *Proceedings of IEEE Ultrasound Symposium*, pages 1101–1104, 1991.

[81] M. O'Donnell, A. R. Skovoroda, B. M. Shapo, and S. Y. Emelianov. Internal displacement and strain imaging using ultrasonic speckle tracking. *IEEE Transactions on Ultrasonics, Ferroelectrics, and Frequency Control*, 41(3):314–325, 1994.

[82] J. Ophir, S. K. Alam, B. Garra, F. Kallel, E. Konofagou, T. Krouskop, and T. Varghese. Elastography: ultrasonic estimation and imaging of the elastic properties of tissues. *Proceedings of the Institution of Mechanical Engineers. Part H, Journal of Engineering in Medicine*, 213(3):203–233, 1999.

[83] J. Ophir, I. Céspedes, H. Ponnekanti, Y. Yazdi, and X. Li. Elastography: a quantitative method for imaging the elasticity of biological tissues. *Ultrasonic Imaging*, 13:111–134, 1991.

[84] K. J. Parker, L. Gao, R. M. Lerner, and S. F. Levinson. Techniques for elastic

imaging: A review. *IEEE Engineering in Medicine and Biology*, 15(6):52–59, 1996.

[85] M. Pernot, M. Tanter, J. Bercoff, K. Waters, and M. Fink. Temperature estimation using ultrasonic spatial compounding. *Ultrasonics, Ferroelectrics and Frequency Control, IEEE Transactions on*, 51(5):606–615, May 2004.

[86] A. Pesavento, C. Perrey, M. Krueger, and H. Ermert. A time-efficient and accurate strain estimation concept for ultrasonic elastography using iterative phase zero estimation. *Ultrasonics, Ferroelectrics and Frequency Control, IEEE Transactions on*, 46(5):1057–1067, September 1999.

[87] M. Pompili, L. Riccardi, M. Covino, B. Barbaro, C. Di Stasi, R. Orefice, G. Gasbarrini, and G. L. Rapaccini. Contrast-enhanced gray-scale harmonic ultrasound in the efficacy assessment of ablation treatments for hepatocellular carcinoma. *Liver International*, 25(5):954–961, 2005.

[88] T. C. Poon and R. N. Rohling. Three-dimensional extended field-of-view ultrasound. *Ultrasound in Medicine & Biology*, 32(3):357–369, 2006.

[89] R. S. Pruthi and E. M. Wallen. Current status of robotic prostatectomy: promises fulfilled. *The Journal of Urology*, 181(6):2420–2421, 2009.

[90] K. Rajpoot, J. A. Noble, V. Grau, C. Szmigielski, and H. Becher. Multiview RT3D echocardiography image fusion. In N. Ayache, H. Delingette, and M. Ser-

mesant, editors, *Functional Imaging and Modeling of the Heart*, volume 5528, pages 134–143. Springer Berlin Heidelberg, Berlin, Heidelberg, 2009.

[91] R. Righetti, F. Kallel, R. J. Stafford, R. E. Price, T. A. Krouskop, J. D. Hazle, and J. Ophir. Elastographic characterization of hifu-induced lesions in canine livers. *Ultrasound in Medicine & Biology*, 25(7):1099–1113, 1999.

[92] H. Rivaz, E. Boctor, M. Choti, and G. Hager. Real-time regularized ultrasound elastography. *IEEE Transactions on Medical Imaging*, 30(4):928–945, 2011.

[93] H. Rivaz, E. Boctor, P. Foroughi, R. Zellars, G. Fichtinger, and G. Hager. Ultrasound elastography: a dynamic programming approach. *IEEE Transactions on Medical Imaging*, 27(10):1373–1377, 2008.

[94] H. Rivaz, I. Fleming, L. Assumpcao, G. Fichtinger, U. Hamper, M. Choti, G. Hager, and E. Boctor. Ablation monitoring with elastography: 2d in-vivo and 3d ex-vivo studies. *Med Image Comput Comput Assist Interv*, 11(Pt 2):458–466, 2008.

[95] H. Rivaz, I. Fleming, M. Matinfar, O. Ahmad, A. Khamene, M. Choti, G. Hager, and E. Boctor. Ablation monitoring with a regularized 3d elastography technique. In *Ultrasonics Symposium, 2008. IUS 2008. IEEE*, pages 308–312, Nov 2008.

[96] D. F. Saldanha, V. L. Khiatani, T. C. Carrillo, F. Y. Yap, J. T. Bui, M. G.

Knuttinen, C. A. Owens, and R. C. Gaba. Current tumor ablation technologies: basic science and device review. *Semin Intervent Radiol*, 27(3):247–254, 2010.

[97] C. Salloum and D. Castaing. Surgical margin status in hepatectomy for liver tumors. *Bull Cancer*, 95(12):1183–1191, 2008.

[98] G. Salomon, J. Kllerman, I. Thederan, F. K. H. Chun, L. Budus, T. Schlomm, H. Isbarn, H. Heinzer, H. Huland, and M. Graefen. Evaluation of prostate cancer detection with ultrasound real-time elastography: a comparison with step section pathological analysis after radical prostatectomy. *European Urology*, 54(6):1354–1362, 2008.

[99] J. T. Sanctis, S. N. Goldberg, and P. R. Mueller. Percutaneous treatment of hepatic neoplasms: A review of current techniques. *CardioVascular and Interventional Radiology*, 21(4):273–296, 1998.

[100] J. Schaar, C. De Korte, F. Mastik, L. Van Damme, R. Krams, P. Serruys, and A. Van Der Steen. Three-dimensional palpography of human coronary arteries: Ex vivo validation and in-patient evaluation. *Herz*, 30(2):125–133, 2005.

[101] C. Schneider, P. Peng, R. Taylor, G. Dachs, C. Hasser, S. DiMaio, and M. Choti. Robot-assisted laparoscopic ultrasonography for hepatic surgery. *Surgery*, 151(5):756–762, 2012.

[102] C. M. Schneider, G. W. Dachs, II, C. J. Hasser, M. A. Choti, S. P. DiMaio, and

R. H. Taylor. Robot-assisted laparoscopic ultrasound. In *Proceedings of the First international conference on Information processing in computer-assisted interventions*, IPCAI'10, pages 67–80, 2010.

[103] R. Seip and E. S. Ebbini. Noninvasive estimation of tissue temperature response to heating fields using diagnostic ultrasound. *IEEE Transanctions Biomedical Engineering*, 42(8):828–839, 1995.

[104] R. Seip, P. VanBaren, C. Cain, and E. S. Ebbini. Noninvasive spatio-temporal temperature change estimation using diagnostic ultrasound. *IEEE Transactions on Ultrasonics, Ferroelectrics, and Frequency Control*, 43:1068–1078, 1996.

[105] R. Siegel, D. Naishadham, and A. Jemal. Cancer statistics, 2013. *CA: A Cancer Journal for Clinicians*, 63(1):11–30, 2013.

[106] C. Simon, P. VanBaren, and E. S. Ebbini. Two-dimensional temperature estimation using diagnostic ultrasound. *IEEE Transactions on Ultrasonics, Ferroelectrics, and Frequency Control*, 45(4):1088–1099, 1998.

[107] S. Singhy and C. Riviere. Physiological tremor amplitude during retinal microsurgery. In *Bioengineering Conference, 2002. Proceedings of the IEEE 28th Annual Northeast*, pages 171–172, 2002.

[108] A. E. Siperstein, S. J. Rogers, P. D. Hansen, and A. Gitomirsky. Laparo-

scopic thermal ablation of hepatic neuroendocrine tumor metastases. *Surgery*, 122(6):1147–1154, Dec 1997.

[109] L. Solbiati, T. Ierace, M. Tonolini, and L. Cova. Guidance and monitoring of radiofrequency liver tumor ablation with contrast-enhanced ultrasound. *European Journal of Radiology*, 51, Supplement(0):S19 – S23, 2004.

[110] R. Souchon, O. Rouviere, A. Gelet, V. Detti, S. Srinivasan, J. Ophir, and J. Y. Chapelon. Visualization of hifu lesions using elastography of the human prostate in vivo: Preliminary results. *Ultrasound in Medicine & Biology*, 29(7):1007–1015, 2003.

[111] P. Stolka, H. Kang, and E. Boctor. The MUSiiC Toolkit: Modular Real-Time Toolkit for Advanced Ultrasound Research. *The Midas Journal - Computer Assisted Intervention; MICCAI 2010, International Workshop on Systems and Architectures for Computer Assisted Interventions*, August 2010.

[112] W. L. Straube and R. M. Arthur. Theoretical estimation of the temperature dependence of backscattered ultrasonic power for noninvasive thermometry. *Ultrasound Med Biol*, 20(9):915–922, 1994.

[113] L. Su, R. E. Link, S. B. Bhayani, W. Sullivan, and C. P. Pavlovich. Nerve-sparing laparoscopic radical prostatectomy: replicating the open surgical technique. *Urology*, 64(1):123–127, 2004.

[114] M. Sumura, K. Shigeno, T. Hyuga, T. Yoneda, H. Shiina, and M. Igawa. Initial evaluation of prostate cancer with real-time elastography based on step-section pathologic analysis after radical prostatectomy: a preliminary study. *International Journal of Urology: Official Journal of the Japanese Urological Association*, 14(9):811–816, 2007.

[115] Z. Sun and H. Ying. A multi-gate time-of-flight technique for estimation of temperature distribution in heated tissue: Theory and computer simulation. *Ultrasonics*, 37:107–102, 1999.

[116] J.-F. Synneva?g, A. Austeng, and S. Holm. Adaptive beamforming applied to medical ultrasound imaging. *Ultrasonics, Ferroelectrics and Frequency Control, IEEE Transactions on*, 54(8):1606–1613, August 2007.

[117] G. M. Treece, J. E. Lindop, A. H. Gee, and R. W. Prager. Freehand ultrasound elastography with a 3-d probe. *Ultrasound in Medicine and Biology*, 34(3):463 – 474, 2008.

[118] E. Turgay, S. Salcudean, and R. Rohling. Identifying the mechanical properties of tissue by ultrasound strain imaging. *Ultrasound Med Biol*, 32(2):221–235, Feb 2006.

[119] S. Ueno, M. Hashimoto, H. Fukukita, and T. Yano. Ultrasound thermometry in hyperthermia. In *Ultrasonics Symposium, 1990. Proceedings., IEEE 1990*, volume 3, pages 1645–1652, Dec 1990.

[120] O. Ukimura, I. S. Gill, M. M. Desai, A. P. Steinberg, M. Kilciler, C. S. Ng, S. C. Abreu, M. Spaliviero, A. P. Ramani, J. H. Kaouk, A. Kawauchi, and T. Miki. Real-time transrectal ultrasonography during laparoscopic radical prostatectomy. *The Journal of Urology*, 172(1):112–118, 2004.

[121] O. Ukimura, C. Magi-Galluzzi, and I. S. Gill. Real-time transrectal ultrasound guidance during laparoscopic radical prostatectomy: impact on surgical margins. *The Journal of Urology*, 175(4):1304–1310, 2006.

[122] M. G. Van Vledder, E. M. Boctor, L. R. Assumpcao, H. Rivaz, P. Foroughi, G. D. Hager, U. M. Hamper, T. M. Pawlik, and M. A. Choti. Intra-operative ultrasound elasticity imaging for monitoring of hepatic tumour thermal ablation. *HPB (Oxford)*, 12(10):717–723, Dec 2010.

[123] T. Varghese and J. Ophir. Enhancement of echo-signal correlation in elastography using temporal stretching. *IEEE Transactions on Ultrasonics, Ferroelectrics, and Frequency Control*, 44(1):173–180, 1997.

[124] T. Varghese, U. Techavipoo, J. A. Zagzebski, and F. T. Lee. Impact of gas bubbles generated during interstitial ablation on elastographic depiction of in vitro thermal lesions. *Journal of Ultrasound in Medicine*, 23(4):535–544, 2004.

[125] T. Varghese, J. A. Zagzebski, Q. Chen, U. Techavipoo, G. Frank, C. Johnson, A. Wright, and F. T. Lee Jr. Ultrasound monitoring of temperature change

during radiofrequency ablation: Preliminary in-vivo results. *Ultrasound in Medicine & Biology*, 28(3):321–329, 2002.

[126] T. Varghese, J. A. Zagzebski, and F. T. Lee Jr. Elastographic imaging of thermal lesions in the liver in vivo following radiofrequency ablation: preliminary results. *Ultrasound in Medicine & Biology*, 28(11-12):1467–1473, 2002.

[127] C. Wachinger, W. Wein, and N. Navab. Registration strategies and similarity measures for three-dimensional ultrasound mosaicing. *Academic Radiology*, 15(11):1404–1415, 2008.

[128] P. C. Walsh, H. Lepor, and J. C. Eggleston. Radical prostatectomy with preservation of sexual function: anatomical and pathological considerations. *The Prostate*, 4(5):473–485, 1983.

[129] Y. Yamakoshi, J. Sato, and T. Sato. Ultrasonic imaging of internal vibration of soft tissue under forced vibration. *IEEE Transactions on Ultrasonics, Ferroelectrics, and Frequency Control*, 37:45–53, 1983.

[130] R. Zahiri-Azar and S. Salcudean. Motion estimation in ultrasound images using time domain cross correlation with prior estimates. *Biomedical Engineering, IEEE Transactions on*, 53(10):1990 –2000, oct. 2006.

[131] Y. Zhu and T. J. Hall. A modified block matching method for real-time freehand strain imaging. *Ultrasonic Imaging*, 24(3):161–176, 2002.

Vita

Ioana Fleming came to the United States after receiving her M.D. degree from University of Medicine and Pharmacy Carol Davila in Bucharest, Romania. She received a B. Sc. degree in Computer Science from Illinois Institute of Technology in 2005, along with a certificate in Leadership Studies and one in Entrepreneurial Studies. She enrolled in the Computer Science Ph.D. program at Johns Hopkins University in the Fall of 2006. She won a Department of Defense Prostate Cancer Pre-Doctoral Fellowship award in 2009 for her work on Improved Image-Guided Laparoscopic Prostatectomy. Her research focuses on motion estimation in ultrasound images, specifically for elastography and thermal imaging. Following her interest in teaching, she has co-developed and instructed the Introduction to Medical Imaging Intersession class at Johns Hopkins, as well as intro programming courses.